

INTEGRATED OPTICAL DEVICES FOR FREE-SPACE OPTICAL COMMUNICATIONS

by

Xian Jin

B.Eng., Nanjin University of Science & Technology, P. R. China, 2006

A THESIS SUBMITTED IN PARTIAL FULFILLMENT OF
THE REQUIREMENTS FOR THE DEGREE OF

MASTER OF APPLIED SCIENCE

in

The College of Graduate Studies
(Electrical Engineering)

THE UNIVERSITY OF BRITISH COLUMBIA
(Okanagan)

December 2009

©Xian Jin, 2009

Abstract

Optical wireless communication technologies for free-space optical (FSO) transmission, distribution, and reception have numerous potential benefits. Such systems offer incredibly high data communication rates (in the same way that fibre optic technologies have revolutionized long-haul Terabit/second data transmission) together with the distributive benefits of multi-user wireless networking. Communication devices for these FSO technologies are presented in this thesis. A macroscopic passive retroreflective structure is introduced first for signal retroreflection over the full 4π steradians solid angle. Modulation is demonstrated with this structure through the use of liquid crystal switching elements. The FSO device work is then extended with an active retroreflective structure incorporating corner-cube-based retro-detection with integrated and orthogonal photodiodes. An actively-controlled differential triangulation process is demonstrated with this novel device to optimize the optical channel alignment in the FSO communication system. The proposed integrated retroreflective structures are ideally-suited to bi-directional (uplink and downlink) multi-nodal systems and have potential to be extended to ultrafast (picosecond) optical modulation in future work.

Table of Contents

Abstract	ii
Table of Contents	iii
List of Tables	vi
List of Figures	vii
List of Abbreviations	x
Acknowledgments	xi
Dedications	xii
Chapter 1 Introduction	1
1.1. Background and Motivation	1
1.2. Literature Review	3
1.3. Scope of This Thesis	5
Chapter 2 Macroscopic Device: Omni-directional Solid Composite Retroreflectors	7
2.1. Background	7
2.2. Operation of Elemental CCRs.	9
2.3. Theoretical Framework	10
2.3.1. Single Hollow Retroreflector	10
2.3.2. Single Solid Retroreflector.	12

2.3.3.	Composite Hollow Retroreflector	13
2.3.4.	Composite Solid Retroreflector	14
2.4.	Experimental Framework	15
2.4.1.	Structural Optical Response	16
2.4.2.	Optical Communication and Modulation Capability	20
2.5.	Summary.	23

Chapter 3 Integrated Device: A Corner-Cube-Based Optical Control and Communication

	System	25
3.1.	Background	25
3.2.	System Design and Operation	27
3.3.	Theoretical Framework	29
3.3.1.	Retroreflection Characteristics	29
3.3.2.	Detection Characteristics	30
3.3.2.1.	Detected Power Levels for the First Illumination Case with $n_1 < n_2 < n_3$	31
3.3.2.2.	Detected Power Levels for the Second Illumination Case with $n_1 < n_3 < n_2$	37
3.3.2.3.	Detected Power Levels for the Third Illumination Case with $n_2 < n_1 < n_3$	43
3.3.2.4.	Detected Power Levels for the Fourth Illumination Case with $n_2 < n_3 < n_1$	49
3.3.2.5.	Detected Power Levels for the Fifth Illumination Case with $n_3 < n_1 < n_2$	55
3.3.2.6.	Detected Power Levels for the Sixth Illumination Case with $n_3 < n_2 < n_1$	61
3.3.2.7.	Summary of Photocurrent Levels for all Six Illumination Cases	67
3.3.3.	Control Characteristics	71
3.4.	Experimental Framework	78
3.4.1.	Verification of the Control Capability	78
3.4.2.	Verification of the Communication Capability	82
3.5.	Summary.	86

Chapter 4 Conclusions	87
4.1. Summary of Contributions	87
4.2. Future Work	88
Bibliography	90
Appendices	95
Appendix A Driving a Pi-cell Optical Modulator	95
Appendix B Summary of Mathematical Expressions for Individual PDs Photocurrents ..	97
Appendix C Matlab Ray-tracing Code	100

List of Tables

3.1 Theoretical normalized differential photocurrents for PD ₁ , PD ₂ and PD ₃ , given various directional cosine component inequality permutations	70
--	----

List of Figures

1.1 Two operation schemes of FSO communication: (a) point-to-point transmissions and (b) multi-point broadcasting (optical/infrared wireless).	2
1.2 Two communication modes of FSO communication systems: (a) active downlink mode and (b) passive uplink mode.	3
1.3 A (a) CorelDraw schematic and (b) photograph of a CCR.	4
2.1 The coordinate system is shown along with the azimuthal angle ϕ and polar angle θ	8
2.2 The retroreflection process in a three-mirrored CCR structure with incident and retroreflected rays.	10
2.3 Theoretical model retroreflected powers for single CCRs	12
2.4 Theoretical model retroreflected powers for composite CCRs	15
2.5 SolidWorks retroreflector schematics.	16
2.6 The experimental system for measuring the retroreflected optical response is shown	18
2.7 Experimental retroreflected power as a function of azimuthal angle ϕ for the composite beveled retroreflector.	19
2.8 The retroreflective power levels are shown as a function of time for the composite beveled retroreflector	21

2.9 Passive uplink mode modulated retroreflective signals are shown as a function of time for the composite beveled retroreflector.	22
2.10 Passive uplink mode modulated retroreflective signals are shown as a function of time for the composite beveled retroreflector.	23
3.1 SolidWorks schematic of the integrated retro-detection photocell.	28
3.2 Schematics are shown for the internal reflection processes occurring in the retro-detector for directional cosine conditions $n_1 < n_2 < n_3$	36
3.3 Schematics are shown for the internal reflection processes occurring in the retro-detector for directional cosine conditions $n_1 < n_3 < n_2$	42
3.4 Schematics are shown for the internal reflection processes occurring in the retro-detector for directional cosine conditions $n_2 < n_1 < n_3$	48
3.5 Schematics are shown for the internal reflection processes occurring in the retro-detector for directional cosine conditions $n_2 < n_3 < n_1$	54
3.6 Schematics are shown for the internal reflection processes occurring in the retro-detector for directional cosine conditions $n_3 < n_1 < n_2$	60
3.7 Schematics are shown for the internal reflection processes occurring in the retro-detector for directional cosine conditions $n_3 < n_2 < n_1$	66
3.8 Theoretical photocurrents are shown as surfaces varying with ϕ and θ . Independent and normalized photocurrents are displayed for (a) P_1 , (b) P_2 , and (c) P_3	72
3.9 The (a) theoretical photocurrent differential sum and (b) theoretical summed photocurrent are shown as a surface varying with ϕ and θ	74
3.10 The (a) 3D view and (b) 2D view of theoretical retroreflected power are shown as a surface varying with ϕ and θ	75

3.11 Theoretical Matlab ray-tracing model results for the retro-detector's photocurrent differential sum are shown.	77
3.12 Experimental results of the retro-detection photocell for three laser orientations.. . . .	79
3.13 Experimental photocurrent surfaces varying with ϕ and θ are shown.	81
3.14 Experimental photocurrent differential sum surface varying with ϕ and θ	82
3.15 The (a) CorelDraw schematic and (b) photograph of experimental laser-based system for the retro-detection photocell.	83
3.16 Photocurrents for the (a) active downlink mode and (b) passive uplink mode are shown as a function of time for the retro-detection photocell.	84
3.17 A photograph of the experimental LED-based broadcasting system is shown.	85
3.18 Photocurrent results for local and remote detection with 4 m propagation are shown for a modulated LED local source broadcasting toward the remote retro-detector.	86
4.1 A (a) SolidWorks schematic and (b) photograph showing the proposed gold-coated GaAs corner-cube-based photoconductive switching device	89
4.2 The (a) crystallographic orientations for the {111} corner-cube texturing and the resulting (b) corner-cube micro-structural arrays.	89
5.1 The (a) driver chip HV 508 for the Pi-cell LC modulator is soldered onto a bare circuit board, and the (b) pin configuration of the HV 508 is shown	96

List of Abbreviations

Abbreviations

Definitions

CCD

Charge Coupled Device

CCR

Corner-Cube Retroreflector

CMOS

Complementary Metal Oxide Semiconductor

DC

Direct Current

FSO

Free-Space Optical

GaAs

Gallium Arsenide

GPS

Global Positioning System

IR

Infrared

LC

Liquid Crystal

LED

Light-Emitting Diode

LOS

Line-of-Sight

MEM

Micro-Electro-Mechanical

MIMO

Multiple-Input-Multiple-Output

OCB

Optically Compensated Bend

PD

Photodiode

RF

Radio Frequency

RMS

Root Mean Square

SNR

Signal-to-Noise Ratio

Acknowledgments

I am very deeply grateful to many individuals and organizations. Without their support, the projects could not be completed.

First the foremost, I would like to thank my supervisor, Dr. Jonathan F. Holzman, for his understanding, encouragement, support, enthusiasm, and guidance. Your helpful suggestions and patient conceptions have gone through all my works in the past two years and made this thesis possible. I will continue to be influenced by his rigorous scholarship, clarity in thinking, and professional integrity.

Also, I would like to express my thanks to the following advisory committee members: Dr. Julian Cheng, and Dr. Richard Klukas. Thanks also go to Dr. Geoff Steeves, from University of Victoria, for his willingness to serve as my external examiner. I really appreciate their valuable time and constructive comments on my thesis.

Many thanks to the technical support from R. LaMountain, Dr. Wilson Eberle and School of Engineering for providing the facilities and research spaces to fabricate and test each of the devices presented here. Also, another thanks to Ali Ahmadi and Milad Abolhasani for their helpful technical advice and patience on my project experiments.

I would like to thank my dear peers Xuegui Song, Junfeng Zhao, James Jianchen Sun, Mingbo Niu, Nick Kuan-Hsiang Huang, Yeyuan Xiao, Chiun-Shen Liao, Ning Wang, Vicki Wei, Sapphire Man Ding, and Luyan Mei for all of their assistances, insight, encouragement and support during my two-year study at the University of British Columbia Okanagan.

Finally, special thanks are owed to my parents for their patience, understanding and support over all these years of education, both morally and financially. I wish to acknowledge my dear wife, Yiwen Wu, for giving invaluable and thoughtful mental support during the whole 7-year long-distance love-run. Without their constant support and encouragement, all my achievements would not be possible.

Dedications

*This thesis is dedicated to my family...
for all of their love and support.*

Chapter 1

Introduction

1.1. Background and Motivation

Laser-based devices, optical instrumentation, and photonic systems have opened the door to many possibilities in both pure and applied applications and revolutionized communications in the past several decades. In particular, the tremendous speeds and broad bandwidths of these optical sources have been especially useful in communication systems, as fibre-optic technologies continue to grow, and photonic switches are now emerging as useful tools in both data processing and information storage.

An innovative approach for optical communication has emerged recently for environments that lend themselves to point-to-point and line-of-sight (LOS) implementations. Technologies commonly associated with radio-based wireless communications are being applied here in free-space optical (FSO) wireless communication formats [1-4]. This optical communication technology uses light propagating in free-space to transmit signals between transceivers and receivers, and it is particularly useful where the physical connection by means of fibre cables is impractical due to high costs or inaccessibility.

FSO wireless communication systems consist of two operation schemes. The two schemes are shown in Fig. 1.1. The point-to-point information transmission scheme in Fig. 1.1(a) is applicable to dense urban environments for which there is minimal pre-existing optical communication infrastructure. Such systems are advantageous because optical frequency bands are unlicensed, and the required transmitter/detector components are inexpensive in comparison to their radio frequency (RF) counterparts. From an operational standpoint, LOS wireless optical transmission systems have also been shown to be less sensitive to fading and co-channel interference in bi-directional communication implementations [5]. The second operation scheme is shown in Fig. 1.1(b) and is applicable to multi-point broadcasting (for optical/infrared wireless

communications) [6]. For these communication systems, the optical wavelength range is attractive in terms of data rates, as optical frequencies are extremely high and allow for large transmission bandwidths. Moreover, optical wireless networks requiring improved security can benefit from the confined nature of infrared/optical wireless radiation.

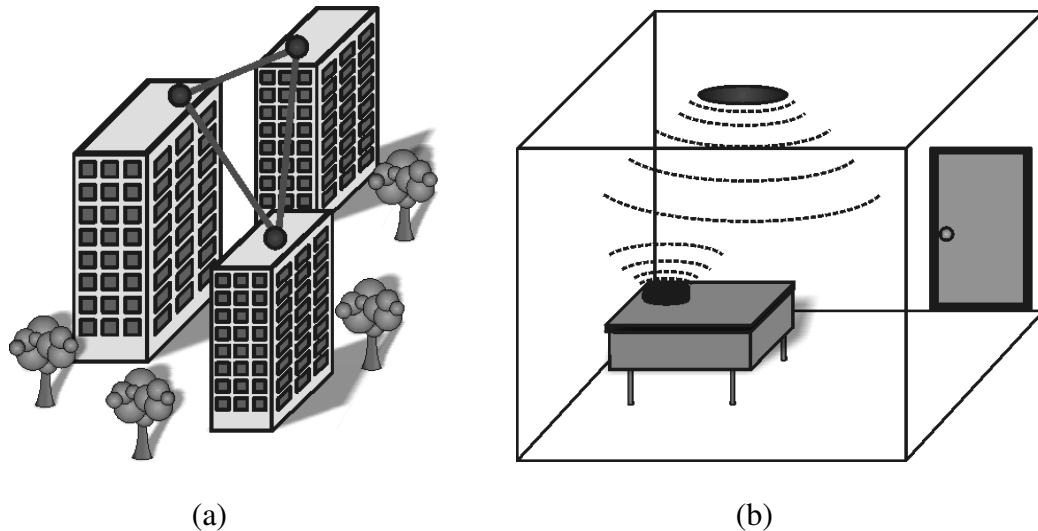


Figure 1.1 Two operation schemes of FSO communication: (a) point-to-point transmissions and (b) multi-point broadcasting (optical/infrared wireless).

At the heart of free-space (wireless) optical communication is the desire to control bi-directional optical beams. Typically, these FSO systems employ both an active downlink communication mode and a passive uplink communication mode. In the active downlink mode, shown in Fig. 1.2(a), transceivers broadcast encoded optical beams into free-space for subsequent receiver detection. In the passive uplink mode in Fig. 1.2(b), the receivers employ reflective structures to redirect the light back to the transceivers after local modulation of the beam [7]. Such implementations allow the communication process to be largely independent of the transceiver and receiver positions. There are, however, several key challenges associated with both active and passive links, and some of these challenges include link performance, channel estimation, angular dependent directionality, optical response sensitivity, optical alignment and communication capability. In this thesis, I will focus on the angular dependence and directionality of these links to improve the optical alignment and communication capabilities in FSO communications.

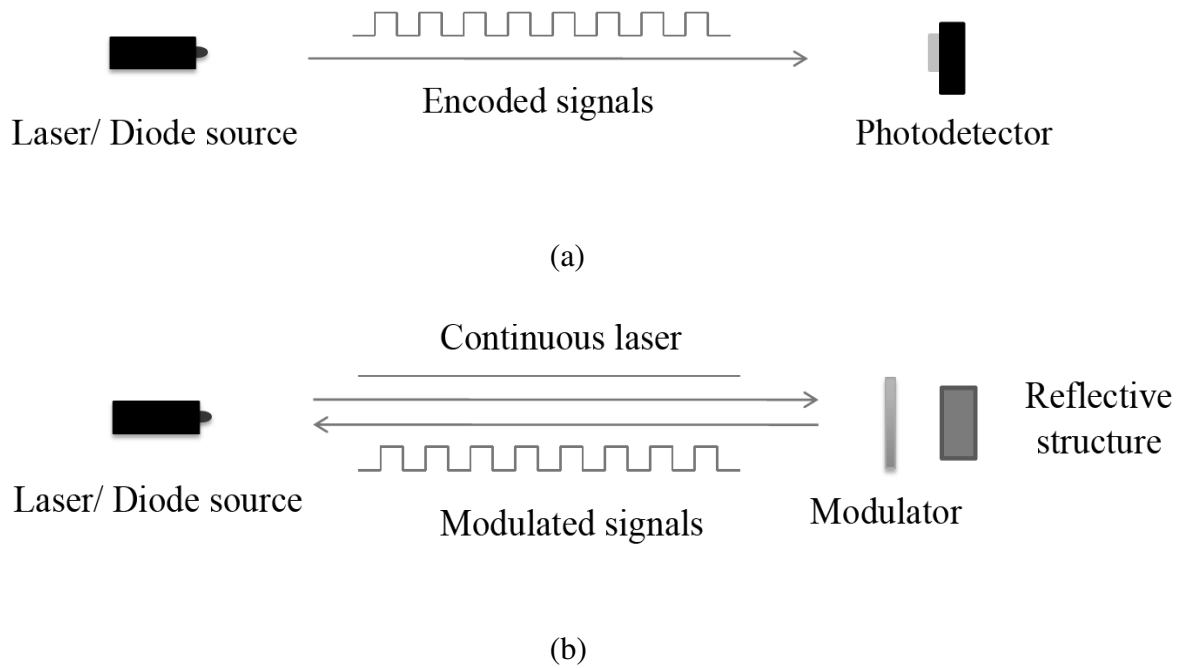


Figure 1.2 Two communication modes of FSO communication systems: (a) active downlink mode and (b) passive uplink mode.

1.2. Literature Review

FSO bi-directional optical communication systems have been demonstrated successfully in the past with configurations incorporating structures for both retroreflection and modulation. A corner-cube retroreflector (CCR) is an excellent candidate for this in an FSO passive uplink configuration. With a suitable retroreflector employed at each node, the incoming optical beam can be modulated with the local information and redirected directly back to the transmission source. The optical link operation is, therefore, largely independent of the position of both the transmitters and receivers.

A standard CCR, shown in Fig. 1.3, is a device made up of three mutually orthogonal reflective surfaces, or mirrors, forming an interior corner. It reflects light beam back to its source with a minimum of light scattering [8-9]. The respective directions of the incident ray's Cartesian components are successively reversed by each of the three mirrors in this structure. This retro-process allows light entering the CCR to be reflected back to its source in a way that is largely independent of the angle of incidence. The reflective surface area for which this retroreflection occurs is called the effective retroreflective area, and it is important for FSO devices to have large effective retroreflective areas.

Currently, there are several research groups involved in the development of optical wireless or FSO links using retroreflective structures. The U. S. Naval Research Laboratory, for example, has created a FSO communication link at 1550 nm using multiple quantum well modulating retroreflectors over a distance of one kilometer [10]. In addition, the University of Oxford employs retroreflectors combined with liquid crystal (LC) modulators, which can be integrated with micro-machines for low power transceivers [11]. The researchers Mao and Kahn at the University of California, Berkeley, have even mechanically deflected the CCR mirrors to inhibit retroreflection and encode optical information [7]. The communication rate of this latter bi-directional optical device is on a millisecond timescale, however, as low data rates are associated with opto-mechanical modulation schemes in general.

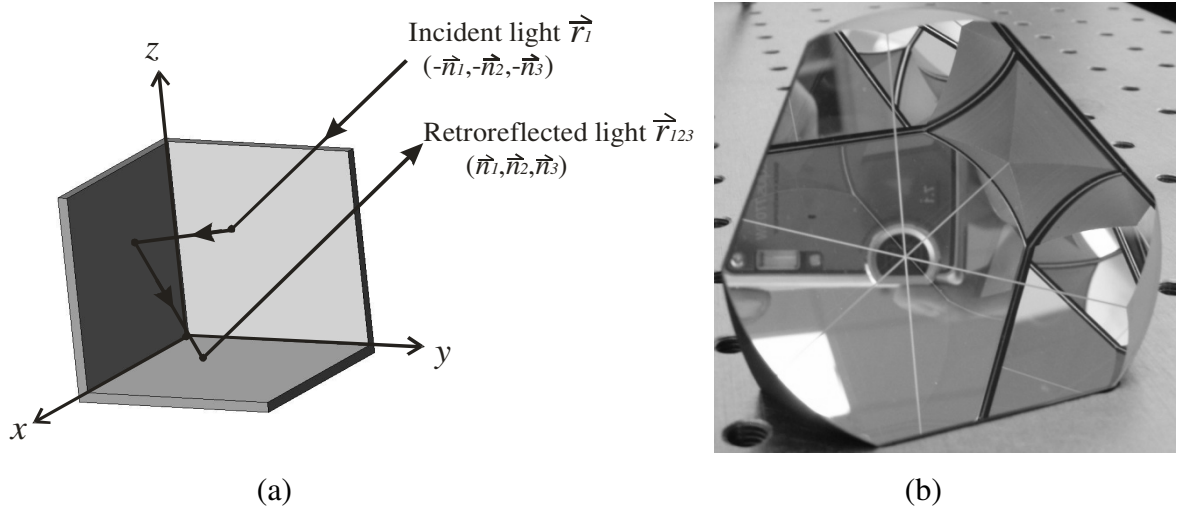


Figure 1.3 A (a) CorelDraw schematic and (b) photograph of a CCR. The structure has three mutually-orthogonal reflective surfaces in an interior corner. The retro-reflection process is displayed for three ray directional cosine components, n_1 , n_2 and n_3 with respect to x -, y -, and z -directions in (a).

While the retroreflection mechanism is typically implemented by way of a simple CCR, a wide variety of optical switching mechanisms have been explored for providing the required modulation. Examples of this optical modulation include those that modulate the optical absorption of the CCR entrance/exit facet (with LC polarization modulation [11]), those that modulate the beam alignment between the transceiver and receiver (with opto-mechanical beam deflection of the CCR mirrors [7]), and those that modulate the optical reflectivity of the internal CCR mirrors (with multi-quantum well absorbers [12]). Endeavors are underway to implement

such systems in Smart Dust optical switching arrangements [13] with numerous retroreflective transmitter/receiver communication nodes in an FSO environment.

In this thesis, I study the angular dependence and directionality of CCRs and fabricate two novel devices to improve the directionality of FSO communication links. For the first device, I introduce a composite assembly of CCRs that is fabricated to enhance the directionality of the overall system. It is shown that the element can provide complete omni-directionality. For the second device, photodiodes (PDs) are incorporated into the CCR structure. The resulting PD structure is a new form of optical device, as it can effectively detect incoming optical signals as well as their incident direction (by way of a new differential triangulation technique). The enhanced retroreflection directionality of these devices, together with optical modulation, is shown to provide effective FSO communication.

1.3. Scope of This Thesis

This thesis consists of four chapters.

Chapter 1 presents the background and motivations for FSO communication. Insight is given toward modern wireless communications, and the benefits of FSO communications are presented.

Chapter 2 provides a detailed introduction and analyses for an omni-directional retroreflecting structure. The device is a composite assembly of individual retroreflectors, and the theoretical analyses show that this structure allows for retroreflection over the full 4π steradians solid angle. The dynamic response of the omni-directional device is then experimentally tested in a simplified passive uplink communication configuration with LC optical modulators covering the composite entrance interfaces. The modulation and communication characteristics of this composite assembly are seen to be successful.

Chapter 3 introduces a new corner-cube-based retro-detection photocell. The structure is fabricated with three independent and mutually-perpendicular PDs, whose differential photocurrents can be used to probe the alignment state of incident beams. These differential photocurrents are then introduced and used in an actively-controlled triangulation procedure to optimize the communication channel alignment in an FSO system. The active downlink and passive uplink communication capabilities of this system are subsequently demonstrated with both a laser-based FSO system and a broadband light-emitting diode (LED) broadcasting FSO system.

Chapter 4 gives a final summary for the contributions presented in this thesis. In addition, future work related to my current research is discussed.

Chapter 2

Macroscopic Device: Omni-directional Solid Composite Retroreflectors

In this chapter, a composite solid CCR is introduced as a novel element for a laser-based FSO wireless communication system. The transmission and communication characteristics of such a FSO data transmission system are characterized, and issues of optical directionality, being related to the optical modulation depth, are investigated for a variety of retroreflecting structures. It is finally shown that this device has an omni-directional retroreflective angular response covering the full 4π steradians solid angle. Such a configuration is a particularly intriguing solution for point-to-point and LOS optical communication implementations.

2.1. Background

As mentioned in the previous chapter, the fundamental principle behind the operation of FSO systems is the bi-directional nature of the optical communication links by way of either an active optical relaying format or a passive optical relaying format. Of these two optical formats, the passive FSO arrangement is particularly attractive for optical wireless communications, as it can be made to be less sensitive to the optical beam alignment, i.e. to be largely independent of the positions of transceivers. With a suitable retroreflector employed at each node, the incoming optical beam can be modulated with the local information and redirected directly back to the transmission source. Recent research topics have focused largely on the optical encoding mechanisms of this process, and a variety of modulation schemes have been proposed, including mechanical modulation of the reflective mirrors and LC modulation of the node entrance. In contrast to this, the work I present here investigates and optimizes the inherent retroreflection process for the optical wireless systems.

The process of retroreflection is at the heart of most passive FSO arrangements, and CCRs are excellent candidates for implementing this retroreflection. CCRs redirect incoming light rays back

to their transmission source by negating each of the three orthogonal ray vector components with the three respective mutually perpendicular mirrors. The exiting beam leaves the CCR in a direction that is anti-parallel to the incident beam.

One of the greatest challenges of implementing multi-nodal bi-directional communication systems has been the geometrical limitations on the reflective nature of the singular CCR. Light incident upon a CCR only returns to its source when it enters the corner through the entrance acceptance cone of the three-mirror corner. This cone corresponds to a solid angle of only $\pi/2$ steradians ($1/8^{\text{th}}$ of the full sphere), as the corresponding azimuthal angle of ϕ and polar angle of θ both range from 0° to 90° (see Fig. 2.1). With these angular limitations in mind, recent work on micro-electro-mechanical (MEM) retroreflective devices have focused on the enhancement of the angular retroreflective acceptance cone through the introduction of rotationally-symmetric corner-cubes in the two-dimensional plane. A four-corned MEM quadruplet system was introduced recently with the above-mentioned goals in mind, and this system was successful in demonstrating retroreflection over 2π steradians. The use of four back-to-back corner cubes allowed for retroreflection with ϕ values ranging from 0° to 360° and θ values ranging from 0° to 90° [14].

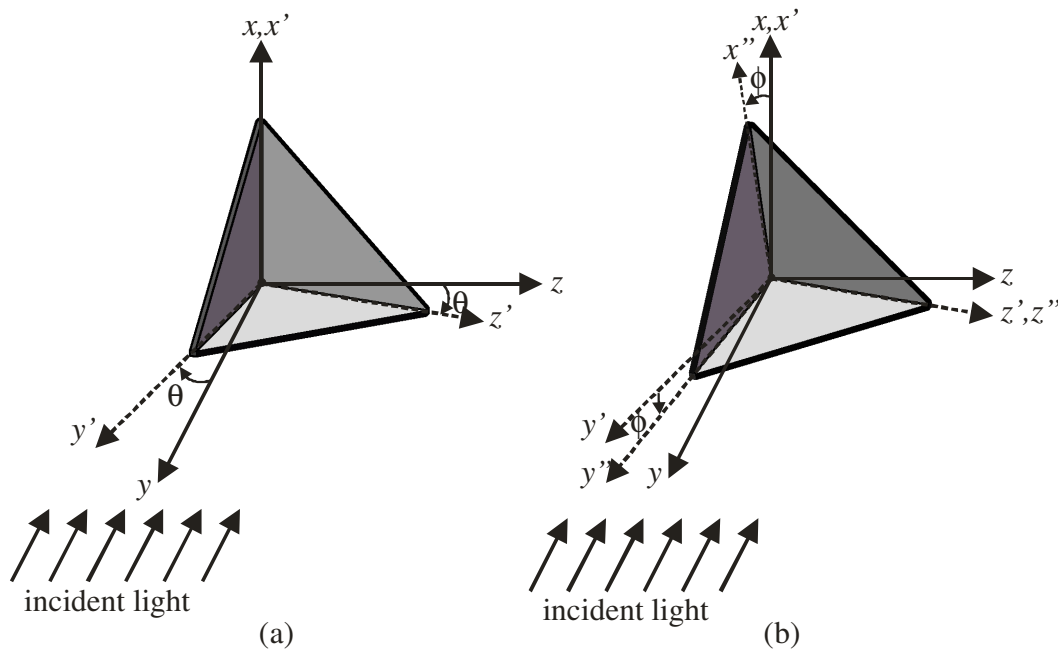


Figure 2.1 The coordinate system is shown along with the azimuthal angle ϕ and polar angle θ . Figure (a) shows the first rotational step on the gyroscope, where the structure is rotated θ about the x -axis. Figure (b) shows the second rotational step on the gyroscope, where the structure is rotated ϕ about the z' -axis. The incident light is anti-parallel to the y -axis.

In my work, the angular acceptance cone of retroreflective structures is thoroughly analyzed and a composite structure is introduced. The composite corner-cube octuplet that is presented here is shown to significantly broaden the operational angles of standard retroreflective structures through the use of multiple solid corner-cube substructures. Eight of these substructures are assembled into a composite retroreflector in such a way that the angular acceptance cone of each retroreflector substructure effectively overlaps with its neighbors. The resulting structure is shown to exhibit retroreflection over the full 4π steradians spherical solid angle, and the resulting device can effectively return incoming optical radiation over the 0° to 360° range of ϕ values and the 0° to 180° range of θ values. The optical response of the composite structure is then characterized here and compared to theoretical results for various combinations of ϕ and θ . Ultimately, the optical communication capability of the structure is tested through a simplified passive uplink communication configuration, and Pi-cell LC modulators with sufficiently fast switching times and broad angular responses are mounted on each of the entrance interfaces of the composite structure to demonstrate the modulation capabilities while encoding the returning beam.

2.2. Operation of Elemental CCRs

The fundamental structure within a retroreflector is the corner-cube. The CCR is composed of three mutually-perpendicular reflective surfaces that form an interior corner. When incident light enters the CCR with ϕ and θ directions as shown in Fig. 2.1 and strikes each of the three mirrors, the x , y and z components of the incoming ray are successively reversed, such that the light exits the CCR at an anti-parallel direction to the incident ray. Such a scenario is shown in the coordinate geometries of Fig. 2.2. Note here that the success of this retroreflection is highly dependent on the spherical coordinate angles of ϕ and θ . All retroreflectors have a finite angular acceptance cone for which this retroreflection process occurs, as not all rays entering the CCR strike three mirrors and undergo retroreflection. This defines the effective aperture (effective area). Certain cases exist for which rays strike only one or two mirrors, and the resulting scattered light does not return to the source. The degree to which a structure acts as a retroreflector can be quantified by the solid angle associated with the retroreflective angular acceptance cone set by ϕ and θ . This acceptance cone is analyzed theoretically for four retroreflective structures with increasing complexity in the following sections.

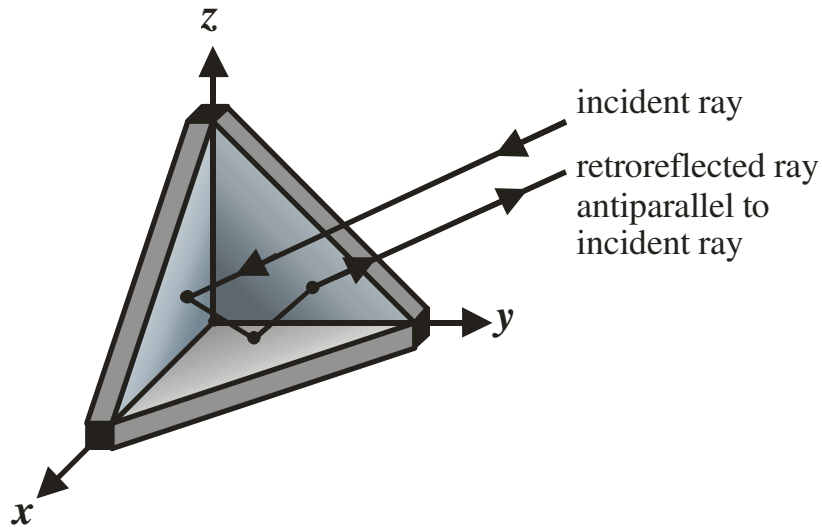


Figure 2.2 The retroreflection process in a three-mirrored CCR structure with incident and retroreflected rays.

2.3. Theoretical Framework

The acceptance cones for which retroreflection occurs are thoroughly investigated for four retroreflective CCR structures in the following subsections. All incident light conditions for retroreflection are studied here with a Matlab ray-tracing model analysis.

2.3.1. Single Hollow Retroreflector

A common goal in retroreflection-based applications is the optimization of the angles at which the retroreflection process occurs. The standard retroreflector uses a hollow corner-cube for which the possibility of retroreflection exists when rays enter the corner-cube at ϕ and θ values within the ranges $0^\circ \leq \theta \leq 90^\circ$ and $0^\circ \leq \phi \leq 90^\circ$. These ranges are necessary conditions, though not entirely sufficient conditions, for retroreflection. The position of the incoming ray must also conform to the requirement of striking each of the three orthogonal mirrors. This latter condition is studied here by way of a ray-tracing model assuming idealized anti-reflection coatings and angular-independent mirror reflectivity. The latter assumption is particularly good due to the fact that the total reflectivity of this CCR is largely balanced to a nearly-constant value, as the contribution from a glancing angle surface is balanced by near-normal incidence on the remaining two surfaces. The probability of retroreflection for a given light ray is inherently

dependent upon both the probability of it entering the retroreflector and the subsequent probability of it striking three mirrors and undergoing retroreflection. These effects are simultaneously quantified by the model by selecting values of ϕ and θ , uniformly illuminating the structure with a sufficiently dense matrix of light rays at this orientation, and recording the retroreflection efficiency for this orientation as the ratio of retroreflected to incident light rays. The Matlab ray-tracing modeled results for this single hollow structure are shown in Fig. 2.3(a) with $\theta = 45^\circ$ for the hollow retroreflector presented in the inset. Note that as ϕ and θ values are changed, the number of light rays entering the CCR varies, and the number of retroreflected rays varies. The optimal reflected power occurs for an orientation with $\phi = 45^\circ$, and retroreflection only occurs for ϕ values within an open angular interval

$$\phi \in (0^\circ, 90^\circ) \text{ (single hollow CCR)}. \quad (1)$$

The features seen within Fig. 2.3(a) are a result of the fact that the probability of a ray's retroreflection is a function of two underlying probabilities:

- i. the probability that the ray enters the corner-cube, and
- ii. the probability that this same light ray will reflect off the three orthogonal mirrors and undergo retroreflection.

The former (external) condition manifests itself through the size of the CCR interface as viewed by the source, with incident orientations nearly normal to the entrance interface of CCR at $\phi = 45^\circ$ having higher entrance probabilities and light rays with orientations outside the equation (1) interval having entrance probabilities that are identically zero. These external conditions ultimately set the maximal interval width along the x -axis of the figure. The latter (internal) condition manifests itself through the nonmonotonic relationship observed in Fig. 2.3(a), with it rising from zero at $\phi = 0^\circ$ and dropping back down to zero at and beyond $\phi = 90^\circ$. Light rays within the corner-cube can be retroreflected if they strike each of the three orthogonal mirrors, and this requirement is dependent both upon the ray position (with light ray positions far from the vertex having the smallest probability for retroreflection) and its angle (with light ray angles well off the normal having the least probability for retroreflection). These internal conditions lead to the symmetric and peaked response shown in the same Fig. 2.3(a). Ultimately, if the directionality of retroreflectors is to be enhanced, these retroreflection probabilities will have to be improved beyond that of a single retroreflector [2].

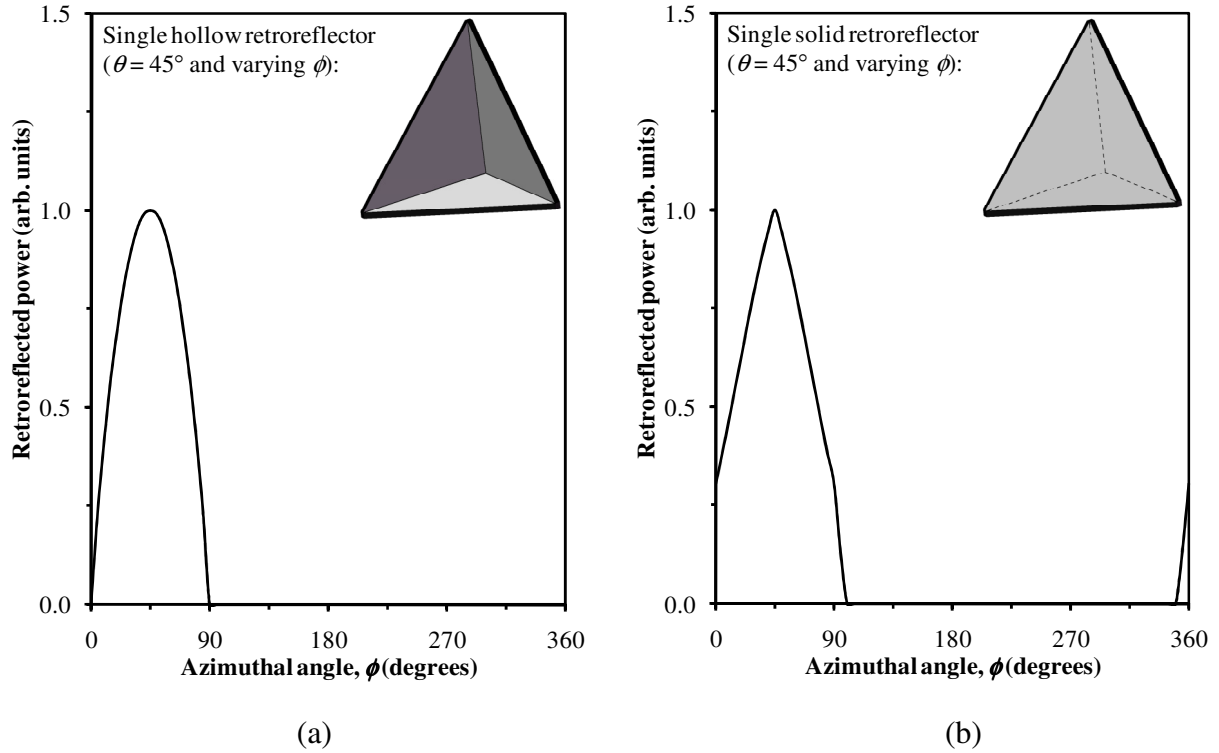


Figure 2.3 Theoretical model retroreflected powers for single CCRs. They are shown as a function of the azimuthal angle ϕ for uniform optical illumination of the (a) single hollow retroreflector and the (b) single solid retroreflector. The results are calculated for a polar angle of $\theta = 45^\circ$.

2.3.2. Single Solid Retroreflector

As mentioned in the previous subsection, the entrance acceptance cone of a CCR plays an important role in determining the likelihood for light ray retroreflection. An interesting solution to extend these angular capabilities beyond the 0° to 90° range makes use of light ray refraction. A silica-filled solid CCR substructure, for example, can be used to bend light rays that would normally not be capable of entering the corner-cube into the structure. A greater number of light rays will be captured, the external probability for retroreflection will be enhanced, and the directionality will be therefore improved. To analyze this scenario, the Matlab ray-tracing model is applied to such a structure, after having been modified to accommodate the angular dependence of the air-silica interface reflectance. The results are shown in Fig. 2.3(b) for the case where $\theta = 45^\circ$. The structure is shown in the figure inset. The angular acceptance cone of this CCR is seen to be broadened below 0° and beyond 90° , and the reflected power at the

extreme orientations of $\phi = 0^\circ$ and 90° has now increased from 0% of the maximum for the hollow case to 30% of the maximum for this solid case. These effects are brought about by refraction, as the silica refractive index of $n = 1.5$ enhances the directionality of retroreflection and expands the angular acceptance cone to be within an open angular interval

$$\phi \in (-\alpha, 90^\circ + \alpha) \text{ (single solid CCR)}. \quad (2)$$

Here, $\alpha \approx 10^\circ$ represents the broadened condition for light ray retroreflection given the orthogonal $\theta = 45^\circ$ and ϕ rotations, though it should be noted that this broadening is a function of the rotational geometries. Non-orthogonal rotations, for example, with $\theta = 45^\circ$ followed by rotations about the original z -axis can further broaden the recorded angular response, as the acceptance conditions are extended by two angle conditions:

- i. an angle of $\arcsin [(\sqrt{2}n - \sqrt{3 - n^2})/3]$ in the y -axis direction which is set by the limiting case for which rays are bent in parallel to one mirror, and
- ii. an angle of $\arcsin (1/\sqrt{3})$ in the z -axis direction which is set by the limiting case of total-internal-reflection.

2.3.3. Composite Hollow Retroreflector

In section 2.3.1 a hollow retroreflective structure was introduced. The structure was capable of retroreflection, though its operation was limited to only 1/8 of the full 4π steradians solid angle. The orthogonal construction of this corner does, however, offer an intriguing possibility for improving upon its overall directionality. The cube can be implemented as a substructure within a composite assembly. The assembly is comprised of eight individual hollow CCRs oriented back-to-back such that their respective planes of symmetry are defined by the $[\pm 1 \pm 1 \pm 1]$ directions. The composite structure is shown in the inset of Fig. 2.4(a), and the reflected power for this composite device is shown in the same figure for a θ value of 45° . Note that the structure is able to effectively replicate the individual power distributions on 90° intervals, and the angular acceptance cone of each individual CCR is spread across the 4π steradians solid angle. The retroreflection is then exhibited for ϕ values within the angular interval

$$\phi \in (0^\circ, 90^\circ) \cup (90^\circ, 180^\circ) \cup (180^\circ, 270^\circ) \cup (270^\circ, 360^\circ) \text{ (composite hollow CCR)}. \quad (3)$$

This multiplicity greatly improves the directionality of the original single hollow CCR, as the external condition for retroreflection is dramatically enhanced by the inclusion of multiple retroreflectors with their own individual angular responses. Light rays from arbitrary orientations now have a much higher probability of entering a CCR and undergoing retroreflection. A final challenge still remains, however, with regard to the reflected powers at the extreme ϕ values of 0° , 90° , 180° , and 270° , as the reflected powers here are negligible, and such orientations would leave the potential for unsuccessful retroreflection.

2.3.4. Composite Solid Retroreflector

The limiting conditions of $\phi = 0^\circ$, 90° , 180° , and 270° for which no retroreflected power is observed can be removed through the incorporation of a composite solid structure as an extension of the previous composite hollow retroreflector. Such a device has the same structure as that in subsection 2.3.3, but it is now comprised of a material, silica, with a refractive index $n = 1.5$. In this way, the benefits of the single solid retroreflector in subsection 2.3.2 (being characterized by a broadened angular response) are merged with the benefits of the composite hollow structure in section 2.3.3 (being characterized by multiple angular responses over the full 0° to 360° range). The structure is shown in the inset of Fig. 2.4(b), and the retroreflected power is shown in the same figure for $\theta = 45^\circ$ with a closed angular interval for retroreflection of

$$\phi \in [0^\circ, 360^\circ] \text{ (composite solid CCR)}. \quad (4)$$

Note that over the full 360° range of ϕ values, the structure now provides finite reflective power at or above 50% of the maxima. The orientations where minima are expected for the hollow structures, corresponding to incident rays entering the CCRs along the $[\pm 1 \ 0 \ 0]$, $[0 \ \pm 1 \ 0]$, and $[0 \ 0 \ \pm 1]$ directions, are improved beyond that of the hollow composite structure. Local maxima are created at these points from the overlapping of the individual solid CCR responses at $\phi = 0^\circ$, 90° , 180° , and 270° , and the retroreflected powers here reach 60% of the absolute maxima (being twice the 30% power exhibited by the single solid CCR). This improvement is due to the additive nature of the composite solid structure as the retroreflected power from multiple CCRs is summed to form the returned beam – a result that is possible only through the

use of a structural refractive index $n > 1$ and multiple retroreflectors. Indeed, the ultimate composite solid retroreflector is able to effectively return incident power at all incident angles.

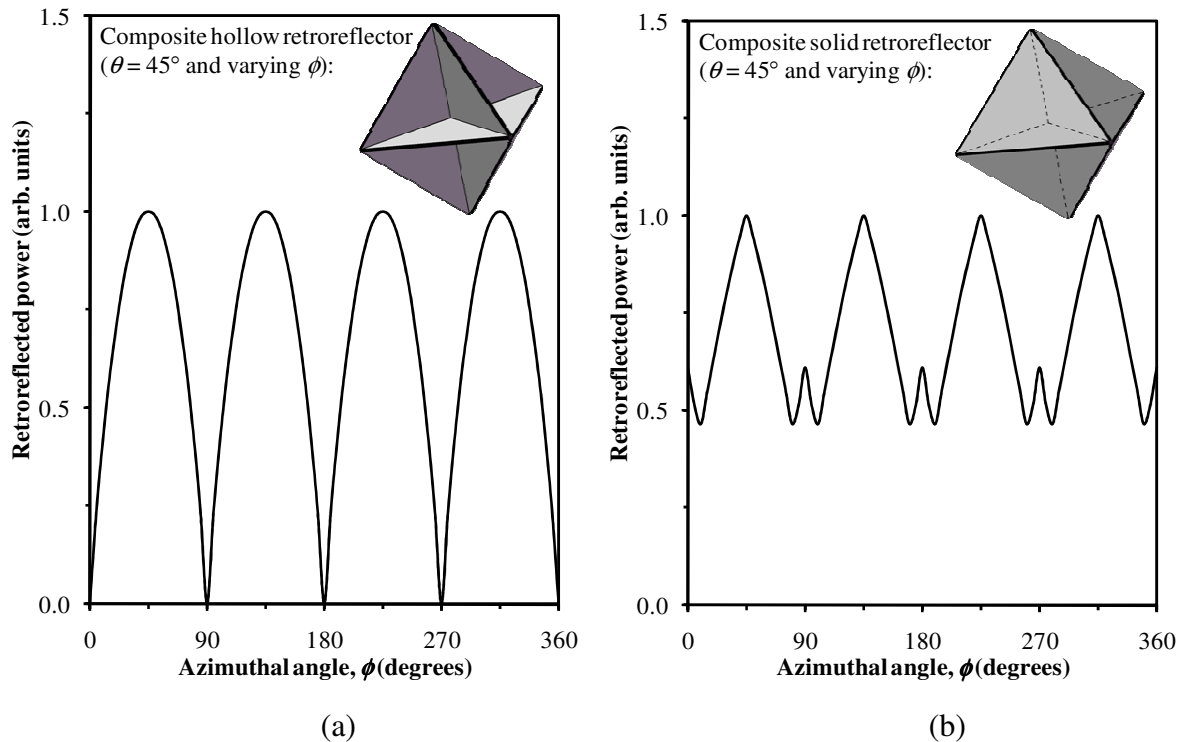


Figure 2.4 Theoretical model retroreflected powers for composite CCRs. They are shown as a function of the azimuthal angle ϕ for uniform optical illumination of the (a) composite hollow retroreflector and the (b) composite solid retroreflector. The results are calculated for a polar angle of $\theta = 45^\circ$.

2.4. Experimental Framework

The composite structures proposed in section 2 demonstrated that the omni-directional nature of retroreflection could be improved by transitioning from the composite hollow structure (shown in Fig. 2.5(a)) to the composite solid structure (shown in Fig. 2.5(b)). In an effort to improve the practicality of this latter solid structure, the individual CCRs are made more compact by beveling each of its extreme points and producing a circular (111) planar interface with a diameter of 42 mm. The losses in retroreflected power attributed to these extreme sections of the CCRs are minimal [1]. A Solidworks schematic of the beveled composite retroreflector is shown in Fig. 2.5(c).

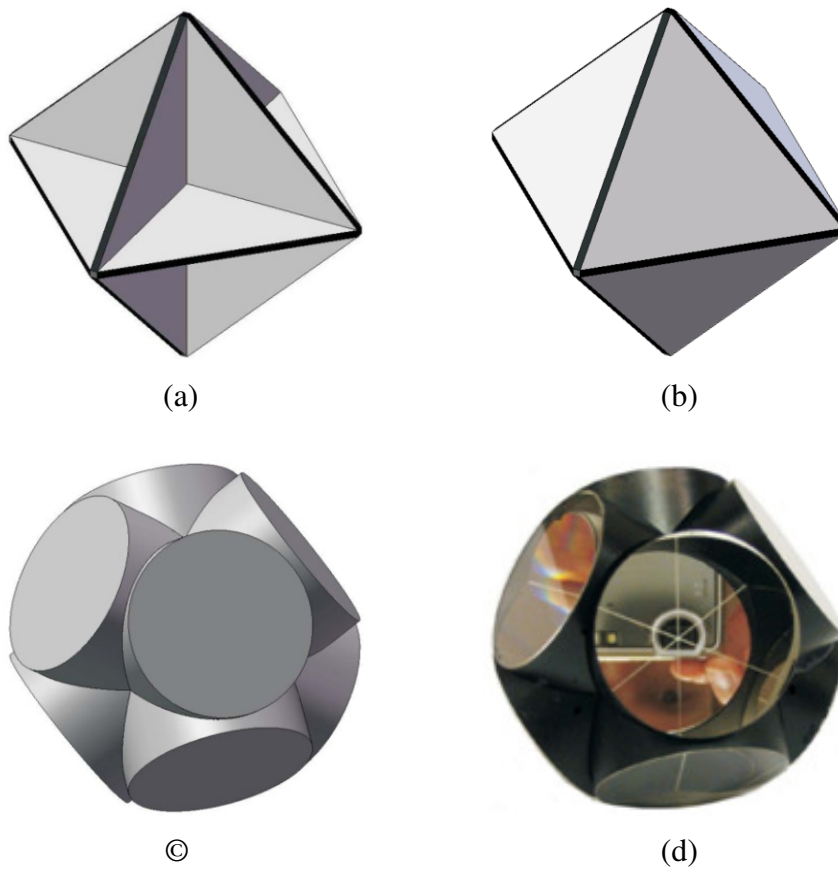


Figure 2.5 SolidWorks retroreflector schematics. They are the (a) composite hollow retroreflector, (b) composite solid retroreflector, and (c) beveled composite retroreflector. A device photograph is shown in (d).

2.4.1. Structural Optical Response

The device to be studied is assembled by bonding eight solid silica CCRs back-to-back with silicone adhesive. The resulting structure is shown in the photograph of Fig. 2.5(d). To test the angular retroreflective power of the proposed composite retroreflector, we mount the assembled design onto a gyroscope which allows for independent rotation in both the ϕ and θ orientations.

The retroreflected power is investigated by way of both a broad spectral source (a white light source) and a monochromatic source (a 632 nm laser) in the experimental setup shown in Fig. 2.6. The laser beam is expanded and collimated by a confocal lens-pair to a sufficiently large and near-uniform spot size, and the white light beam is collimated by a parabolic back-reflector. Both beams propagate 1 m and are independently directed through an R/T = 10/90 beamsplitter onto the beveled composite solid retroreflector. The back-reflected power is collected from the returning beam with the afore-mentioned beamsplitter and sampled by a broad-spectrum silicon

photodetector. Given the large difference between the propagation length and detector size, the measured signal is found to be dominated by the backward-propagating retroreflected beam of interest, with negligible contributions from the randomized light scattering off non-mirrored surfaces of our device (approximately 0.01% of the signal). In fact, this poor scattering efficiency is one of the prime motivations for our use of retroreflectors in bi-directional communications. Moreover, the sensitivity of the experimental setup for laser illumination is improved through the use of lock-in detection with a Stanford Research Systems SR830 Lock-in Amplifier. The incident laser beam is modulated at 1.5 kHz, and the signal detected by the silicon photodetector is locked-in to this reference frequency, such that the background signal levels are completely eliminated. With this configuration, the resulting photodetector signal is recorded as ϕ and θ are varying. For the purposes of this experiment, the retroreflecting octuplet is set at the θ value, and retroreflected powers are measured as ϕ is rotated.

Retroreflected powers for the composite beveled retroreflector are shown for white light illumination and laser illumination in Figs. 2.7(a)-(b) and (c)-(d), respectively. The profiles are presented in Figs. 2.7 (a) and (c) for θ values between 0° and 45° and Figs. 2.7 (b) and (d) for θ values between 45° and 90° . Note that the white light illumination and laser illumination responses show a similar angular dependence, and the structure effectively retroreflects power for all orientations. The characteristic curves of this retroreflection are seen to be a strong function of the θ values, and the retroreflected power variations are greatest when $\theta = 45^\circ$. The retroreflected power at this θ value forms a series of four maxima and four minima over the range of ϕ values (similar to the theoretical results of Fig. 2.4(b)). Interestingly, the small subpeaks in the troughs of the model results are not present in either set of experimental measurements, and their absence is attributed to the extreme nature of the incident ray angles at these points. At such orientations, reflections from the aluminum mirrors occur at glancing angles, and the angular dependence of this reflection is not included in the idealized model. For polar angles beyond $\theta = 45^\circ$, the ϕ -dependent variations are seen to diminish. This observation is a result of the fact that the structure, as viewed from the source, varies greatly with ϕ when $\theta = 45^\circ$ and would give the symmetrical retroreflection pattern with any ϕ rotations when $\theta = 90^\circ$. These overall characteristics are witnessed in both the white light and laser illumination results, though minor variations are observed between these illumination data sets and are attributed to the improved sensitivity and background-free nature of the lock-in detection system used for the laser results.

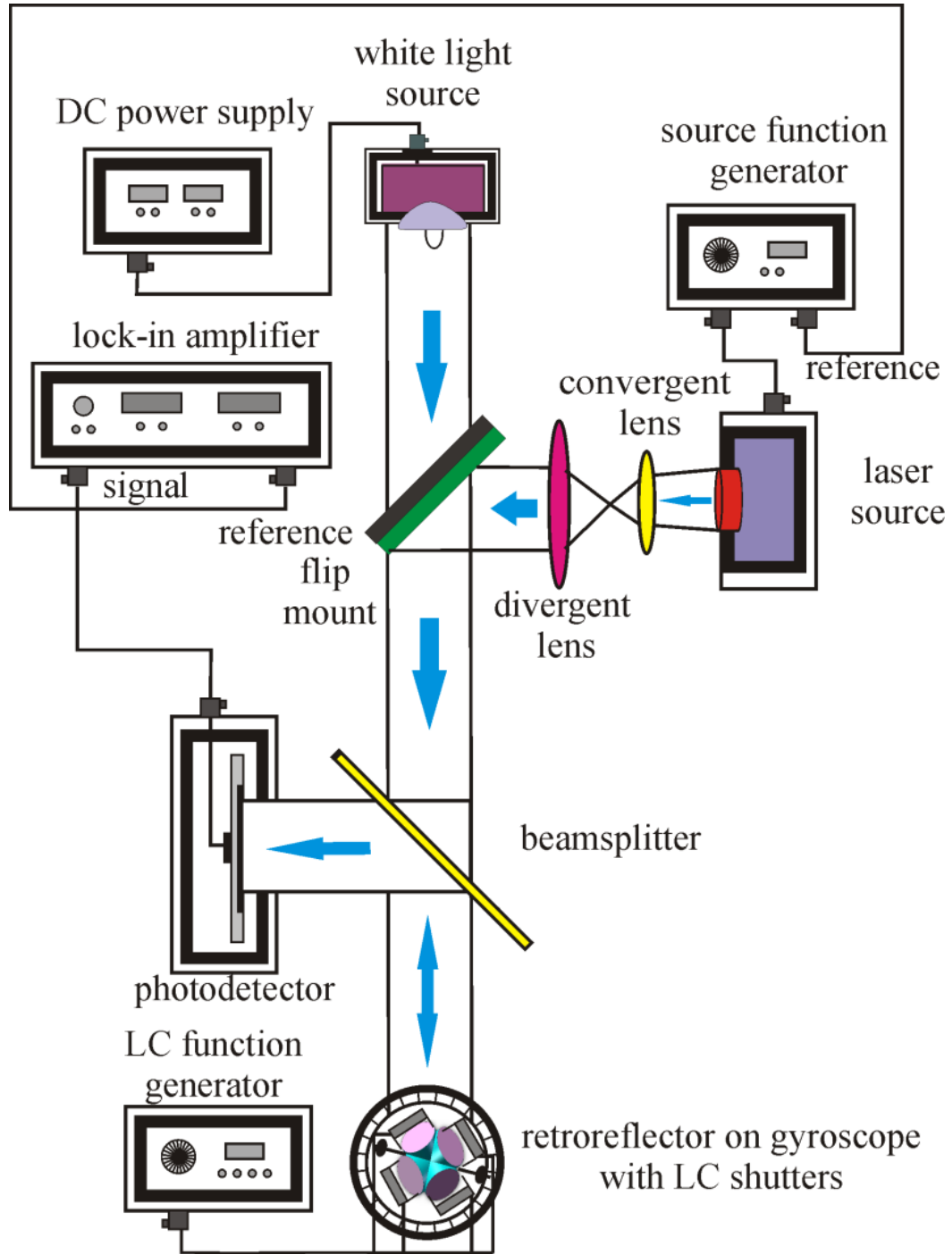
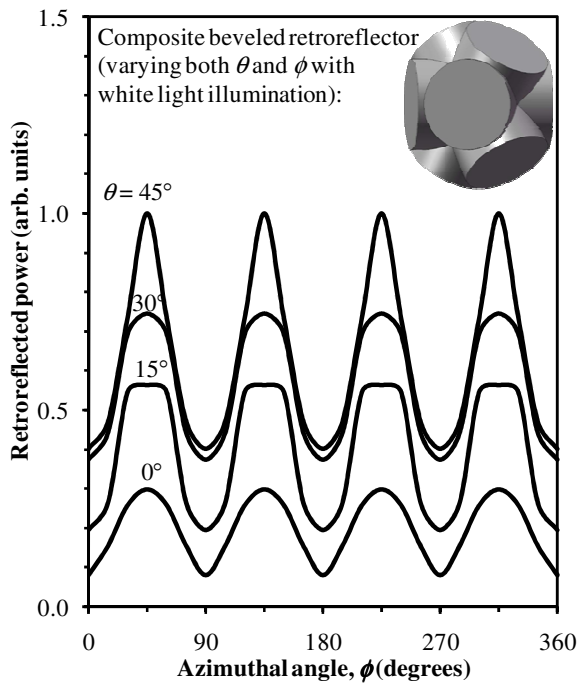
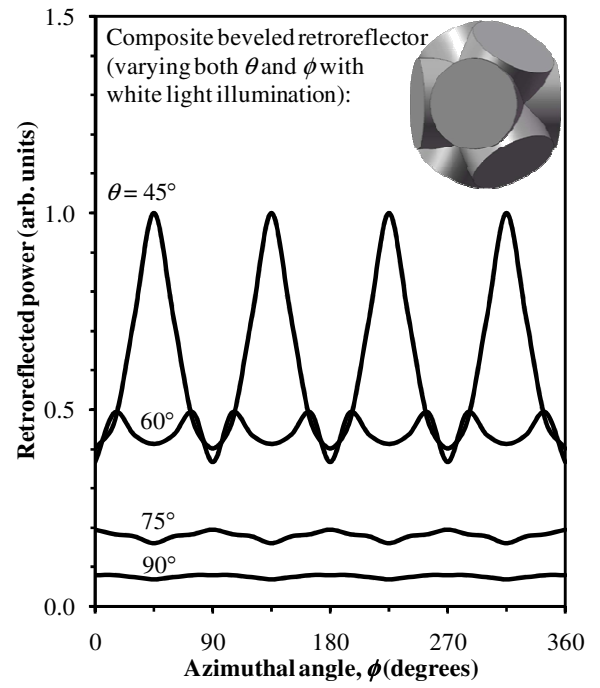


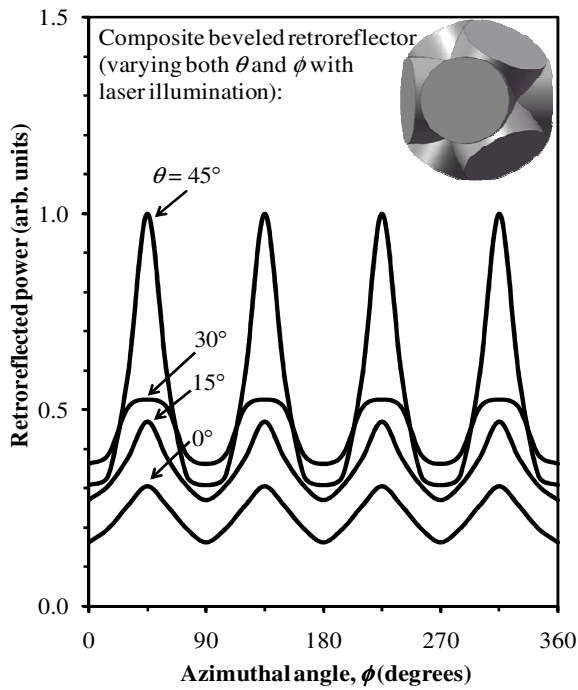
Figure 2.6 The experimental system for measuring the retroreflected optical response is shown. Light from the optical sources is expanded to create sufficiently uniform and collimated beams. The beams are then directed onto the retroreflector of interest with near-uniform beam intensity. The back-reflected optical power is sampled by a beamsplitter and large-area silicon detector.



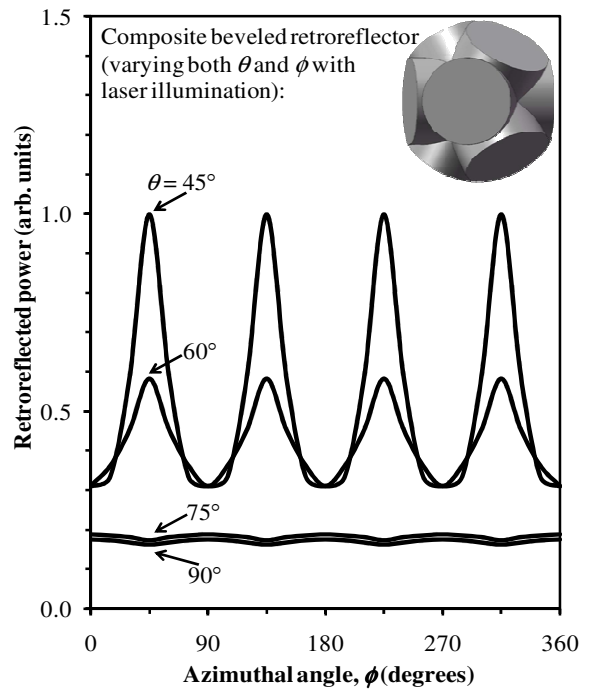
(a)



(b)



(c)



(d)

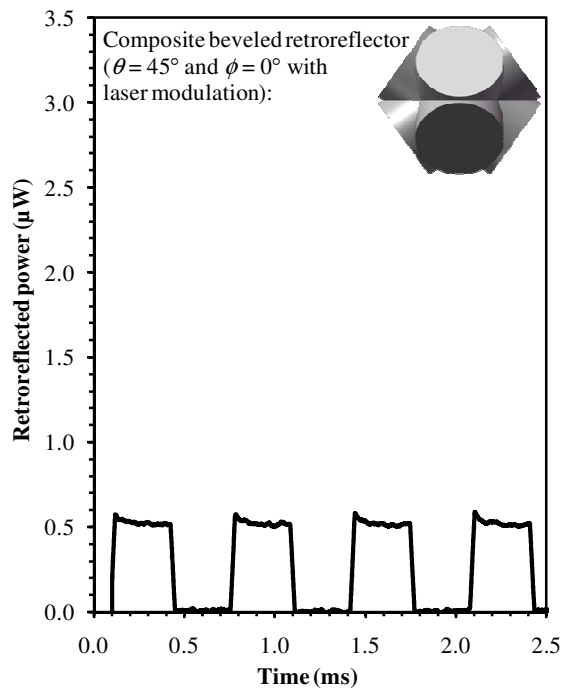
Figure 2.7 Experimental retroreflected power as a function of azimuthal angle ϕ for the composite beveled retroreflector. It is shown for the (a)-(b) white light illumination and a (c)-(d) near-uniform laser illumination both with a propagation length of 1 meter. The polar angle θ ranges from 0° to 45° for (a) and (c) and 45° to 90° for (b) and (d), respectively.

2.4.2. Optical Communication and Modulation Capability

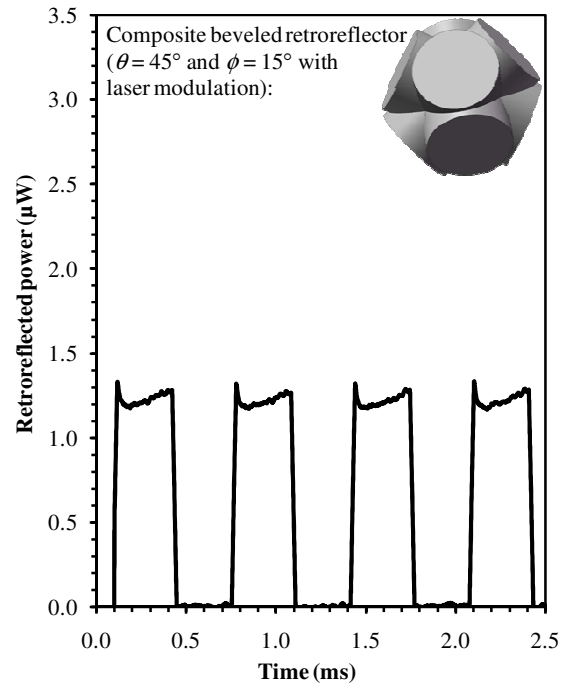
The composite optical device characterized in the previous subsection is an intriguing structure for an FSO communication link, as such a structure can provide multi-directionality for signal transmission and reception. With this in mind, an important property for these effective FSO systems is the ability for dynamic control by way of modulation. This optical switching process encodes the required information. For such an FSO communication system, this modulation is typically achieved in an active modulation configuration (with laser beams directly encoded with signal information) or a passive modulation configuration (with continuous laser beams and modulation of the retroreflected power). These configurations are demonstrated here for the proposed composite solid retroreflector.

The active configuration is analyzed first with a system employing a laser beam modulated at 1.5 kHz. The experimental setup has been introduced in Fig. 2.6, and the experimental retroreflected power as a function of azimuthal angle ϕ for the composite beveled retroreflector was shown in Fig. 2.7(c)-(d) of the previous subsection. The related time-domain waveforms for orientations of $\phi = 0^\circ, 15^\circ, 30^\circ,$ and 45° at a polar angle of $\theta = 45^\circ$, respectively, are shown in Figs. 2.8(a)-(d), and the Solidworks schematic of the composite retroreflector in the figure insets shows the structure at the respective orientations as viewed by the laser source. It is readily apparent that the directly-modulated laser signals are effectively mapped onto the retroreflected beam powers and are associated with an appreciable depth of modulation. The retroreflected power levels monotonically increase as ϕ varies from 0° to 45° . The troughs appearing at the top of square waveform are attributed to the finite bandwidth of the system (and witnessed by way of this Gibb's phenomenon).

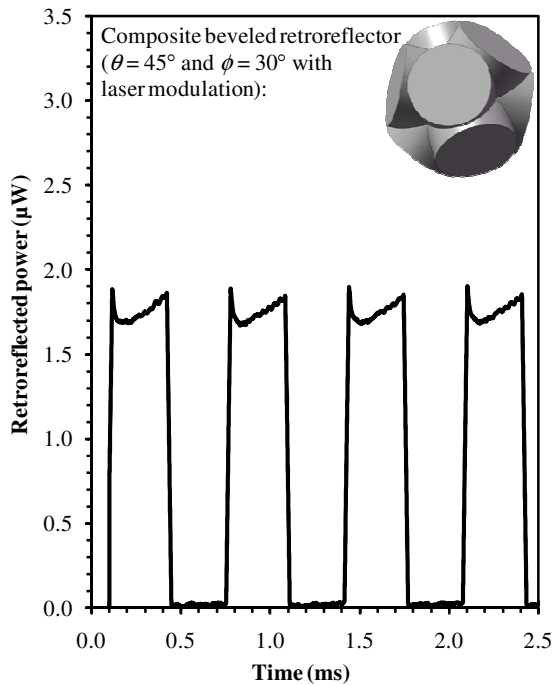
In contrast to the results above, bi-directional configurations typically employ CCRs in passive modulation communication with LC optical modulators encoding information onto the retroreflected beam before it is returned to the laser transceiver [7, 11]. Advantages of these LC CCR systems include a minimal positional dependence, low operational voltages, and high optical switching contrast ratios. If these systems are applied in three-dimensional omnidirectional configurations, however, it becomes necessary to employ both a structure that is capable of retroreflecting at all incident angles (as demonstrated in subsection 2.4.1) and a modulation technique that is capable of switching at all incident angles (as will be shown here using LC modulation).



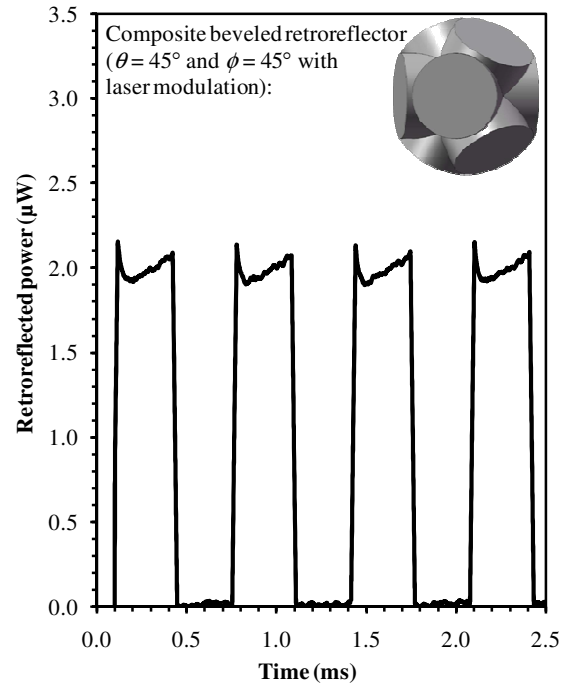
(a)



(b)



(c)



(d)

Figure 2.8 The retroreflective power levels are shown as a function of time for the composite beveled retroreflector. It is illuminated by a laser beam modulated at 1.5 kHz with a power of 0.15 mW and a propagation length of 1 meter. The modulated power signals are shown as a function of time for orientations with (a) $\phi = 0^\circ$, (b) $\phi = 15^\circ$, (c) $\phi = 30^\circ$ and (d) $\phi = 45^\circ$ at a polar angle of $\theta = 45^\circ$.

The composite beveled retroreflector is adapted for LC modulation by mounting optical shutters over the CCR entrance interfaces. The optical shutters that are used are based on Pi-cell polarization-modulation as opposed to the standard TN modulation, as the Pi-cell configuration is characterized by faster activation and recovery times (See Appendix A). The angular dependence of this optical switching process is analyzed here by recording time-domain modulation results with the LC modulators. The profiles of the time-domain waveforms with Pi-cell LC shutter modulation at 150 Hz of a near-uniform continuous laser beam are shown in Figs. 2.9 (a)-(b) and 2.10 (a)-(b) corresponding to ϕ values of 0° , 15° , 30° , and 45° at a polar angle of $\theta = 45^\circ$, respectively. Solidworks schematics of composite retroreflectors in the figure insets show the structure at the respective orientations as viewed by the laser source. All LC modulation results at the presented orientations show appreciable retroreflected signal levels, and the peak values for these signals grow as ϕ is increased. This trend is a consequence of two simultaneous responses:

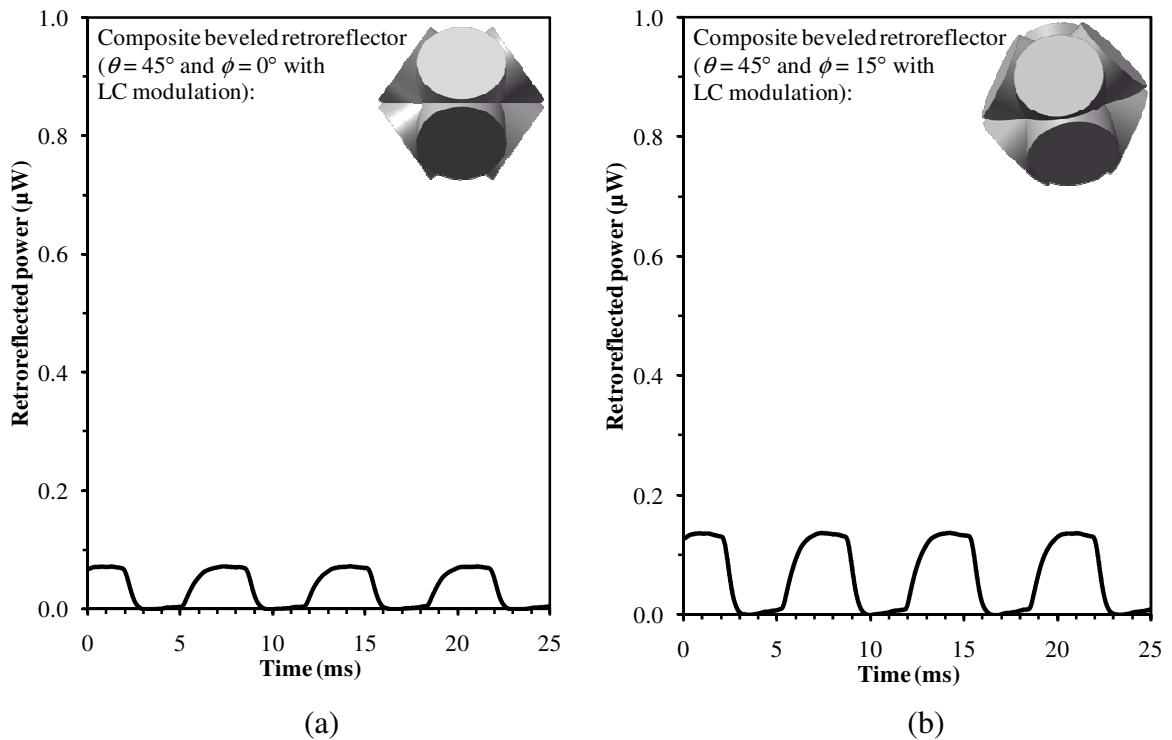


Figure 2.9 Passive uplink mode modulated retroreflective signals are shown as a function of time for the composite beveled retroreflector. It is illuminated by a continuous laser with a power of 0.15 mW and a propagation length of 1 meter and Pi-cell LC optical modulators (not shown in the insets). The modulated power signals are shown as a function time for orientations with (a) $\phi = 0^\circ$ and (b) $\phi = 15^\circ$ at a polar angle of $\theta = 45^\circ$.

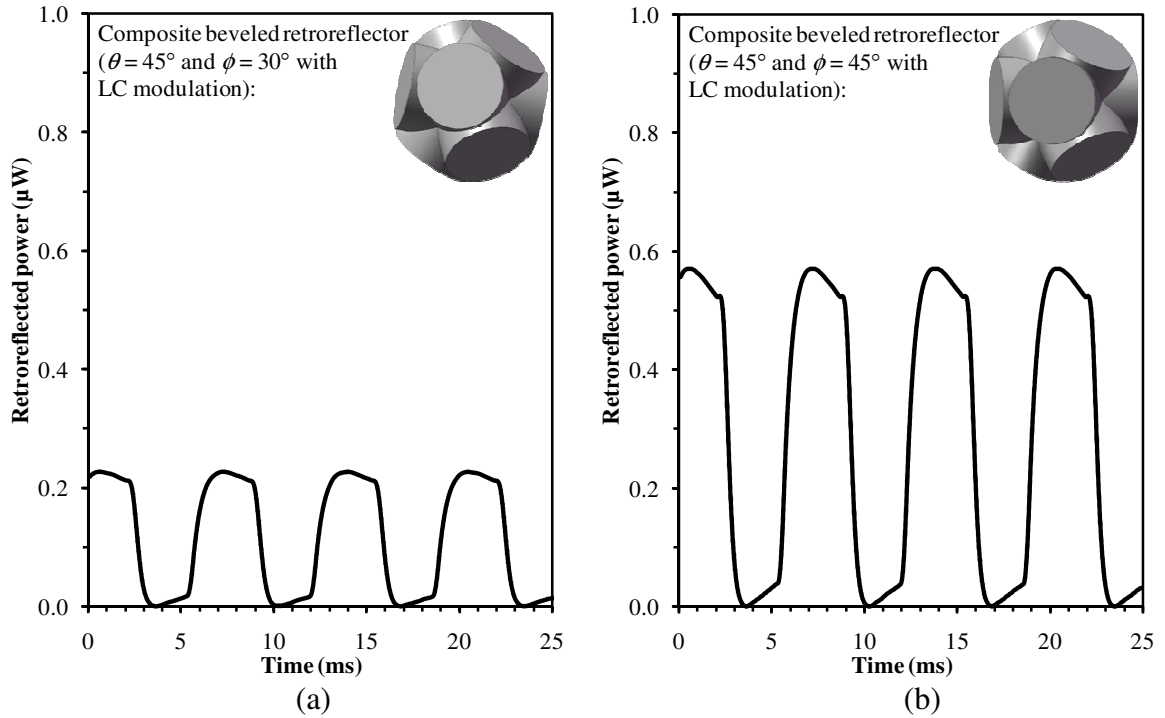


Figure 2.10 Passive uplink mode modulated retroreflective signals are shown as a function of time for the composite beveled retroreflector. It is illuminated by a continuous laser with a power of 0.15 mW and a propagation length of 1 meter and Pi-cell LC optical modulators (not shown in the insets). The modulated power signals are shown as a function time for orientations with (a) $\phi = 30^\circ$ and (b) $\phi = 45^\circ$ at a polar angle of $\theta = 45^\circ$.

- i. the retroreflected power of the composite structure increases as ϕ increases, and
- ii. the LC modulation depth improves as ϕ approaches 45° due to the inherent nature of Pi-cell.

At this 45° orientation the light rays are at near-normal incidence to the LC shutters (approximately 10° off the normal), the capability of polarization modulation is near to its optimal value, and the observed retroreflected passive modulation is appreciable.

2.5. Summary

In summary, the composite retroreflector that was introduced here was shown to return incident optical power for all combinations of ϕ and θ . The angular dependence of the structure was analyzed with a Matlab ray-tracing model, and these theoretical analyses were found to be in

excellent agreement with the collected experimental data. The composite structure presented here was the first demonstration of an element capable of complete retroreflection over all angles. The omni-directionality of the composite retroreflector was then applied to modulation with active and passive communication configurations. Modulation results of the composite structure were tested with Pi-cell LC shutters over the CCR entrance interfaces. The complete composite optical modulator/retroreflector was highly successful in encoding local modulation signals onto the retroreflected optical beam.

Chapter 3

Integrated Device: A Corner-Cube-Based Optical Control and Communication System

In this chapter, a control-based extension of the previous omni-directional retroreflective implementations is introduced as a novel instrument for FSO communication applications. The fundamental requirements for optical retroreflection, detection, and modulation are all met within one integrated structure. The structure consists of three independent and mutually perpendicular optically-active PDs arranged within an interior corner. The photodetection capabilities of these PDs bring about numerous advantages for both active downlink and passive uplink FSO links. In particular, the novel technique, defined here as retro-detection, has bi-directional communication capabilities and the ability for active-control (via differential triangulation technology). The retro-detection system is demonstrated here through both theoretical model results and experimental testing with excellent agreement.

3.1. Background

FSO systems have the same high-speed benefits as their fibre optic counterparts [15], with additional benefits witnessed in applications on short scales with variable user endpoints. In these distributed systems, FSO signals can be broadcasted throughout the communication environment for optical wireless networking [16]. The challenges associated with this optical signal distribution are addressed in this work, and the FSO link angular coverage is seen to be optimized by the new photodetection technique. Interestingly, the work is also a significant extension of remote sensing technologies.

Remote sensing is the basis for probing external environments, and improvements in this sensing have followed the development of various signal emission and detection technologies.

At the heart of remote sensing is the capability of these instruments to successfully gather information from distributed targets by way of passive remote sensing [17-20] and active remote sensing [21-24].

Passive remote sensing describes a system in which uni-directional information is gathered from the external environment. Typically, natural or artificial targets emit/reflect visible, infrared (IR), or RF signals that are detected by a passive sensor network. Charge coupled devices (CCD) [25] and complementary metal oxide semiconductor (CMOS) sensors [26] are classic examples of such a passive system for visible/IR spectra. Global positioning systems (GPSs) are an example of passive reception in the RF regime [27, 28]. Ultimately, the selected technology must be appropriate for the scale of the desired detection environment, with long wavelength RF systems being well-suited to global scales and short wavelength optical systems being better-suited to applications requiring high sensitivities and small spatial resolutions.

Active remote sensing differs from its passive remote sensing counterpart through its increased level of control and bi-directional implementation. Active remote sensing employs signal emission, reflection, and detection to scan objects in an external environment. The emitted and subsequently reflected/backscattered signals can be an effective probe of the remote target properties, as the source characteristics can be controlled (through modulation, polarization, wavelength, etc.) to improve the signal sensitivity. This principle has been successfully applied in long-wavelength remote sensing applications such as millimeter-wave radar [29], short range radar [30], and even mid-IR terahertz (THz) imaging [31] and radar ranging [32].

In the work presented here, a new architecture is introduced to extend the capabilities of active remote sensing. The proposed active corner-cube target allows for simultaneous retro-reflection of incident signals back to their source and local detection of the incident power levels. Moreover, the employed integrated PD structure is capable of real-time sensing for control and optimization of the optical alignment. Unlike standard PD [33] and photoconductive [34] switching technologies, which record a single magnitude for the incident optical power, the retro-detection structure is able to simultaneously record the total incident optical power *and* its direction of incidence by way of differential channel sampling. Moreover, the implemented structure allows the operation in both active and passive FSO bi-directional communications (by simultaneously offering optical signal retroreflection, detection and modulation in one device). The control and communication characteristics of this integrated retro-detection photocell prototype are demonstrated here theoretically and experimentally with excellent agreement.

3.2. System Design and Operation

The integrated retro-detection device of interest to this investigation is assembled as the corner-cube-based photocell shown in Fig. 3.1. The device is fabricated out of three mutually-orthogonal silicon PDs that are $9.7 \times 9.7 \text{ mm}^2$ in size. The PDs are aligned as an interior corner, with PD₁ lying in the yz -plane, PD₂ lying in the xz -plane, and PD₃ lying in the xy -plane. Moreover, a high-speed Pi-cell LC optical modulator is bonded to the retro-detection photocell entrance interface to modulate both incident and retroreflected optical beams.

The orthogonal nature of the integrated retro-detector provides a distinct retroreflecting characteristic which allows incident light to be reflected directly back to its source. This is accomplished through three internal reflections off of the three constituent PDs, whose active regions are electrically-isolated. Interestingly, the employment of PDs offers a unique opportunity to probe the power levels of incident light by sampling the non-reflected fraction of the beam power. The three resulting photocurrents are recorded as $i_1(t)$, $i_2(t)$, and $i_3(t)$, as shown in Fig. 3.1, with each corresponding to PD₁, PD₂, and PD₃, respectively. The sum of these photocurrents provides a measure of the total incoming optical signal power level.

The constituent photocurrents of the integrated retro-detection system play an important role in triangulating the incoming optical signal orientations, and the differential combinations of these photocurrents can ultimately offer an effective mechanism for this differential optimization and triangulation of the incident light directions by way of the azimuthal angle ϕ and polar angle θ . The differential photocurrents are defined here as

$$\begin{aligned}i_{1-2}(t) &= i_1(t) - i_2(t) \\i_{1-3}(t) &= i_1(t) - i_3(t) \\i_{2-3}(t) &= i_2(t) - i_3(t).\end{aligned}\tag{5}$$

These differential signals are related to the azimuthal ϕ and polar θ orientations and can be used to optimize the beam alignment as follows. Typically, ϕ is optimized first during a 0° to 90° rotation. Over this range, the PD₁ photocurrent diminishes from its full-illumination maximum down to its negligible-illumination minimum, while the PD₂ photocurrent rises from its negligible-illumination minimum up to its full-illumination maximum. It is apparent that the system must be rotated and re-aligned in the xy -plane by a careful tracking of the differential photocurrent between PD₁ and PD₂, and the $\phi = 45^\circ$ midpoint gives a balanced differential

photocurrent with $i_{1-2}(t) = 0$. This condition indicates an optimal alignment for ϕ . In the next control phase, the same optimization process is employed to balance θ while monitoring both $i_{1-3}(t)$ and $i_{2-3}(t)$. When all these differential photocurrents are zero, i.e. $i_{1-2}(t) = i_{2-3}(t) = i_{1-3}(t) = 0$, this perfect optical alignment orients the system with the incident light rays entering the corner along the azimuthal angle $\phi = 45^\circ$ and the polar angle $\theta = \cos^{-1}(1/\sqrt{3}) \approx 54.7^\circ$, where this photocell is now oriented with its $(x, y, z) = (1,1,1)$ coordinate aligned directly toward the illumination source. Thus, it is possible to monitor the system for conditions in which one or more differential photocurrents are not equal to zero, $i_{1-2}(t)$ or $i_{2-3}(t)$ or $i_{1-3}(t) \neq 0$, and the photocell is exhibiting optical misalignment.

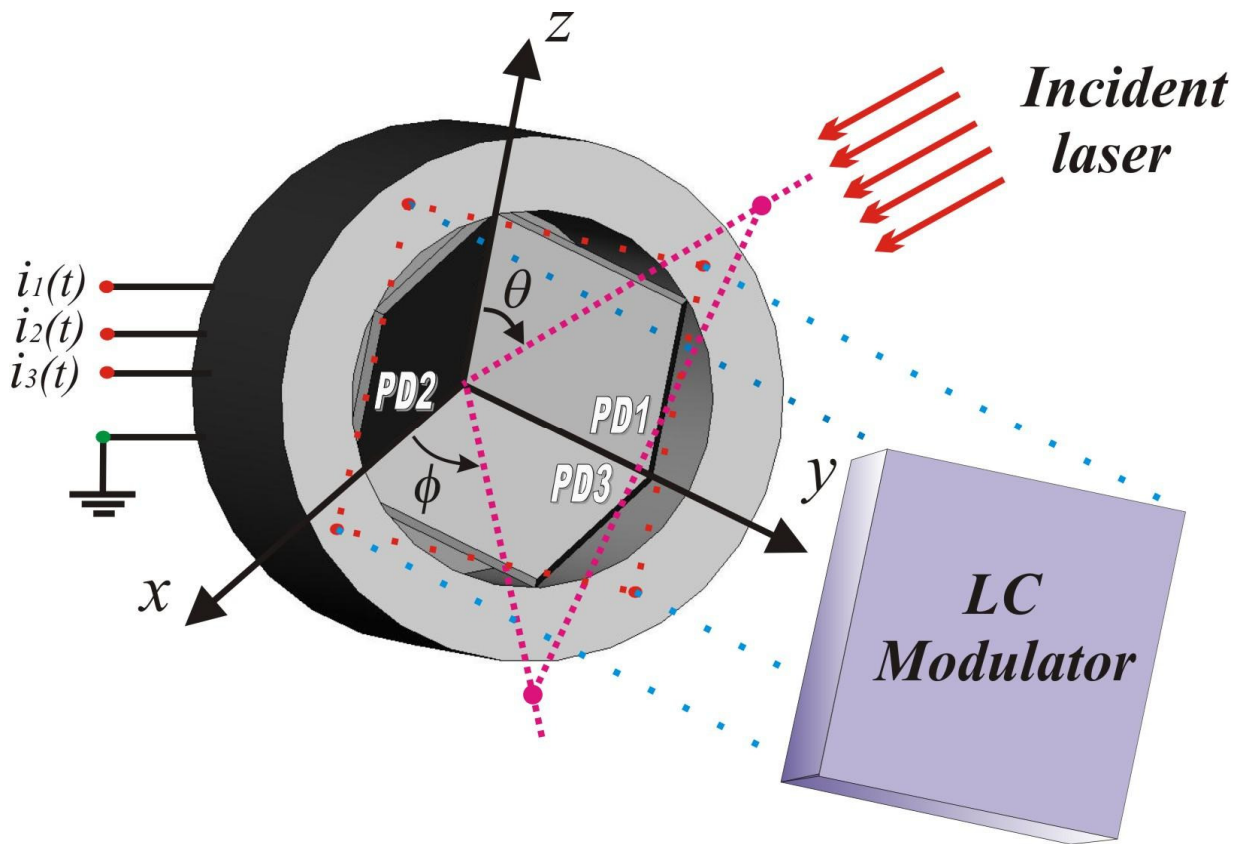


Figure 3.1 SolidWorks schematic of the integrated retro-detection photocell. The structure consists of three mutually-orthogonal silicon PDs arranged in the form of an interior corner. Differential photocurrents recorded by the PDs are capable of triangulating the incident light source with respect to the azimuthal angle ϕ and the polar angle θ . Moreover, a Pi-cell LC modulator is mounted at the entrance interface for optical modulation.

3.3. Theoretical Framework

In the previous section, the proposed integrated photocell shown in Fig. 3.1 was introduced. The geometrical nature of this architecture allows it to act as a retro-reflector by reflecting a fraction of the incident light back to its source, while local sensing is facilitated by the use of PDs (as the non-reflected fraction of incident light can be sampled and summed to probe the incident light levels and orientations). Ultimately, the geometrical and active PD construction together provides a method for differentiating between orthogonal components of the incident light intensity levels, and this offers an effective mechanism for differential optimization, realignment, and control. The theory and methodology for the angular response of these reflection, detection, and control characteristics are presented in detail within the following subsections.

3.3.1. Retroreflection Characteristics

Active remote sensing targets must effectively redirect large fractions of incident light back to their respective sources. A suitable structure for accomplishing this reflection is the standard CCR. Such an architecture consists of three reflective surfaces that are mutually-perpendicular and orientated as an interior corner (as shown in Fig. 3.1). When incident light enters the corner along the unit-normal vector

$$\hat{r} = -n_1\hat{x} - n_2\hat{y} - n_3\hat{z}, \quad (6)$$

it undergoes a series of reflections, reversing the n_1 , n_2 and n_3 incident ray directional cosines in the x , y , and z directions, respectively. The uniform incident intensity,

$$I_0\hat{r}_1 = -I_0n_1\hat{x} - I_0n_2\hat{y} - I_0n_3\hat{z}, \quad (7)$$

for a uniform intensity magnitude of I_0 leads to intensities of

$$\begin{aligned} \bar{I}_1 &= +RI_0n_1\hat{x} - RI_0n_2\hat{y} - RI_0n_3\hat{z} \\ \bar{I}_2 &= -RI_0n_1\hat{x} + RI_0n_2\hat{y} - RI_0n_3\hat{z} \\ \bar{I}_3 &= -RI_0n_1\hat{x} - RI_0n_2\hat{y} + RI_0n_3\hat{z}, \end{aligned} \quad (8)$$

after the light undergoes reflections from PD₁, PD₂, and PD₃, respectively. The angular-independent surface reflectivity here is denoted by R . After three successful internal reflections, light exits the corner-cube anti-parallel to the incident ray with an intensity defined by

$$-I_0R^3\hat{r} = +I_0R^3n_1\hat{x} + I_0R^3n_2\hat{y} + I_0R^3n_3\hat{z}. \quad (9)$$

The degree to which this structure acts as a retro-reflector can be quantified by the reflection solid angle subtended by the azimuthal angle ϕ and polar angle θ . The definitions for these angles have been shown in Fig. 3.1 along with the directional cosine components

$$\begin{aligned} n_1 &= \cos\phi \cdot \cos\theta \\ n_2 &= \sin\phi \cdot \cos\theta \\ n_3 &= \sin\theta. \end{aligned} \quad (10)$$

The retro-reflective response of this corner-cube structure has been successfully applied to short [35] and long [36] range bi-directional applications, and the angular analysis for the retro-reflection directionality is shown elsewhere [37].

3.3.2. Detection Characteristics

The desired optical detection process for the proposed retro-detector is fundamentally based on the use of three orthogonal silicon PDs. The incident light with a uniform intensity illuminates the element shown in Fig. 3.1 and (typically) leads to three PD photocurrents with differing amplitudes. The disparity between these amplitudes is due to imbalances between the incident light ray directional cosine components. Each PD will have a differing cross-sectional area as viewed from the source: incident light with a large n_1 component along the x -axis will preferentially illuminate PD₁; incident light with a large n_2 component along the y -axis will preferentially illuminate PD₂; and incident light with a large n_3 component along the z -axis will preferentially illuminate PD₃. Quantifying this relationship becomes further complicated by the fact that the recorded PD photocurrents will also have contributions from light rays after primary and secondary internal reflections. The complete theoretical model for the PD photocurrents, including these internal reflections, is developed in this detection characteristics subsection. Power levels incident upon PD₁, PD₂, and PD₃ are investigated as three individual responses with results defined in terms of six illumination condition cases: (1) $n_1 < n_2 < n_3$, (2) $n_1 < n_3 < n_2$, (3) $n_2 < n_1 < n_3$, (4) $n_2 < n_3 < n_1$, (5) $n_3 < n_1 < n_2$, and (6) $n_3 < n_2 < n_1$. Each of these cases is,

itself, characterized by six individual subcases, where the photocurrent levels will depend upon the ordering of the primary and secondary reflections. All of these thirty-six conditions for incident angle permutations are successively analyzed in the following subsections.

3.3.2.1. Detected Power Levels for the First Illumination Case with $n_1 < n_2 < n_3$

The first analysis case corresponds to incident illumination with the x , y , and z directional cosine components in increasing order of magnitudes. This $n_1 < n_2 < n_3$ situation is analyzed for the first subcase, in which the incident light strikes PD₁, reflects onto PD₂, and reflects onto PD₃ (and subsequently exits the retro-detector to return to its source). In this case, the light ray unit-normal vectors that are incident on PD₁, PD₂ and PD₃ are

$$\begin{aligned}\hat{r}_1 &= -n_1\hat{x} - n_2\hat{y} - n_3\hat{z} \\ \hat{r}_{12} &= +n_1\hat{x} - n_2\hat{y} - n_3\hat{z} \\ \hat{r}_{123} &= +n_1\hat{x} + n_2\hat{y} - n_3\hat{z},\end{aligned}\tag{11}$$

respectively, where the subscripts indicate the successive illumination and reflection sequence. Fig. 3.2(a) shows the resulting illumination areas for this subcase. Here, PD₁ is fully illuminated and shaded, and its four corner points in the yz -plane are projected along \hat{r}_{12} onto the xz -plane. The resulting shaded PD₂ illumination area is then defined as the overlap between this projected area and the PD₂ surface. Similarly, the PD₂ illumination area is projected along \hat{r}_{123} onto the xy -plane, and the shaded PD₃ illumination is defined as the overlap between this projected area and the PD₃ surface. The resulting illumination area normal vectors can now be defined for this subcase as

$$\begin{aligned}\bar{A}_1 &= a^2\hat{x} \\ \bar{A}_{12} &= a^2\frac{n_1}{2n_3}\hat{y} \\ \bar{A}_{123} &= a^2\frac{n_1n_2}{2n_3^2}\hat{z}.\end{aligned}\tag{12}$$

The corresponding incident power levels associated with PD₁, PD₂ and PD₃ are then found by taking the component of these illumination area normal vectors in (12) along the respective reflected light ray unit-normal vectors in (11). The result is

$$P_1 = -I_0\hat{r}_1 \cdot \bar{A}_1 = I_0a^2n_1$$

$$\begin{aligned}
P_{12} &= -RI_0 \hat{r}_{12} \cdot \bar{A}_{12} = RI_0 a^2 \frac{n_1 n_2}{2n_3} \\
P_{123} &= -R^2 I_0 \hat{r}_{123} \cdot \bar{A}_{123} = R^2 I_0 a^2 \frac{n_1 n_2}{2n_3}.
\end{aligned} \tag{13}$$

The second subcase for $n_1 < n_2 < n_3$ corresponds to the situation with the incident light illuminating PD₁, PD₃, and PD₂, in order. In this case, the respective light ray unit-normal vectors incident on the surfaces of PD₁, PD₃ and PD₂ are

$$\begin{aligned}
\hat{r}_1 &= -n_1 \hat{x} - n_2 \hat{y} - n_3 \hat{z} \\
\hat{r}_{13} &= +n_1 \hat{x} - n_2 \hat{y} - n_3 \hat{z} \\
\hat{r}_{132} &= +n_1 \hat{x} - n_2 \hat{y} + n_3 \hat{z}.
\end{aligned} \tag{14}$$

Again, the successive illumination areas are referred onto their adjoining neighbors, and the illumination areas are displayed in Fig. 3.2(b) (shown for $n_3 < 2n_2$). Using the shaded areas on this figure, the illumination area normal vectors can be defined as

$$\begin{aligned}
\bar{A}_1 &= a^2 \hat{x} \\
\bar{A}_{13} &= a^2 \left(\frac{n_1}{n_3} - \frac{n_1 n_2}{2n_3^2} \right) \hat{z} \\
\bar{A}_{132} &= a^2 \begin{cases} \left(2 \frac{n_1}{n_2} - \frac{n_1}{n_3} - \frac{n_1 n_3}{2n_2^2} \right) \hat{y}, n_3 < 2n_2 \\ \frac{n_1}{n_3} \hat{y}, n_3 > 2n_2 \end{cases}.
\end{aligned} \tag{15}$$

The corresponding incident power levels associated with PD₁, PD₃ and PD₂ are then found by taking the component of these illumination area normal vectors from (15) along the respective reflected light ray unit-normal vectors from (14). The result is

$$\begin{aligned}
P_1 &= -I_0 \hat{r}_1 \cdot \bar{A}_1 = I_0 a^2 n_1 \\
P_{13} &= -RI_0 \hat{r}_{13} \cdot \bar{A}_{13} = RI_0 a^2 \left(n_1 - \frac{n_1 n_2}{2n_3} \right) \\
P_{132} &= -R^2 I_0 \hat{r}_{132} \cdot \bar{A}_{132} \\
&= R^2 I_0 a^2 \begin{cases} \left(2n_1 - \frac{n_1 n_2}{n_3} - \frac{n_1 n_3}{2n_2} \right), n_3 < 2n_2 \\ \frac{n_1 n_2}{n_3}, n_3 > 2n_2 \end{cases}.
\end{aligned} \tag{16}$$

The third subcase for $n_1 < n_2 < n_3$ is shown in Fig. 3.2(c), and it is characterized by illumination of PD₂, followed by subsequent reflections off PD₁ and PD₃. The light ray unit-normal vectors incident on the surfaces of PD₂, PD₁, and PD₃, respectively, are

$$\begin{aligned}\hat{r}_2 &= -n_1\hat{x} - n_2\hat{y} - n_3\hat{z} \\ \hat{r}_{21} &= -n_1\hat{x} + n_2\hat{y} - n_3\hat{z} \\ \hat{r}_{213} &= +n_1\hat{x} + n_2\hat{y} - n_3\hat{z}.\end{aligned}\tag{17}$$

Using these light ray components and the resulting illumination area projections, the respective illumination area normal vectors can be written for PD₂, PD₁, and PD₃ as

$$\begin{aligned}\bar{A}_2 &= a^2\hat{y} \\ \bar{A}_{21} &= a^2\frac{n_2}{2n_3}\hat{x} \\ \bar{A}_{213} &= a^2\frac{n_1n_2}{2n_3}\hat{z}.\end{aligned}\tag{18}$$

The resulting incident power levels associated with PD₂, PD₁, and PD₃ are then found by taking the component of the illumination area normal vectors from (18) along the respective reflected light ray unit-normal vectors from (17), such that

$$\begin{aligned}P_2 &= -I_0\hat{r}_2 \cdot \bar{A}_2 = I_0a^2n_2 \\ P_{21} &= -RI_0\hat{r}_{21} \cdot \bar{A}_{21} = RI_0a^2\frac{n_1n_2}{2n_3} \\ P_{213} &= -R^2I_0\hat{r}_{213} \cdot \bar{A}_{213} = R^2I_0a^2\frac{n_1n_2}{2n_3}.\end{aligned}\tag{19}$$

The fourth subcase for $n_1 < n_2 < n_3$ is shown in Fig. 3.2(d), and it corresponds to the case for which PD₂, PD₃, and PD₁ are successively illuminated. The respective light ray unit-normal vectors incident on PD₂, PD₃, and PD₁ can be expressed as

$$\begin{aligned}\hat{r}_2 &= -n_1\hat{x} - n_2\hat{y} - n_3\hat{z} \\ \hat{r}_{23} &= -n_1\hat{x} + n_2\hat{y} - n_3\hat{z} \\ \hat{r}_{231} &= -n_1\hat{x} + n_2\hat{y} + n_3\hat{z},\end{aligned}\tag{20}$$

and the PD₂, PD₃, and PD₁ illumination area normal vectors are

$$\bar{A}_2 = a^2\hat{y}$$

$$\begin{aligned}\bar{A}_{23} &= a^2 \left(\frac{n_2}{n_3} - \frac{n_1 n_2}{2n_3^2} \right) \hat{z} \\ \bar{A}_{231} &= a^2 \begin{cases} \left(2 - \frac{n_2}{n_3} - \frac{n_3}{2n_2} \right) \hat{x}, n_3 < 2n_2 \\ \frac{n_2}{n_3} \hat{x}, n_3 > 2n_2 \end{cases}.\end{aligned}\quad (21)$$

The PD₂, PD₃, and PD₁ incident powers are then found by taking the illumination area normal vector components in (21) along the reflected light ray unit-normal vectors in (20), giving

$$\begin{aligned}P_2 &= -I_0 \hat{r}_2 \cdot \bar{A}_2 = I_0 a^2 n_2 \\ P_{23} &= -R I_0 \hat{r}_{23} \cdot \bar{A}_{23} = R I_0 a^2 \left(n_2 - \frac{n_1 n_2}{2n_3} \right) \\ P_{231} &= -R^2 I_0 \hat{r}_{231} \cdot \bar{A}_{231} \\ &= R^2 I_0 a^2 \begin{cases} \left(2n_1 - \frac{n_1 n_2}{n_3} - \frac{n_1 n_3}{2n_2} \right), n_3 < 2n_2 \\ \frac{n_1 n_2}{n_3}, n_3 > 2n_2 \end{cases}.\end{aligned}\quad (22)$$

The fifth subcase for $n_1 < n_2 < n_3$ has illumination and reflection conditions shown in Fig. 3.2(e). Here, light rays are reflected in order off of PD₃, PD₁, and PD₂. The light ray unit-normal vectors incident on the surfaces of PD₃, PD₁, and PD₂ become

$$\begin{aligned}\hat{r}_3 &= -n_1 \hat{x} - n_2 \hat{y} - n_3 \hat{z} \\ \hat{r}_{31} &= -n_1 \hat{x} - n_2 \hat{y} + n_3 \hat{z} \\ \hat{r}_{312} &= +n_1 \hat{x} - n_2 \hat{y} + n_3 \hat{z},\end{aligned}\quad (23)$$

and the resulting illumination area normal vectors for illumination of PD₃, PD₁, and PD₂ are

$$\begin{aligned}\bar{A}_3 &= a^2 \hat{z} \\ \bar{A}_{31} &= a^2 \left(1 - \frac{n_2}{2n_3} \right) \hat{x} \\ \bar{A}_{312} &= a^2 \frac{n_1}{2n_3} \hat{y}.\end{aligned}\quad (24)$$

The resulting incident power levels recorded by PD₃, PD₁, and PD₂ for this subcase are then found from (23) and (24) to be

$$P_3 = -I_0 \hat{r}_3 \cdot \bar{A}_3 = I_0 a^2 n_3$$

$$\begin{aligned}
P_{31} &= -RI_0 \hat{r}_{31} \cdot \bar{A}_{31} = RI_0 a^2 \left(n_1 - \frac{n_1 n_2}{2n_3} \right) \\
P_{312} &= -R^2 I_0 \hat{r}_{312} \cdot \bar{A}_{312} = R^2 I_0 a^2 \frac{n_1 n_2}{2n_3}.
\end{aligned} \tag{25}$$

The sixth and final subcase for $n_1 < n_2 < n_3$ is displayed in Fig. 3.2(f). The surface of PD₃ is illuminated first, followed by successive reflections off of PD₂ and PD₁. The light ray unit-normal vectors for this succession are

$$\begin{aligned}
\hat{r}_3 &= -n_1 \hat{x} - n_2 \hat{y} - n_3 \hat{z} \\
\hat{r}_{32} &= -n_1 \hat{x} - n_2 \hat{y} + n_3 \hat{z} \\
\hat{r}_{321} &= -n_1 \hat{x} + n_2 \hat{y} + n_3 \hat{z}.
\end{aligned} \tag{26}$$

The resulting illumination area normal vectors and detected power levels for PD₃, PD₂, and PD₁ are

$$\begin{aligned}
\bar{A}_3 &= a^2 \hat{z} \\
\bar{A}_{32} &= a^2 \left(1 - \frac{n_1}{2n_3} \right) \hat{y} \\
\bar{A}_{321} &= a^2 \frac{n_2}{2n_3} \hat{x}
\end{aligned} \tag{27}$$

and

$$\begin{aligned}
P_3 &= -I_0 \hat{r}_3 \cdot \bar{A}_3 = I_0 a^2 n_3 \\
P_{32} &= -RI_0 \hat{r}_{32} \cdot \bar{A}_{32} = RI_0 a^2 \left(n_2 - \frac{n_1 n_2}{2n_3} \right) \\
P_{321} &= -R^2 I_0 \hat{r}_{321} \cdot \bar{A}_{321} = R^2 I_0 a^2 \frac{n_1 n_2}{2n_3}.
\end{aligned} \tag{28}$$

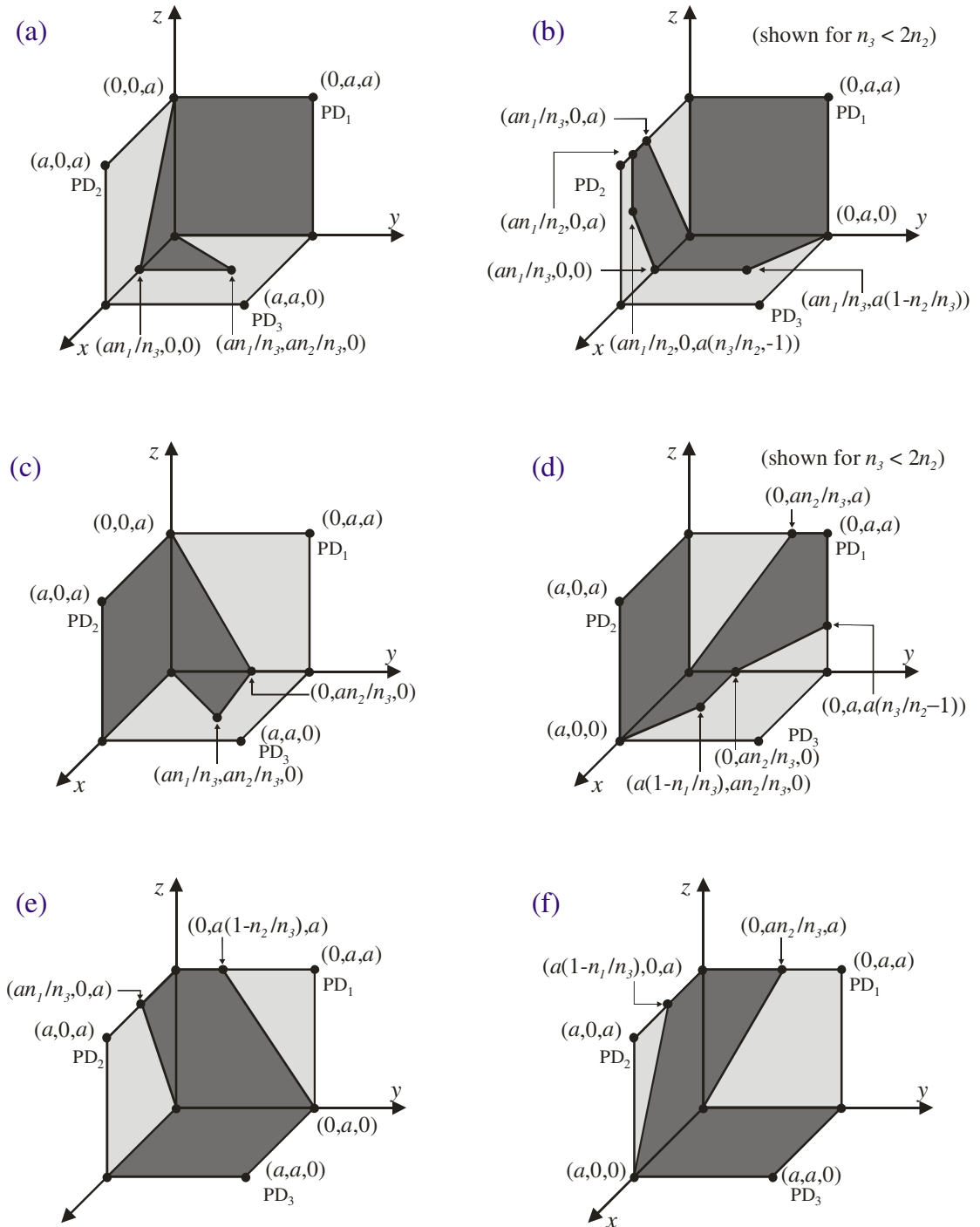


Figure 3.2 Schematics are shown for the internal reflection processes occurring in the retro-detector for directional cosine conditions $n_1 < n_2 < n_3$. Unilluminated areas are shown with light shading. Illuminated areas are shown with dark shading. The order of internal reflections proceeds as (a) PD₁ onto PD₂ onto PD₃, (b) PD₁ onto PD₃ onto PD₂, (c) PD₂ onto PD₁ onto PD₃, (d) PD₂ onto PD₃ onto PD₁, (e) PD₃ onto PD₁ onto PD₂, and (f) PD₃ onto PD₂ onto PD₁.

3.3.2.2. Detected Power Levels for the Second Illumination Case with $n_1 < n_3 < n_2$

The second analysis case corresponds to incident illumination with the x , z , and y directional cosine components in increasing order of magnitudes. This $n_1 < n_3 < n_2$ situation is analyzed for the first subcase, in which the incident light strikes PD₁, reflects onto PD₂, and reflects onto PD₃ (and subsequently exits the retro-detector to return to its source). In this case, the light ray unit-normal vectors that are incident on PD₁, PD₂ and PD₃ are

$$\begin{aligned}\hat{r}_1 &= -n_1\hat{x} - n_2\hat{y} - n_3\hat{z} \\ \hat{r}_{12} &= +n_1\hat{x} - n_2\hat{y} - n_3\hat{z} \\ \hat{r}_{123} &= +n_1\hat{x} + n_2\hat{y} - n_3\hat{z},\end{aligned}\tag{29}$$

respectively, where the subscripts indicate the successive illumination and reflection sequence. Fig. 3.3(a) shows the resulting illumination areas for this subcase. Here, PD₁ is fully illuminated and shaded, and its four corner points in the yz -plane are projected along \hat{r}_{12} onto the xz -plane. The resulting shaded PD₂ illumination area is then defined as the overlap between this projected area and the PD₂ surface. Similarly, the PD₂ illumination area is projected along \hat{r}_{123} onto the xy -plane, and the shaded PD₃ illumination is defined as the overlap between this projected area and the PD₃ surface. The resulting illumination area normal vectors can now be defined for this subcase as

$$\begin{aligned}\bar{A}_1 &= a^2\hat{x} \\ \bar{A}_{12} &= a^2\left(\frac{n_1}{n_2} - \frac{n_1n_3}{2n_2^2}\right)\hat{y} \\ \bar{A}_{123} &= a^2\begin{cases} \left(2\frac{n_1}{n_3} - \frac{n_1}{n_2} - \frac{n_1n_2}{2n_3^2}\right)\hat{z}, n_2 < 2n_3 \\ \frac{n_1}{n_2}\hat{z}, n_2 > 2n_3 \end{cases}.\end{aligned}\tag{30}$$

The corresponding incident power levels associated with PD₁, PD₂ and PD₃ are then found by taking the component of these illumination area normal vectors in (30) along the respective reflected light ray unit-normal vectors in (29). The result is

$$\begin{aligned}P_1 &= -I_0\hat{r}_1 \cdot \bar{A}_1 = I_0a^2n_1, \\ P_{12} &= -RI_0\hat{r}_{12} \cdot \bar{A}_{12} = RI_0a^2\left(n_1 - \frac{n_1n_3}{2n_2}\right)\end{aligned}$$

$$\begin{aligned}
P_{123} &= -R^2 I_0 \hat{r}_{123} \cdot \bar{A}_{123} \\
&= R^2 I_0 a^2 \begin{cases} \left(2n_1 - \frac{n_1 n_3}{n_2} - \frac{n_1 n_2}{2n_3} \right), n_2 < 2n_3. \\ \frac{n_1 n_3}{n_2}, n_2 > 2n_3 \end{cases} \quad (31)
\end{aligned}$$

The second subcase for $n_1 < n_3 < n_2$ corresponds to the situation with the incident light illuminating PD₁, PD₃, and PD₂, in order. In this case, the respective light ray unit-normal vectors incident on the surfaces of PD₁, PD₃ and PD₂ are

$$\begin{aligned}
\hat{r}_1 &= -n_1 \hat{x} - n_2 \hat{y} - n_3 \hat{z} \\
\hat{r}_{13} &= +n_1 \hat{x} - n_2 \hat{y} - n_3 \hat{z} \\
\hat{r}_{132} &= +n_1 \hat{x} - n_2 \hat{y} + n_3 \hat{z}. \quad (32)
\end{aligned}$$

Again, the successive illumination areas are referred onto their adjoining neighbors, and the illumination areas are displayed in Fig. 3.3(b) (shown for $n_2 < 2n_3$). Using the shaded areas on this figure, the illumination area normal vectors can be defined as

$$\begin{aligned}
\bar{A}_1 &= a^2 \hat{x} \\
\bar{A}_{13} &= a^2 \frac{n_1}{2n_2} \hat{z} \\
\bar{A}_{132} &= a^2 \frac{n_1 n_3}{2n_2^2} \hat{y}. \quad (33)
\end{aligned}$$

The corresponding incident power levels associated with PD₁, PD₃ and PD₂ are then found by taking the component of these illumination area normal vectors from (33) along the respective reflected light ray unit-normal vectors from (32). The result is

$$\begin{aligned}
P_1 &= -I_0 \hat{r}_1 \cdot \bar{A}_1 = I_0 a^2 n_1 \\
P_{13} &= -R I_0 \hat{r}_{13} \cdot \bar{A}_{13} = R I_0 a^2 \frac{n_1 n_3}{2n_2} \\
P_{132} &= -R^2 I_0 \hat{r}_{132} \cdot \bar{A}_{132} = R^2 I_0 a^2 \frac{n_1 n_3}{2n_2}. \quad (34)
\end{aligned}$$

The third subcase for $n_1 < n_3 < n_2$ is shown in Fig. 3.3(c), and it is characterized by illumination of PD₂, followed by subsequent reflections off PD₁ and PD₃. The light ray unit-normal vectors incident on the surfaces of PD₂, PD₁, and PD₃, respectively, are

$$\hat{r}_2 = -n_1 \hat{x} - n_2 \hat{y} - n_3 \hat{z}$$

$$\begin{aligned}
\hat{r}_{21} &= -n_1\hat{x} + n_2\hat{y} - n_3\hat{z} \\
\hat{r}_{213} &= +n_1\hat{x} + n_2\hat{y} - n_3\hat{z}.
\end{aligned} \tag{35}$$

Using these light ray components and the resulting illumination area projections, the respective illumination area normal vectors can be written for PD₂, PD₁, and PD₃ as

$$\begin{aligned}
\bar{A}_2 &= a^2\hat{y} \\
\bar{A}_{21} &= a^2\left(1 - \frac{n_3}{2n_2}\right)\hat{x} \\
\bar{A}_{213} &= a^2\frac{n_1}{2n_2}\hat{z}.
\end{aligned} \tag{36}$$

The resulting incident power levels associated with PD₂, PD₁, and PD₃ are then found by taking the component of the illumination area normal vectors from (36) along the respective reflected light ray unit-normal vectors from (35), such that

$$\begin{aligned}
P_2 &= -I_0\hat{r}_2 \cdot \bar{A}_2 = I_0a^2n_2 \\
P_{21} &= -RI_0\hat{r}_{21} \cdot \bar{A}_{21} = RI_0a^2\left(n_1 - \frac{n_1n_3}{2n_2}\right) \\
P_{213} &= -R^2I_0\hat{r}_{213} \cdot \bar{A}_{213} = R^2I_0a^2\frac{n_1n_3}{2n_2}.
\end{aligned} \tag{37}$$

The fourth subcase for $n_1 < n_3 < n_2$ is shown in Fig. 3.3(d), and it corresponds to the case for which PD₂, PD₃, and PD₁ are successively illuminated. The respective light ray unit-normal vectors incident on PD₂, PD₃, and PD₁ can be expressed as

$$\begin{aligned}
\hat{r}_2 &= -n_1\hat{x} - n_2\hat{y} - n_3\hat{z} \\
\hat{r}_{23} &= -n_1\hat{x} + n_2\hat{y} - n_3\hat{z} \\
\hat{r}_{231} &= -n_1\hat{x} + n_2\hat{y} + n_3\hat{z},
\end{aligned} \tag{38}$$

and the PD₂, PD₃, and PD₁ illumination area normal vectors are

$$\begin{aligned}
\bar{A}_2 &= a^2\hat{y}, \\
\bar{A}_{23} &= a^2\left(1 - \frac{n_1}{2n_2}\right)\hat{z} \\
\bar{A}_{231} &= a^2\frac{n_3}{2n_2}\hat{x}.
\end{aligned} \tag{39}$$

The PD_2 , PD_3 , and PD_1 incident powers are then found by taking the illumination area normal vector components in (39) along the reflected light ray unit-normal vectors in (38), giving

$$\begin{aligned}
P_2 &= -I_0 \hat{r}_2 \cdot \bar{A}_2 = I_0 a^2 n_2 \\
P_{23} &= -RI_0 \hat{r}_{23} \cdot \bar{A}_{23} = RI_0 a^2 \left(n_3 - \frac{n_1 n_3}{2n_2} \right) \\
P_{231} &= -R^2 I_0 \hat{r}_{231} \cdot \bar{A}_{231} = R^2 I_0 a^2 \frac{n_1 n_3}{2n_2}.
\end{aligned} \tag{40}$$

The fifth subcase for $n_1 < n_3 < n_2$ has illumination and reflection conditions shown in Fig. 3.3(e). Here, light rays are reflected in order off of PD_3 , PD_1 , and PD_2 . The light ray unit-normal vectors incident on the surfaces of PD_3 , PD_1 , and PD_2 become

$$\begin{aligned}
\hat{r}_3 &= -n_1 \hat{x} - n_2 \hat{y} - n_3 \hat{z} \\
\hat{r}_{31} &= -n_1 \hat{x} - n_2 \hat{y} + n_3 \hat{z} \\
\hat{r}_{312} &= +n_1 \hat{x} - n_2 \hat{y} + n_3 \hat{z},
\end{aligned} \tag{41}$$

and the resulting illumination area normal vectors for illumination of PD_3 , PD_1 , and PD_2 are

$$\begin{aligned}
\bar{A}_3 &= a^2 \hat{z} \\
\bar{A}_{31} &= a^2 \frac{n_3}{2n_2} \hat{x} \\
\bar{A}_{312} &= a^2 \frac{n_1 n_3}{2n_2^2} \hat{y}.
\end{aligned} \tag{42}$$

The resulting incident power levels recorded by PD_3 , PD_1 , and PD_2 for this subcase are then found from (41) and (42) to be

$$\begin{aligned}
P_3 &= -I_0 \hat{r}_3 \cdot \bar{A}_3 = I_0 a^2 n_3 \\
P_{31} &= -RI_0 \hat{r}_{31} \cdot \bar{A}_{31} = RI_0 a^2 \frac{n_1 n_3}{2n_2} \\
P_{312} &= -R^2 I_0 \hat{r}_{312} \cdot \bar{A}_{312} = R^2 I_0 a^2 \frac{n_1 n_3}{2n_2}.
\end{aligned} \tag{43}$$

The sixth and final subcase for $n_1 < n_3 < n_2$ is displayed in Fig. 3.3(f). The surface of PD_3 is illuminated first, followed by successive reflections off of PD_2 and PD_1 . The light ray unit-normal vectors for this succession are

$$\hat{r}_3 = -n_1 \hat{x} - n_2 \hat{y} - n_3 \hat{z}$$

$$\begin{aligned}
\hat{r}_{32} &= -n_1\hat{x} - n_2\hat{y} + n_3\hat{z} \\
\hat{r}_{321} &= -n_1\hat{x} + n_2\hat{y} + n_3\hat{z}.
\end{aligned} \tag{44}$$

The resulting illumination area normal vectors and detected power levels for PD₃, PD₂, and PD₁ are

$$\begin{aligned}
\bar{A}_3 &= a^2\hat{z} \\
\bar{A}_{32} &= a^2\left(\frac{n_3}{n_2} - \frac{n_1n_3}{2n_2^2}\right)\hat{y} \\
\bar{A}_{321} &= a^2\begin{cases} \left(2 - \frac{n_3}{n_2} - \frac{n_2}{2n_3}\right)\hat{x}, n_2 < 2n_3 \\ \frac{n_3}{n_2}\hat{x}, n_2 > 2n_3 \end{cases},
\end{aligned} \tag{45}$$

and

$$\begin{aligned}
P_3 &= -I_0\hat{r}_3 \cdot \bar{A}_3 = I_0a^2n_3 \\
P_{32} &= -RI_0\hat{r}_{32} \cdot \bar{A}_{32} = RI_0a^2\left(n_3 - \frac{n_1n_3}{2n_2}\right) \\
P_{321} &= -R^2I_0\hat{r}_{321} \cdot \bar{A}_{321} \\
&= R^2I_0a^2\begin{cases} \left(2n_1 - \frac{n_1n_3}{n_2} - \frac{n_1n_2}{2n_3}\right), n_2 < 2n_3 \\ \frac{n_1n_3}{n_2}, n_2 > 2n_3 \end{cases}.
\end{aligned} \tag{46}$$

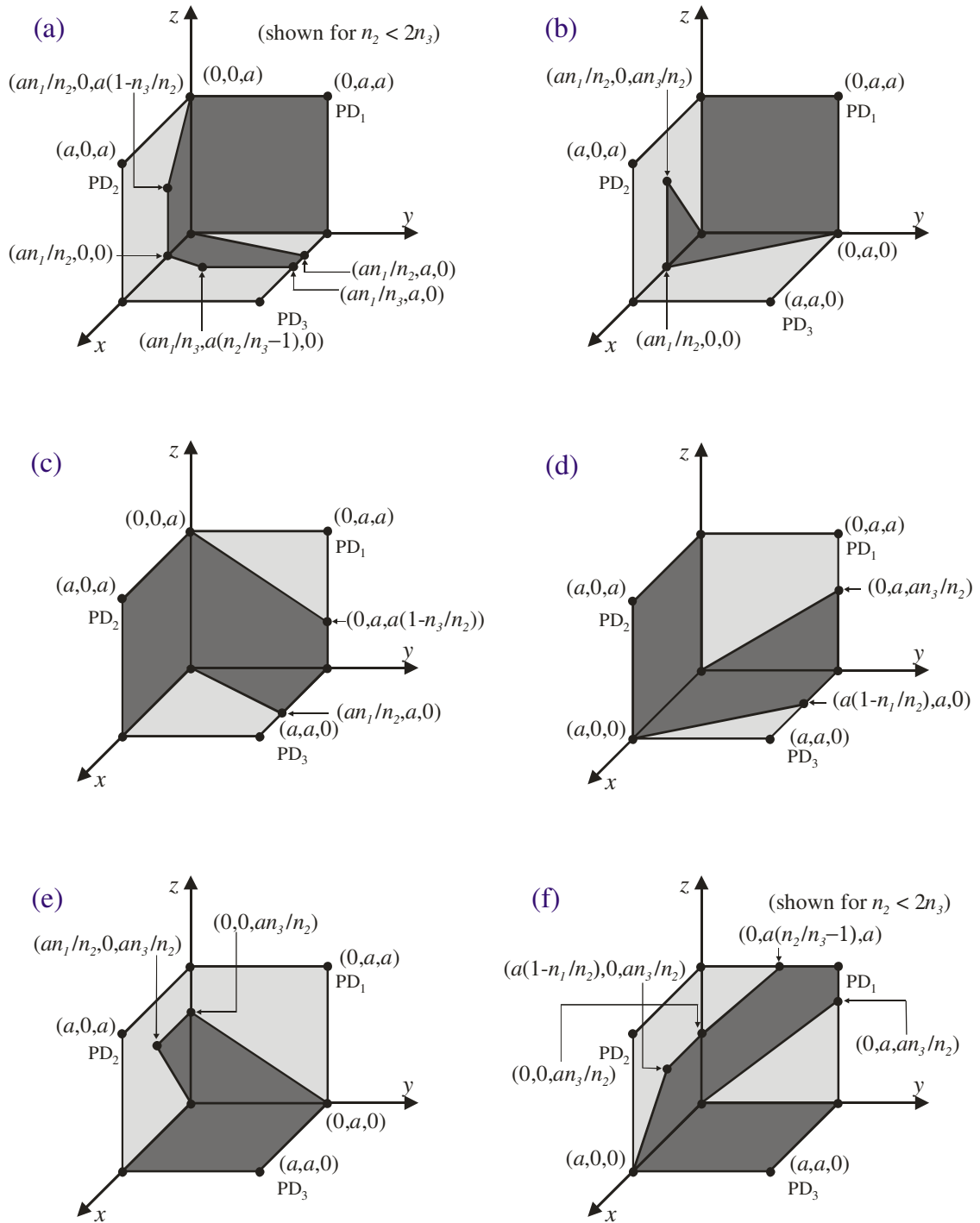


Figure 3.3 Schematics are shown for the internal reflection processes occurring in the retro-detector for directional cosine conditions $n_1 < n_3 < n_2$. Unilluminated areas are shown with light shading. Illuminated areas are shown with dark shading. The order of internal reflections proceeds as (a) PD₁ onto PD₂ onto PD₃, (b) PD₁ onto PD₃ onto PD₂, (c) PD₂ onto PD₁ onto PD₃, (d) PD₂ onto PD₃ onto PD₁, (e) PD₃ onto PD₁ onto PD₂, and (f) PD₃ onto PD₂ onto PD₁.

3.3.2.3. Detected Power Levels for the Third Illumination Case with $n_2 < n_1 < n_3$

The third analysis case corresponds to incident illumination with the y , x , and z directional cosine components in increasing order of magnitudes. This $n_2 < n_1 < n_3$ situation is analyzed for the first subcase, in which the incident light strikes PD₁, reflects onto PD₂, and reflects onto PD₃ (and subsequently exits the retro-detector to return to its source). In this case, the light ray unit-normal vectors that are incident on PD₁, PD₂ and PD₃ are

$$\begin{aligned}\hat{r}_1 &= -n_1\hat{x} - n_2\hat{y} - n_3\hat{z} \\ \hat{r}_{12} &= +n_1\hat{x} - n_2\hat{y} - n_3\hat{z} \\ \hat{r}_{123} &= +n_1\hat{x} + n_2\hat{y} - n_3\hat{z},\end{aligned}\tag{47}$$

respectively, where the subscripts indicate the successive illumination and reflection sequence. Fig. 3.4(a) shows the resulting illumination areas for this subcase. Here, PD₁ is fully illuminated and shaded, and its four corner points in the yz -plane are projected along \hat{r}_{12} onto the xz -plane. The resulting shaded PD₂ illumination area is then defined as the overlap between this projected area and the PD₂ surface. Similarly, the PD₂ illumination area is projected along \hat{r}_{123} onto the xy -plane, and the shaded PD₃ illumination is defined as the overlap between this projected area and the PD₃ surface. The resulting illumination area normal vectors can now be defined for this subcase as

$$\begin{aligned}\bar{A}_1 &= a^2\hat{x}, \\ \bar{A}_{12} &= a^2\frac{n_1}{2n_3}\hat{y} \\ \bar{A}_{123} &= a^2\frac{n_1n_2}{2n_3}\hat{z}.\end{aligned}\tag{48}$$

The corresponding incident power levels associated with PD₁, PD₂ and PD₃ are then found by taking the component of these illumination area normal vectors in (48) along the respective reflected light ray unit-normal vectors in (47). The result is

$$\begin{aligned}P_1 &= -I_0\hat{r}_1 \cdot \bar{A}_1 = I_0a^2n_1 \\ P_{12} &= -RI_0\hat{r}_{12} \cdot \bar{A}_{12} = RI_0a^2\frac{n_1n_2}{2n_3} \\ P_{123} &= -R^2I_0\hat{r}_{123} \cdot \bar{A}_{123} = R^2I_0a^2\frac{n_1n_2}{2n_3}.\end{aligned}\tag{49}$$

The second subcase for $n_2 < n_l < n_3$ corresponds to the situation with the incident light illuminating PD₁, PD₃, and PD₂, in order. In this case, the respective light ray unit-normal vectors incident on the surfaces of PD₁, PD₃ and PD₂ are

$$\begin{aligned}\hat{r}_1 &= -n_1\hat{x} - n_2\hat{y} - n_3\hat{z} \\ \hat{r}_{13} &= +n_1\hat{x} - n_2\hat{y} - n_3\hat{z} \\ \hat{r}_{132} &= +n_1\hat{x} - n_2\hat{y} + n_3\hat{z}.\end{aligned}\quad (50)$$

Again, the successive illumination areas are referred onto their adjoining neighbours, and the illumination areas are displayed in Fig. 3.4(b) (shown for $n_3 < 2n_l$). Using the shaded areas on this figure, the illumination area normal vectors can be defined as

$$\begin{aligned}\bar{A}_1 &= a^2\hat{x} \\ \bar{A}_{13} &= a^2\left(\frac{n_1}{n_3} - \frac{n_1n_2}{2n_3^2}\right)\hat{z} \\ \bar{A}_{132} &= a^2\begin{cases} \left(2 - \frac{n_1}{n_3} - \frac{n_3}{2n_1}\right)\hat{y}, n_3 < 2n_1 \\ \frac{n_1}{n_3}\hat{y}, n_3 > 2n_1 \end{cases}.\end{aligned}\quad (51)$$

The corresponding incident power levels associated with PD₁, PD₃ and PD₂ are then found by taking the component of these illumination area normal vectors from (51) along the respective reflected light ray unit-normal vectors from (50). The result is

$$\begin{aligned}P_1 &= -I_0\hat{r}_1 \cdot \bar{A}_1 = I_0a^2n_1 \\ P_{13} &= -RI_0\hat{r}_{13} \cdot \bar{A}_{13} = RI_0a^2\left(n_1 - \frac{n_1n_2}{2n_3}\right) \\ P_{132} &= -R^2I_0\hat{r}_{132} \cdot \bar{A}_{132} \\ &= R^2I_0a^2\begin{cases} \left(2n_2 - \frac{n_1n_2}{n_3} - \frac{n_2n_3}{2n_1}\right), n_3 < 2n_1 \\ \frac{n_1n_2}{n_3}, n_3 > 2n_1 \end{cases}.\end{aligned}\quad (52)$$

The third subcase for $n_2 < n_l < n_3$ is shown in Fig. 3.4(c), and it is characterized by illumination of PD₂, followed by subsequent reflections off PD₁ and PD₃. The light ray unit-normal vectors incident on the surfaces of PD₂, PD₁, and PD₃, respectively, are

$$\begin{aligned}\hat{r}_2 &= -n_1\hat{x} - n_2\hat{y} - n_3\hat{z} \\ \hat{r}_{21} &= -n_1\hat{x} + n_2\hat{y} - n_3\hat{z}\end{aligned}$$

$$\hat{r}_{213} = +n_1\hat{x} + n_2\hat{y} - n_3\hat{z}. \quad (53)$$

Using these light ray components and the resulting illumination area projections, the respective illumination area normal vectors can be written for PD₂, PD₁, and PD₃ as

$$\begin{aligned} \bar{A}_2 &= a^2\hat{y} \\ \bar{A}_{21} &= a^2\frac{n_2}{2n_3}\hat{x} \\ \bar{A}_{213} &= a^2\frac{n_1n_2}{2n_3}\hat{z}. \end{aligned} \quad (54)$$

The resulting incident power levels associated with PD₂, PD₁, and PD₃ are then found by taking the component of the illumination area normal vectors from (54) along the respective reflected light ray unit-normal vectors from (53), such that

$$\begin{aligned} P_2 &= -I_0\hat{r}_2 \cdot \bar{A}_2 = I_0a^2n_2 \\ P_{21} &= -RI_0\hat{r}_{21} \cdot \bar{A}_{21} = RI_0a^2\frac{n_1n_2}{2n_3} \\ P_{213} &= -R^2I_0\hat{r}_{213} \cdot \bar{A}_{213} = R^2I_0a^2\frac{n_1n_2}{2n_3}. \end{aligned} \quad (55)$$

The fourth subcase for $n_2 < n_1 < n_3$ is shown in Fig. 3.4(d), and it corresponds to the case for which PD₂, PD₃, and PD₁ are successively illuminated. The respective light ray unit-normal vectors incident on PD₂, PD₃, and PD₁ can be expressed as

$$\begin{aligned} \hat{r}_2 &= -n_1\hat{x} - n_2\hat{y} - n_3\hat{z} \\ \hat{r}_{23} &= -n_1\hat{x} + n_2\hat{y} - n_3\hat{z} \\ \hat{r}_{231} &= -n_1\hat{x} + n_2\hat{y} + n_3\hat{z}, \end{aligned} \quad (56)$$

and the PD₂, PD₃, and PD₁ illumination area normal vectors are

$$\begin{aligned} \bar{A}_2 &= a^2\hat{y} \\ \bar{A}_{23} &= a^2\left(\frac{n_2}{n_3} - \frac{n_1n_2}{2n_3^2}\right)\hat{z} \\ \bar{A}_{231} &= a^2\begin{cases} \left(2\frac{n_2}{n_1} - \frac{n_2}{n_3} - \frac{n_2n_3}{2n_1^2}\right)\hat{x}, n_3 < 2n_1 \\ \frac{n_2}{n_3}\hat{x}, n_3 > 2n_1 \end{cases}. \end{aligned} \quad (57)$$

The PD_2 , PD_3 , and PD_1 incident powers are then found by taking the illumination area normal vector components in (57) along the reflected light ray unit-normal vectors in (56), giving

$$\begin{aligned}
P_2 &= -I_0 \hat{r}_2 \cdot \bar{A}_2 = I_0 a^2 n_2 \\
P_{23} &= -RI_0 \hat{r}_{23} \cdot \bar{A}_{23} = RI_0 a^2 \left(n_2 - \frac{n_1 n_2}{2n_3} \right) \\
P_{231} &= -R^2 I_0 \hat{r}_{231} \cdot \bar{A}_{231} \\
&= R^2 I_0 a^2 \begin{cases} \left(2n_2 - \frac{n_1 n_2}{n_3} - \frac{n_2 n_3}{2n_1} \right), n_3 < 2n_1 \\ \frac{n_1 n_2}{n_3}, n_3 > 2n_1 \end{cases}. \tag{58}
\end{aligned}$$

The fifth subcase for $n_2 < n_1 < n_3$ has illumination and reflection conditions shown in Fig. 3.4(e). Here, light rays are reflected in order off of PD_3 , PD_1 , and PD_2 . The light ray unit-normal vectors incident on the surfaces of PD_3 , PD_1 , and PD_2 become

$$\begin{aligned}
\hat{r}_3 &= -n_1 \hat{x} - n_2 \hat{y} - n_3 \hat{z} \\
\hat{r}_{31} &= -n_1 \hat{x} - n_2 \hat{y} + n_3 \hat{z} \\
\hat{r}_{312} &= +n_1 \hat{x} - n_2 \hat{y} + n_3 \hat{z}, \tag{59}
\end{aligned}$$

and the resulting illumination area normal vectors for illumination of PD_3 , PD_1 , and PD_2 are

$$\begin{aligned}
\bar{A}_3 &= a^2 \hat{z} \\
\bar{A}_{31} &= a^2 \left(1 - \frac{n_2}{2n_3} \right) \hat{x} \\
\bar{A}_{312} &= a^2 \frac{n_1}{2n_3} \hat{y}. \tag{60}
\end{aligned}$$

The resulting incident power levels recorded by PD_3 , PD_1 , and PD_2 for this subcase are then found from (59) and (60) to be

$$\begin{aligned}
P_3 &= -I_0 \hat{r}_3 \cdot \bar{A}_3 = I_0 a^2 n_3 \\
P_{31} &= -RI_0 \hat{r}_{31} \cdot \bar{A}_{31} = RI_0 a^2 \left(n_1 - \frac{n_1 n_2}{2n_3} \right) \\
P_{312} &= -R^2 I_0 \hat{r}_{312} \cdot \bar{A}_{312} = R^2 I_0 a^2 \frac{n_1 n_2}{2n_3}. \tag{61}
\end{aligned}$$

The sixth and final subcase for $n_2 < n_1 < n_3$ is displayed in Fig. 3.4(f). The surface of PD₃ is illuminated first, followed by successive reflections off of PD₂ and PD₁. The light ray unit-normal vectors for this succession are

$$\begin{aligned}\hat{r}_3 &= -n_1\hat{x} - n_2\hat{y} - n_3\hat{z} \\ \hat{r}_{32} &= -n_1\hat{x} - n_2\hat{y} + n_3\hat{z} \\ \hat{r}_{321} &= -n_1\hat{x} + n_2\hat{y} + n_3\hat{z}.\end{aligned}\tag{62}$$

The resulting illumination area normal vectors and detected power levels for PD₃, PD₂, and PD₁ are

$$\begin{aligned}\bar{A}_3 &= a^2\hat{z} \\ \bar{A}_{32} &= a^2\left(1 - \frac{n_1}{2n_3}\right)\hat{y} \\ \bar{A}_{321} &= a^2\frac{n_2}{2n_3}\hat{x}.\end{aligned}\tag{63}$$

and

$$\begin{aligned}P_3 &= -I_0\hat{r}_3 \cdot \bar{A}_3 = I_0a^2n_3 \\ P_{32} &= -RI_0\hat{r}_{32} \cdot \bar{A}_{32} = RI_0a^2\left(n_2 - \frac{n_1n_2}{2n_3}\right) \\ P_{321} &= -R^2I_0\hat{r}_{321} \cdot \bar{A}_{321} = R^2I_0a^2\frac{n_1n_2}{2n_3}.\end{aligned}\tag{64}$$

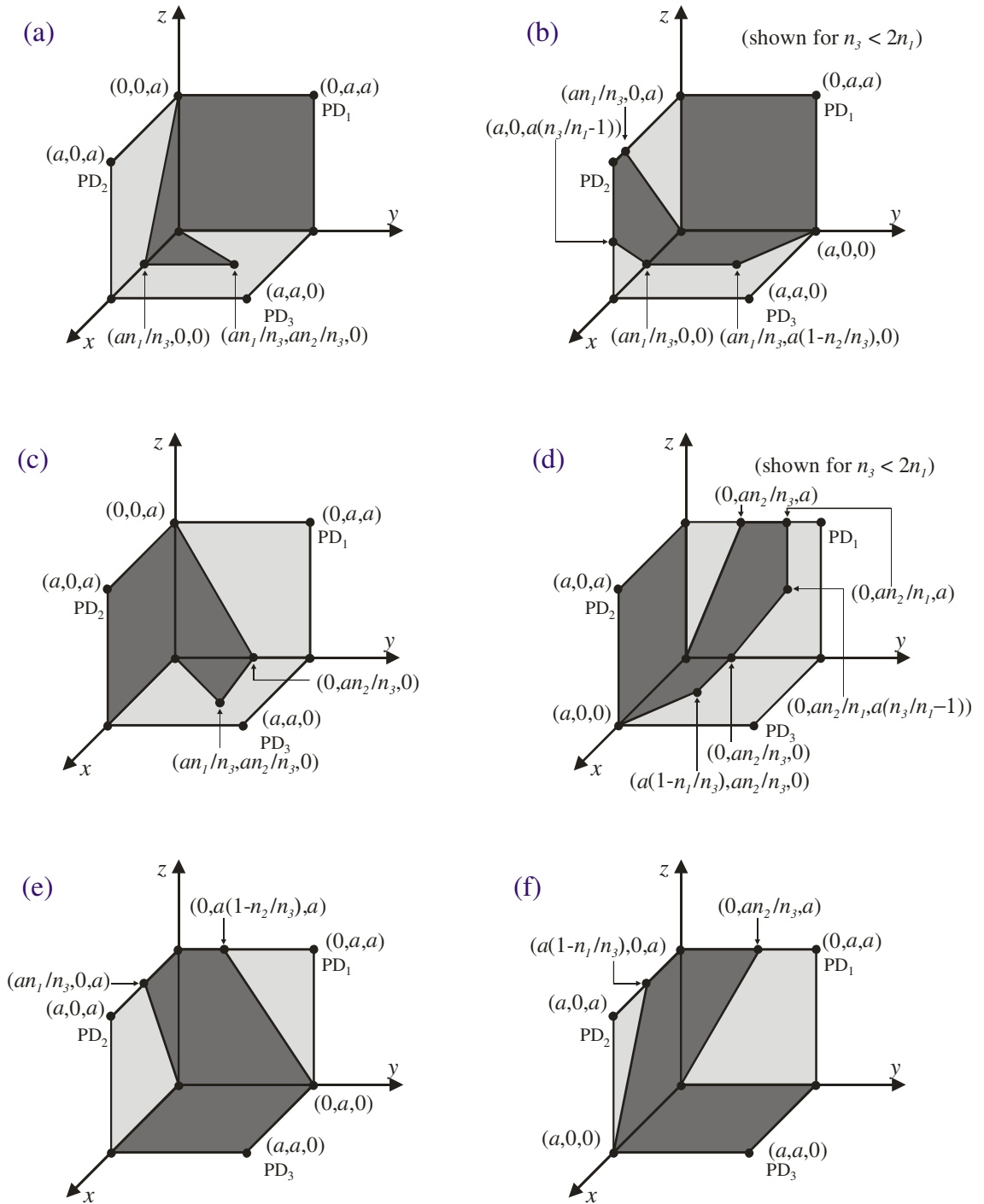


Figure 3.4 Schematics are shown for the internal reflection processes occurring in the retro-detector for directional cosine conditions $n_2 < n_1 < n_3$. Unilluminated areas are shown with light shading. Illuminated areas are shown with dark shading. The order of internal reflections proceeds as (a) PD₁ onto PD₂ onto PD₃, (b) PD₁ onto PD₃ onto PD₂, (c) PD₂ onto PD₁ onto PD₃, (d) PD₂ onto PD₃ onto PD₁, (e) PD₃ onto PD₁ onto PD₂, and (f) PD₃ onto PD₂ onto PD₁.

3.3.2.4. Detected Power Levels for the Fourth Illumination Case with $n_2 < n_3 < n_1$

The fourth analysis case corresponds to incident illumination with the y , z , and x directional cosine components in increasing order of magnitudes. This $n_2 < n_3 < n_1$ situation is analyzed for the first subcase, in which the incident light strikes PD₁, reflects onto PD₂, and reflects onto PD₃ (and subsequently exits the retro-detector to return to its source). In this case, the light ray unit-normal vectors that are incident on PD₁, PD₂ and PD₃ are

$$\begin{aligned}\hat{r}_1 &= -n_1\hat{x} - n_2\hat{y} - n_3\hat{z} \\ \hat{r}_{12} &= +n_1\hat{x} - n_2\hat{y} - n_3\hat{z} \\ \hat{r}_{123} &= +n_1\hat{x} + n_2\hat{y} - n_3\hat{z},\end{aligned}\tag{65}$$

respectively, where the subscripts indicate the successive illumination and reflection sequence. Fig. 3.5(a) shows the resulting illumination areas for this subcase. Here, PD₁ is fully illuminated and shaded, and its four corner points in the yz -plane are projected along \hat{r}_{12} onto the xz -plane. The resulting shaded PD₂ illumination area is then defined as the overlap between this projected area and the PD₂ surface. Similarly, the PD₂ illumination area is projected along \hat{r}_{123} onto the xy -plane, and the shaded PD₃ illumination is defined as the overlap between this projected area and the PD₃ surface. The resulting illumination area normal vectors can now be defined for this subcase as

$$\begin{aligned}\bar{A}_1 &= a^2\hat{x} \\ \bar{A}_{12} &= a^2\left(1 - \frac{n_3}{2n_1}\right)\hat{y} \\ \bar{A}_{123} &= a^2\frac{n_2}{2n_1}\hat{z}.\end{aligned}\tag{66}$$

The corresponding incident power levels associated with PD₁, PD₂ and PD₃ are then found by taking the component of these illumination area normal vectors in (66) along the respective reflected light ray unit-normal vectors in (65). The result is

$$\begin{aligned}P_1 &= -I_0\hat{r}_1 \cdot \bar{A}_1 = I_0a^2n_1 \\ P_{12} &= -RI_0\hat{r}_{12} \cdot \bar{A}_{12} = RI_0a^2\left(n_2 - \frac{n_2n_3}{2n_1}\right) \\ P_{123} &= -R^2I_0\hat{r}_{123} \cdot \bar{A}_{123} = R^2I_0a^2\frac{n_2n_3}{2n_1}.\end{aligned}\tag{67}$$

The second subcase for $n_2 < n_3 < n_1$ corresponds to the situation with the incident light illuminating PD₁, PD₃, and PD₂, in order. In this case, the respective light ray unit-normal vectors incident on the surfaces of PD₁, PD₃ and PD₂ are

$$\begin{aligned}\hat{r}_1 &= -n_1\hat{x} - n_2\hat{y} - n_3\hat{z} \\ \hat{r}_{13} &= +n_1\hat{x} - n_2\hat{y} - n_3\hat{z} \\ \hat{r}_{132} &= +n_1\hat{x} - n_2\hat{y} + n_3\hat{z}.\end{aligned}\quad (68)$$

Again, the successive illumination areas are referred onto their adjoining neighbors, and the illumination areas are displayed in Fig. 3.5(b) (shown for $n_1 < 2n_3$). Using the shaded areas on this figure, the illumination area normal vectors can be defined as

$$\begin{aligned}\bar{A}_1 &= a^2\hat{x} \\ \bar{A}_{13} &= a^2\left(1 - \frac{n_2}{2n_1}\right)\hat{z} \\ \bar{A}_{132} &= a^2\frac{n_3}{2n_1}\hat{y}.\end{aligned}\quad (69)$$

The corresponding incident power levels associated with PD₁, PD₃ and PD₂ are then found by taking the component of these illumination area normal vectors from (69) along the respective reflected light ray unit-normal vectors from (68). The result is

$$\begin{aligned}P_1 &= -I_0\hat{r}_1 \cdot \bar{A}_1 = I_0a^2n_1 \\ P_{13} &= -RI_0\hat{r}_{13} \cdot \bar{A}_{13} = RI_0a^2\left(n_3 - \frac{n_2n_3}{2n_1}\right) \\ P_{132} &= -R^2I_0\hat{r}_{132} \cdot \bar{A}_{132} = R^2I_0a^2\frac{n_2n_3}{2n_1}.\end{aligned}\quad (70)$$

The third subcase for $n_2 < n_3 < n_1$ is shown in Fig. 3.5(c), and it is characterized by illumination of PD₂, followed by subsequent reflections off PD₁ and PD₃. The light ray unit-normal vectors incident on the surfaces of PD₂, PD₁, and PD₃, respectively, are

$$\begin{aligned}\hat{r}_2 &= -n_1\hat{x} - n_2\hat{y} - n_3\hat{z} \\ \hat{r}_{21} &= -n_1\hat{x} + n_2\hat{y} - n_3\hat{z} \\ \hat{r}_{213} &= +n_1\hat{x} + n_2\hat{y} - n_3\hat{z}.\end{aligned}\quad (71)$$

Using these light ray components and the resulting illumination area projections, the respective illumination area normal vectors can be written for PD₂, PD₁, and PD₃ as

$$\begin{aligned}
\bar{A}_2 &= a^2 \hat{y} \\
\bar{A}_{21} &= a^2 \left(\frac{n_2}{n_1} - \frac{n_2 n_3}{2n_1^2} \right) \hat{x} \\
\bar{A}_{213} &= a^2 \begin{cases} \left(2 \frac{n_2}{n_3} - \frac{n_2}{n_1} - \frac{n_1 n_2}{2n_3^2} \right) \hat{z}, n_1 < 2n_3 \\ \frac{n_2}{n_1} \hat{z}, n_1 > 2n_3 \end{cases}.
\end{aligned} \tag{72}$$

The resulting incident power levels associated with PD₂, PD₁, and PD₃ are then found by taking the component of the illumination area normal vectors from (72) along the respective reflected light ray unit-normal vectors from (71), such that

$$\begin{aligned}
P_2 &= -I_0 \hat{r}_2 \cdot \bar{A}_2 = I_0 a^2 n_2 \\
P_{21} &= -RI_0 \hat{r}_{21} \cdot \bar{A}_{21} = RI_0 a^2 \left(n_2 - \frac{n_2 n_3}{2n_1} \right) \\
P_{213} &= -R^2 I_0 \hat{r}_{213} \cdot \bar{A}_{213} \\
&= R^2 I_0 a^2 \begin{cases} \left(2n_2 - \frac{n_2 n_3}{n_1} - \frac{n_1 n_2}{2n_3} \right), n_1 < 2n_3 \\ \frac{n_2 n_3}{n_1}, n_1 > 2n_3 \end{cases}.
\end{aligned} \tag{73}$$

The fourth subcase for $n_2 < n_3 < n_1$ is shown in Fig. 3.5(d), and it corresponds to the case for which PD₂, PD₃, and PD₁ are successively illuminated. The respective light ray unit-normal vectors incident on PD₂, PD₃, and PD₁ can be expressed as

$$\begin{aligned}
\hat{r}_2 &= -n_1 \hat{x} - n_2 \hat{y} - n_3 \hat{z} \\
\hat{r}_{23} &= -n_1 \hat{x} + n_2 \hat{y} - n_3 \hat{z} \\
\hat{r}_{231} &= -n_1 \hat{x} + n_2 \hat{y} + n_3 \hat{z},
\end{aligned} \tag{74}$$

and the PD₂, PD₃, and PD₁ illumination area normal vectors are

$$\begin{aligned}
\bar{A}_2 &= a^2 \hat{y} \\
\bar{A}_{23} &= a^2 \frac{n_2}{2n_1} \hat{z} \\
\bar{A}_{231} &= a^2 \frac{n_2 n_3}{2n_1^2} \hat{x}.
\end{aligned} \tag{75}$$

The PD₂, PD₃, and PD₁ incident powers are then found by taking the illumination area normal vector components in (75) along the reflected light ray unit-normal vectors in (74), giving

$$\begin{aligned}
P_2 &= -I_0 \hat{r}_2 \cdot \bar{A}_2 = I_0 a^2 n_2 \\
P_{23} &= -RI_0 \hat{r}_{23} \cdot \bar{A}_{23} = RI_0 a^2 \frac{n_2 n_3}{2n_1} \\
P_{231} &= -R^2 I_0 \hat{r}_{231} \cdot \bar{A}_{231} = R^2 I_0 a^2 \frac{n_2 n_3}{2n_1}.
\end{aligned} \tag{76}$$

The fifth subcase for $n_2 < n_3 < n_1$ has illumination and reflection conditions shown in Fig. 3.5(e). Here, light rays are reflected in order off of PD₃, PD₁, and PD₂. The light ray unit-normal vectors incident on the surfaces of PD₃, PD₁, and PD₂ become

$$\begin{aligned}
\hat{r}_3 &= -n_1 \hat{x} - n_2 \hat{y} - n_3 \hat{z} \\
\hat{r}_{31} &= -n_1 \hat{x} - n_2 \hat{y} + n_3 \hat{z} \\
\hat{r}_{312} &= +n_1 \hat{x} - n_2 \hat{y} + n_3 \hat{z},
\end{aligned} \tag{77}$$

and the resulting illumination area normal vectors for illumination of PD₃, PD₁, and PD₂ are

$$\begin{aligned}
\bar{A}_3 &= a^2 \hat{z} \\
\bar{A}_{31} &= a^2 \left(\frac{n_3}{n_1} - \frac{n_2 n_3}{2n_1^2} \right) \hat{x} \\
\bar{A}_{312} &= a^2 \begin{cases} \left(2 - \frac{n_3}{n_1} - \frac{n_1}{2n_3} \right) \hat{y}, n_1 < 2n_3 \\ \frac{n_3}{n_1} \hat{y}, n_1 > 2n_3 \end{cases}.
\end{aligned} \tag{78}$$

The resulting incident power levels recorded by PD₃, PD₁, and PD₂ for this subcase are then found from (77) and (78) to be

$$\begin{aligned}
P_3 &= -I_0 \hat{r}_3 \cdot \bar{A}_3 = I_0 a^2 n_3 \\
P_{31} &= -RI_0 \hat{r}_{31} \cdot \bar{A}_{31} = RI_0 a^2 \left(n_3 - \frac{n_2 n_3}{2n_1} \right) \\
P_{312} &= -R^2 I_0 \hat{r}_{312} \cdot \bar{A}_{312} \\
&= R^2 I_0 a^2 \begin{cases} \left(2n_2 - \frac{n_2 n_3}{n_1} - \frac{n_1 n_2}{2n_3} \right), n_1 < 2n_3. \\ \frac{n_2 n_3}{n_1}, n_1 > 2n_3 \end{cases}.
\end{aligned} \tag{79}$$

The sixth and final subcase for $n_2 < n_3 < n_1$ is displayed in Fig. 3.5(f). The surface of PD₃ is illuminated first, followed by successive reflections off of PD₂ and PD₁. The light ray unit-normal vectors for this succession are

$$\begin{aligned}\hat{r}_3 &= -n_1\hat{x} - n_2\hat{y} - n_3\hat{z} \\ \hat{r}_{32} &= -n_1\hat{x} - n_2\hat{y} + n_3\hat{z} \\ \hat{r}_{321} &= -n_1\hat{x} + n_2\hat{y} + n_3\hat{z}.\end{aligned}\tag{80}$$

The resulting illumination area normal vectors and detected power levels for PD₃, PD₂, and PD₁ are

$$\begin{aligned}\bar{A}_3 &= a^2\hat{z} \\ \bar{A}_{32} &= a^2\frac{n_3}{2n_1}\hat{y} \\ \bar{A}_{321} &= a^2\frac{n_2n_3}{2n_1^2}\hat{x},\end{aligned}\tag{81}$$

and

$$\begin{aligned}P_3 &= -I_0\hat{r}_3 \cdot \bar{A}_3 = I_0a^2n_3 \\ P_{32} &= -RI_0\hat{r}_{32} \cdot \bar{A}_{32} = RI_0a^2\frac{n_2n_3}{2n_1} \\ P_{321} &= -R^2I_0\hat{r}_{321} \cdot \bar{A}_{321} = R^2I_0a^2\frac{n_2n_3}{2n_1}.\end{aligned}\tag{82}$$

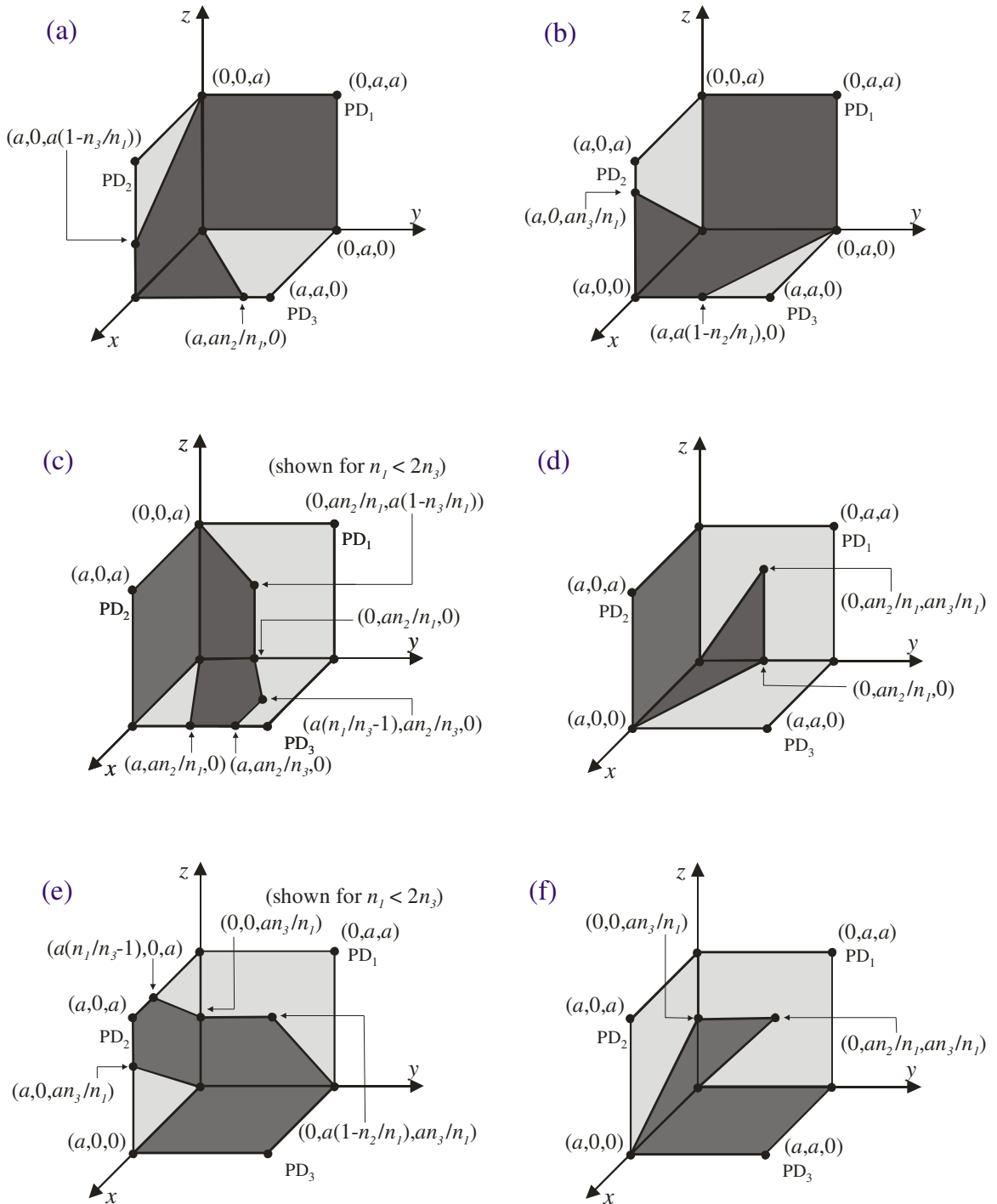


Figure 3.5 Schematics are shown for the internal reflection processes occurring in the retro-detector for directional cosine conditions $n_2 < n_3 < n_1$. Unilluminated areas are shown with light shading. Illuminated areas are shown with dark shading. The order of internal reflections proceeds as (a) PD_1 onto PD_2 onto PD_3 , (b) PD_1 onto PD_3 onto PD_2 , (c) PD_2 onto PD_1 onto PD_3 , (d) PD_2 onto PD_3 onto PD_1 , (e) PD_3 onto PD_1 onto PD_2 , and (f) PD_3 onto PD_2 onto PD_1 .

3.3.2.5. Detected Power Levels for the Fifth Illumination Case with $n_3 < n_1 < n_2$

The fifth analysis case corresponds to incident illumination with the z , x , and y directional cosine components in increasing order of magnitudes. This $n_3 < n_1 < n_2$ situation is analyzed for the first subcase, in which the incident light strikes PD₁, reflects onto PD₂, and reflects onto PD₃ (and subsequently exits the retro-detector to return to its source). In this case, the light ray unit-normal vectors that are incident on PD₁, PD₂ and PD₃ are

$$\begin{aligned}\hat{r}_1 &= -n_1\hat{x} - n_2\hat{y} - n_3\hat{z} \\ \hat{r}_{12} &= +n_1\hat{x} - n_2\hat{y} - n_3\hat{z} \\ \hat{r}_{123} &= +n_1\hat{x} + n_2\hat{y} - n_3\hat{z}.\end{aligned}\quad (83)$$

respectively, where the subscripts indicate the successive illumination and reflection sequence. Fig. 3.6(a) shows the resulting illumination areas for this subcase. Here, PD₁ is fully illuminated and shaded, and its four corner points in the yz -plane are projected along \hat{r}_{12} onto the xz -plane. The resulting shaded PD₂ illumination area is then defined as the overlap between this projected area and the PD₂ surface. Similarly, the PD₂ illumination area is projected along \hat{r}_{123} onto the xy -plane, and the shaded PD₃ illumination is defined as the overlap between this projected area and the PD₃ surface. The resulting illumination area normal vectors can now be defined for this subcase as

$$\begin{aligned}\bar{A}_1 &= a^2\hat{x} \\ \bar{A}_{12} &= a^2\left(\frac{n_1}{n_2} - \frac{n_1n_3}{2n_2^2}\right)\hat{y} \\ \bar{A}_{123} &= a^2\begin{cases} \left(2 - \frac{n_1}{n_2} - \frac{n_2}{2n_1}\right)\hat{z}, n_2 < 2n_1 \\ \frac{n_1}{n_2}\hat{z}, n_2 > 2n_1 \end{cases}.\end{aligned}\quad (84)$$

The corresponding incident power levels associated with PD₁, PD₂ and PD₃ are then found by taking the component of these illumination area normal vectors in (84) along the respective reflected light ray unit-normal vectors in (83). The result is

$$\begin{aligned}P_1 &= -I_0\hat{r}_1 \cdot \bar{A}_1 = I_0a^2n_1 \\ P_{12} &= -RI_0\hat{r}_{12} \cdot \bar{A}_{12} = RI_0a^2\left(n_1 - n_1\frac{n_3}{2n_2}\right)\end{aligned}$$

$$\begin{aligned}
P_{123} &= -R^2 I_0 \hat{r}_{123} \cdot \bar{A}_{123} \\
&= R^2 I_0 a^2 \begin{cases} \left(2n_3 - \frac{n_1 n_3}{n_2} - \frac{n_2 n_3}{2n_1} \right), n_2 < 2n_1 . \\ \frac{n_1 n_3}{n_2}, n_2 > 2n_1 \end{cases} .
\end{aligned} \tag{85}$$

The second subcase for $n_3 < n_1 < n_2$ corresponds to the situation with the incident light illuminating PD₁, PD₃, and PD₂, in order. In this case, the respective light ray unit-normal vectors incident on the surfaces of PD₁, PD₃ and PD₂ are

$$\begin{aligned}
\hat{r}_1 &= -n_1 \hat{x} - n_2 \hat{y} - n_3 \hat{z} \\
\hat{r}_{13} &= +n_1 \hat{x} - n_2 \hat{y} - n_3 \hat{z} \\
\hat{r}_{132} &= +n_1 \hat{x} - n_2 \hat{y} + n_3 \hat{z} .
\end{aligned} \tag{86}$$

Again, the successive illumination areas are referred onto their adjoining neighbours, and the illumination areas are displayed in Fig. 3.6(b) (shown for $n_2 < 2n_1$). Using the shaded areas on this figure, the illumination area normal vectors can be defined as

$$\begin{aligned}
\bar{A}_1 &= a^2 \hat{x} \\
\bar{A}_{13} &= a^2 \frac{n_1}{2n_2} \hat{z} \\
\bar{A}_{132} &= a^2 \frac{n_1 n_3}{2n_2^2} \hat{y} .
\end{aligned} \tag{87}$$

The corresponding incident power levels associated with PD₁, PD₃ and PD₂ are then found by taking the component of these illumination area normal vectors from (87) along the respective reflected light ray unit-normal vectors from (86). The result is

$$\begin{aligned}
P_1 &= -I_0 \hat{r}_1 \cdot \bar{A}_1 = I_0 a^2 n_1 \\
P_{13} &= -R I_0 \hat{r}_{13} \cdot \bar{A}_{13} = R I_0 a^2 \frac{n_1 n_3}{2n_2} \\
P_{132} &= -R^2 I_0 \hat{r}_{132} \cdot \bar{A}_{132} = R^2 I_0 a^2 \frac{n_1 n_3}{2n_2} .
\end{aligned} \tag{88}$$

The third subcase for $n_3 < n_1 < n_2$ is shown in Fig. 3.6(c), and it is characterized by illumination of PD₂, followed by subsequent reflections off PD₁ and PD₃. The light ray unit-normal vectors incident on the surfaces of PD₂, PD₁, and PD₃, respectively, are

$$\hat{r}_2 = -n_1 \hat{x} - n_2 \hat{y} - n_3 \hat{z}$$

$$\begin{aligned}
\hat{r}_{21} &= -n_1\hat{x} + n_2\hat{y} - n_3\hat{z} \\
\hat{r}_{213} &= +n_1\hat{x} + n_2\hat{y} - n_3\hat{z}.
\end{aligned} \tag{89}$$

Using these light ray components and the resulting illumination area projections, the respective illumination area normal vectors can be written for PD₂, PD₁, and PD₃ as

$$\begin{aligned}
\bar{A}_2 &= a^2\hat{y} \\
\bar{A}_{21} &= a^2\left(1 - \frac{n_3}{2n_2}\right)\hat{x} \\
\bar{A}_{213} &= a^2\frac{n_1}{2n_2}\hat{z}.
\end{aligned} \tag{90}$$

The resulting incident power levels associated with PD₂, PD₁, and PD₃ are then found by taking the component of the illumination area normal vectors from (90) along the respective reflected light ray unit-normal vectors from (89), such that

$$\begin{aligned}
P_2 &= -I_0\hat{r}_2 \cdot \bar{A}_2 = I_0a^2n_2 \\
P_{21} &= -RI_0\hat{r}_{21} \cdot \bar{A}_{21} = RI_0a^2\left(n_1 - \frac{n_1n_3}{2n_2}\right) \\
P_{213} &= -R^2I_0\hat{r}_{213} \cdot \bar{A}_{213} = R^2I_0a^2\frac{n_1n_3}{2n_2}.
\end{aligned} \tag{91}$$

The fourth subcase for $n_3 < n_1 < n_2$ is shown in Fig. 3.6(d), and it corresponds to the case for which PD₂, PD₃, and PD₁ are successively illuminated. The respective light ray unit-normal vectors incident on PD₂, PD₃, and PD₁ can be expressed as

$$\begin{aligned}
\hat{r}_2 &= -n_1\hat{x} - n_2\hat{y} - n_3\hat{z} \\
\hat{r}_{23} &= -n_1\hat{x} + n_2\hat{y} - n_3\hat{z} \\
\hat{r}_{231} &= -n_1\hat{x} + n_2\hat{y} + n_3\hat{z},
\end{aligned} \tag{92}$$

and the PD₂, PD₃, and PD₁ illumination area normal vectors are

$$\begin{aligned}
\bar{A}_2 &= a^2\hat{y} \\
\bar{A}_{23} &= a^2\left(1 - \frac{n_1}{2n_2}\right)\hat{z} \\
\bar{A}_{231} &= a^2\frac{n_3}{2n_2}\hat{x}.
\end{aligned} \tag{93}$$

The PD_2 , PD_3 , and PD_1 incident powers are then found by taking the illumination area normal vector components in (93) along the reflected light ray unit-normal vectors in (92), giving

$$\begin{aligned}
P_2 &= -I_0 \hat{r}_2 \cdot \bar{A}_2 = I_0 a^2 n_2 \\
P_{23} &= -RI_0 \hat{r}_{23} \cdot \bar{A}_{23} = RI_0 a^2 \left(n_3 - \frac{n_1 n_3}{2n_2} \right) \\
P_{231} &= -R^2 I_0 \hat{r}_{231} \cdot \bar{A}_{231} = R^2 I_0 a^2 \frac{n_1 n_3}{2n_2}.
\end{aligned} \tag{94}$$

The fifth subcase for $n_3 < n_1 < n_2$ has illumination and reflection conditions shown in Fig. 3.6(e). Here, light rays are reflected in order off of PD_3 , PD_1 , and PD_2 . The light ray unit-normal vectors incident on the surfaces of PD_3 , PD_1 , and PD_2 become

$$\begin{aligned}
\hat{r}_3 &= -n_1 \hat{x} - n_2 \hat{y} - n_3 \hat{z} \\
\hat{r}_{31} &= -n_1 \hat{x} - n_2 \hat{y} + n_3 \hat{z} \\
\hat{r}_{312} &= +n_1 \hat{x} - n_2 \hat{y} + n_3 \hat{z},
\end{aligned} \tag{95}$$

and the resulting illumination area normal vectors for illumination of PD_3 , PD_1 , and PD_2 are

$$\begin{aligned}
\bar{A}_3 &= a^2 \hat{z} \\
\bar{A}_{31} &= a^2 \frac{n_3}{2n_2} \hat{x} \\
\bar{A}_{312} &= a^2 \frac{n_1 n_3}{2n_2^2} \hat{y}.
\end{aligned} \tag{96}$$

The resulting incident power levels recorded by PD_3 , PD_1 , and PD_2 for this subcase are then found from (95) and (96) to be

$$\begin{aligned}
P_3 &= -I_0 \hat{r}_3 \cdot \bar{A}_3 = I_0 a^2 n_3 \\
P_{31} &= -RI_0 \hat{r}_{31} \cdot \bar{A}_{31} = RI_0 a^2 \frac{n_1 n_3}{2n_2} \\
P_{312} &= -R^2 I_0 \hat{r}_{312} \cdot \bar{A}_{312} = R^2 I_0 a^2 \frac{n_1 n_3}{2n_2}.
\end{aligned} \tag{97}$$

The sixth and final subcase for $n_3 < n_1 < n_2$ is displayed in Fig. 3.6(f). The surface of PD_3 is illuminated first, followed by successive reflections off of PD_2 and PD_1 . The light ray unit-normal vectors for this succession are

$$\hat{r}_3 = -n_1 \hat{x} - n_2 \hat{y} - n_3 \hat{z}$$

$$\begin{aligned}
\hat{r}_{32} &= -n_1\hat{x} - n_2\hat{y} + n_3\hat{z} \\
\hat{r}_{321} &= -n_1\hat{x} + n_2\hat{y} + n_3\hat{z}.
\end{aligned} \tag{98}$$

The resulting illumination area normal vectors and detected power levels for PD₃, PD₂, and PD₁ are

$$\begin{aligned}
\bar{A}_3 &= a^2\hat{z} \\
\bar{A}_{32} &= a^2\left(\frac{n_3}{n_2} - \frac{n_1n_3}{2n_2^2}\right)\hat{y} \\
\bar{A}_{321} &= a^2\begin{cases} \left(2\frac{n_3}{n_1} - \frac{n_3}{n_2} - \frac{n_2n_3}{2n_1^2}\right)\hat{x}, n_2 < 2n_1 \\ \frac{n_3}{n_2}\hat{x}, n_2 > 2n_1 \end{cases},
\end{aligned} \tag{99}$$

and

$$\begin{aligned}
P_3 &= -I_0\hat{r}_3 \cdot \bar{A}_3 = I_0a^2n_3 \\
P_{32} &= -RI_0\hat{r}_{32} \cdot \bar{A}_{32} = RI_0a^2\left(n_3 - \frac{n_1n_3}{2n_2}\right) \\
P_{321} &= -R^2I_0\hat{r}_{321} \cdot \bar{A}_{321} \\
&= R^2I_0a^2\begin{cases} \left(2n_3 - \frac{n_1n_3}{n_2} - \frac{n_2n_3}{2n_1}\right), n_2 < 2n_1 \\ \frac{n_1n_3}{n_2}, n_2 > 2n_1 \end{cases}
\end{aligned} \tag{100}$$

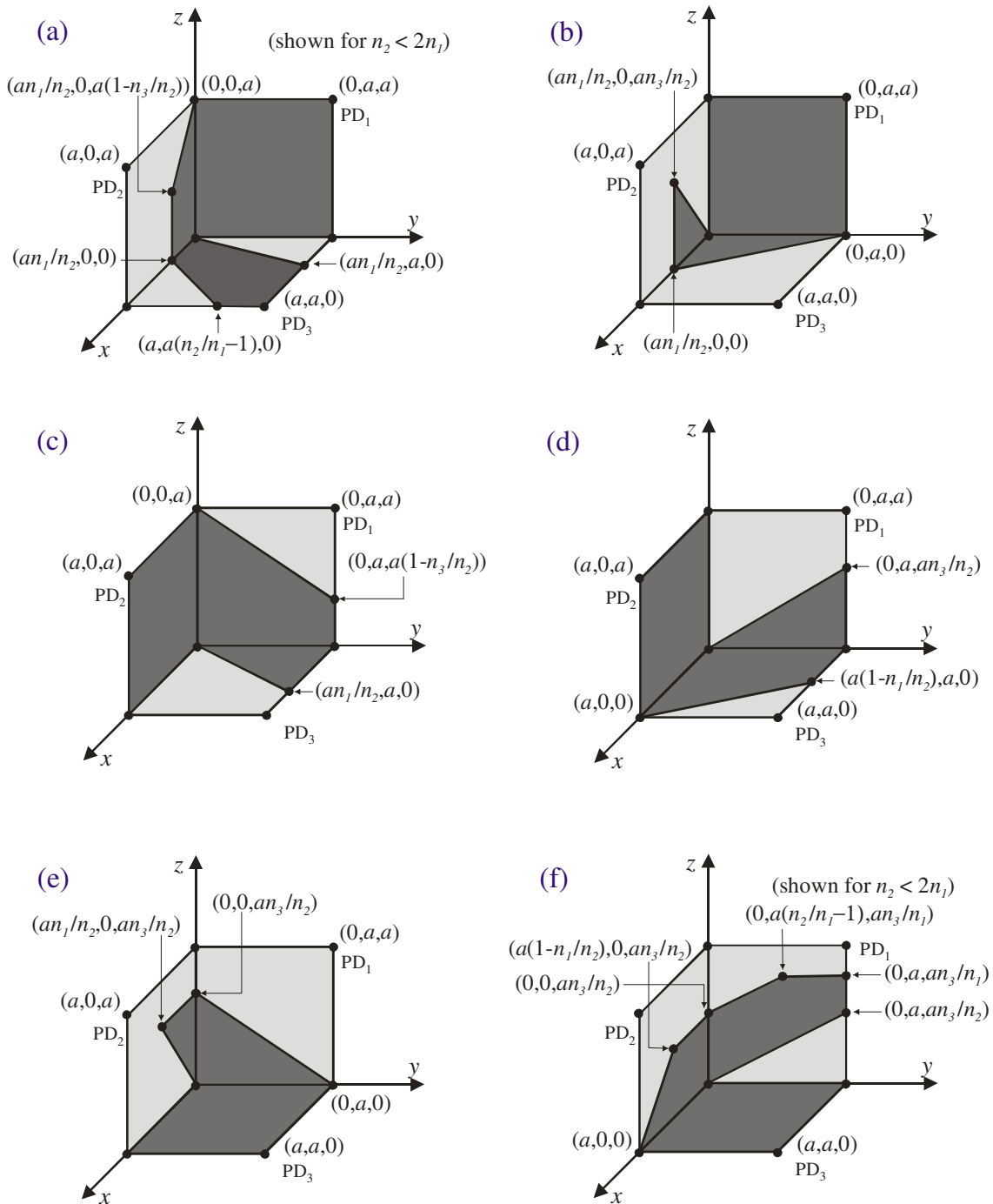


Figure 3.6 Schematics are shown for the internal reflection processes occurring in the retro-detector for directional cosine conditions $n_3 < n_1 < n_2$. Unilluminated areas are shown with light shading. Illuminated areas are shown with dark shading. The order of internal reflections proceeds as (a) PD₁ onto PD₂ onto PD₃, (b) PD₁ onto PD₃ onto PD₂, (c) PD₂ onto PD₁ onto PD₃, (d) PD₂ onto PD₃ onto PD₁, (e) PD₃ onto PD₁ onto PD₂, and (f) PD₃ onto PD₂ onto PD₁.

3.3.2.6. Detected Power Levels for the Sixth Illumination Case with $n_3 < n_2 < n_1$

The final analysis case corresponds to incident illumination with the z , y , and x directional cosine components in increasing order of magnitudes. This $n_3 < n_2 < n_1$ situation is analyzed for the first subcase, in which the incident light strikes PD₁, reflects onto PD₂, and reflects onto PD₃ (and subsequently exits the retro-detector to return to its source). In this case, the light ray unit-normal vectors that are incident on PD₁, PD₂ and PD₃ are

$$\begin{aligned}\hat{r}_1 &= -n_1\hat{x} - n_2\hat{y} - n_3\hat{z} \\ \hat{r}_{12} &= +n_1\hat{x} - n_2\hat{y} - n_3\hat{z} \\ \hat{r}_{123} &= +n_1\hat{x} + n_2\hat{y} - n_3\hat{z},\end{aligned}\tag{101}$$

respectively, where the subscripts indicate the successive illumination and reflection sequence. Fig. 3.7(a) shows the resulting illumination areas for this subcase. Here, PD₁ is fully illuminated and shaded, and its four corner points in the yz -plane are projected along \hat{r}_{12} onto the xz -plane. The resulting shaded PD₂ illumination area is then defined as the overlap between this projected area and the PD₂ surface. Similarly, the PD₂ illumination area is projected along \hat{r}_{123} onto the xy -plane, and the shaded PD₃ illumination is defined as the overlap between this projected area and the PD₃ surface. The resulting illumination area normal vectors can now be defined for this subcase as

$$\begin{aligned}\bar{A}_1 &= a^2\hat{x} \\ \bar{A}_{12} &= a^2\left(1 - \frac{n_3}{2n_1}\right)\hat{y} \\ \bar{A}_{123} &= a^2\frac{n_2}{2n_1}\hat{z}.\end{aligned}\tag{102}$$

The corresponding incident power levels associated with PD₁, PD₂ and PD₃ are then found by taking the component of these illumination area normal vectors in (102) along the respective reflected light ray unit-normal vectors in (101). The result is

$$\begin{aligned}P_1 &= -I_0\hat{r}_1 \cdot \bar{A}_1 = I_0a^2n_1 \\ P_{12} &= -RI_0\hat{r}_{12} \cdot \bar{A}_{12} = RI_0a^2\left(n_2 - \frac{n_2n_3}{2n_1}\right) \\ P_{123} &= -R^2I_0\hat{r}_{123} \cdot \bar{A}_{123} = R^2I_0a^2\frac{n_2n_3}{2n_1}.\end{aligned}\tag{103}$$

The second subcase for $n_3 < n_2 < n_1$ corresponds to the situation with the incident light illuminating PD₁, PD₃, and PD₂, in order. In this case, the respective light ray unit-normal vectors incident on the surfaces of PD₁, PD₃ and PD₂ are

$$\begin{aligned}\hat{r}_1 &= -n_1\hat{x} - n_2\hat{y} - n_3\hat{z} \\ \hat{r}_{13} &= +n_1\hat{x} - n_2\hat{y} - n_3\hat{z} \\ \hat{r}_{132} &= +n_1\hat{x} - n_2\hat{y} + n_3\hat{z}.\end{aligned}\quad (104)$$

Again, the successive illumination areas are referred onto their adjoining neighbors, and the illumination areas are displayed in Fig. 3.7(b) (shown for $n_1 < 2n_2$). Using the shaded areas on this figure, the illumination area normal vectors can be defined as

$$\begin{aligned}\bar{A}_1 &= a^2\hat{x} \\ \bar{A}_{13} &= a^2\left(1 - \frac{n_2}{2n_1}\right)\hat{z} \\ \bar{A}_{132} &= a^2\frac{n_3}{2n_1}\hat{y}.\end{aligned}\quad (105)$$

The corresponding incident power levels associated with PD₁, PD₃ and PD₂ are then found by taking the component of these illumination area normal vectors from (105) along the respective reflected light ray unit-normal vectors from (104). The result is

$$\begin{aligned}P_1 &= -I_0\hat{r}_1 \cdot \bar{A}_1 = I_0a^2n_1 \\ P_{13} &= -RI_0\hat{r}_{13} \cdot \bar{A}_{13} = RI_0a^2\left(n_3 - \frac{n_2n_3}{2n_1}\right) \\ P_{132} &= -R^2I_0\hat{r}_{132} \cdot \bar{A}_{132} = R^2I_0a^2\frac{n_2n_3}{2n_1}.\end{aligned}\quad (106)$$

The third subcase for $n_3 < n_2 < n_1$ is shown in Fig. 3.7(c), and it is characterized by illumination of PD₂, followed by subsequent reflections off PD₁ and PD₃. The light ray unit-normal vectors incident on the surfaces of PD₂, PD₁, and PD₃, respectively, are

$$\begin{aligned}\hat{r}_2 &= -n_1\hat{x} - n_2\hat{y} - n_3\hat{z} \\ \hat{r}_{21} &= -n_1\hat{x} + n_2\hat{y} - n_3\hat{z} \\ \hat{r}_{213} &= +n_1\hat{x} + n_2\hat{y} - n_3\hat{z}.\end{aligned}\quad (107)$$

Using these light ray components and the resulting illumination area projections, the respective illumination area normal vectors can be written for PD₂, PD₁, and PD₃ as

$$\begin{aligned}
\bar{A}_2 &= a^2 \hat{y} \\
\bar{A}_{21} &= a^2 \left(\frac{n_2}{n_1} - \frac{n_2 n_3}{2n_1^2} \right) \hat{x} \\
\bar{A}_{213} &= a^2 \begin{cases} \left(2 - \frac{n_2}{n_1} - \frac{n_1}{2n_2} \right) \hat{z}, n_1 < 2n_2 \\ \frac{n_2}{n_1} \hat{z}, n_1 > 2n_2 \end{cases} .
\end{aligned} \tag{108}$$

The resulting incident power levels associated with PD₂, PD₁, and PD₃ are then found by taking the component of the illumination area normal vectors from (108) along the respective reflected light ray unit-normal vectors from (107), such that

$$\begin{aligned}
P_2 &= -I_0 \hat{r}_2 \cdot \bar{A}_2 = I_0 a^2 n_2 \\
P_{21} &= -RI_0 \hat{r}_{21} \cdot \bar{A}_{21} = RI_0 a^2 \left(n_2 - \frac{n_2 n_3}{2n_1} \right) \\
P_{213} &= -R^2 I_0 \hat{r}_{213} \cdot \bar{A}_{213} \\
&= R^2 I_0 a^2 \begin{cases} \left(2n_3 - \frac{n_2 n_3}{n_1} - \frac{n_1 n_3}{2n_2} \right), n_1 < 2n_2 \\ \frac{n_2 n_3}{n_1}, n_1 > 2n_2 \end{cases} .
\end{aligned} \tag{109}$$

The fourth subcase for $n_3 < n_2 < n_1$ is shown in Fig. 3.7(d), and it corresponds to the case for which PD₂, PD₃, and PD₁ are successively illuminated. The respective light ray unit-normal vectors incident on PD₂, PD₃, and PD₁ can be expressed as

$$\begin{aligned}
\hat{r}_2 &= -n_1 \hat{x} - n_2 \hat{y} - n_3 \hat{z} \\
\hat{r}_{23} &= -n_1 \hat{x} + n_2 \hat{y} - n_3 \hat{z} \\
\hat{r}_{231} &= -n_1 \hat{x} + n_2 \hat{y} + n_3 \hat{z},
\end{aligned} \tag{110}$$

and the PD₂, PD₃, and PD₁ illumination area normal vectors are

$$\begin{aligned}
\bar{A}_2 &= a^2 \hat{y} \\
\bar{A}_{23} &= a^2 \frac{n_2}{2n_1} \hat{z} \\
\bar{A}_{231} &= a^2 \frac{n_2 n_3}{2n_1^2} \hat{x}.
\end{aligned} \tag{111}$$

The PD₂, PD₃, and PD₁ incident powers are then found by taking the illumination area normal vector components in (111) along the reflected light ray unit-normal vectors in (110), giving

$$\begin{aligned}
P_2 &= -I_0 \hat{r}_2 \cdot \bar{A}_2 = I_0 a^2 n_2 \\
P_{23} &= -RI_0 \hat{r}_{23} \cdot \bar{A}_{23} = RI_0 a^2 \frac{n_2 n_3}{2n_1} \\
P_{231} &= -R^2 I_0 \hat{r}_{231} \cdot \bar{A}_{231} = R^2 I_0 a^2 \frac{n_2 n_3}{2n_1}.
\end{aligned} \tag{112}$$

The fifth subcase for $n_3 < n_2 < n_1$ has illumination and reflection conditions shown in Fig. 3.7(e). Here, light rays are reflected in order off of PD₃, PD₁, and PD₂. The light ray unit-normal vectors incident on the surfaces of PD₃, PD₁, and PD₂ become

$$\begin{aligned}
\hat{r}_3 &= -n_1 \hat{x} - n_2 \hat{y} - n_3 \hat{z} \\
\hat{r}_{31} &= -n_1 \hat{x} - n_2 \hat{y} + n_3 \hat{z} \\
\hat{r}_{312} &= +n_1 \hat{x} - n_2 \hat{y} + n_3 \hat{z},
\end{aligned} \tag{113}$$

and the resulting illumination area normal vectors for illumination of PD₃, PD₁, and PD₂ are

$$\begin{aligned}
\bar{A}_3 &= a^2 \hat{z} \\
\bar{A}_{31} &= a^2 \left(\frac{n_3}{n_1} - \frac{n_2 n_2}{2n_1^2} \right) \hat{x} \\
\bar{A}_{312} &= a^2 \begin{cases} \left(2 \frac{n_3}{n_2} - \frac{n_3}{n_1} - \frac{n_1 n_3}{2n_2^2} \right) \hat{y}, n_1 < 2n_2 \\ \frac{n_3}{n_1} \hat{y}, n_1 > 2n_2 \end{cases}.
\end{aligned} \tag{114}$$

The resulting incident power levels recorded by PD₃, PD₁, and PD₂ for this subcase are then found from (113) and (114) to be

$$\begin{aligned}
P_3 &= -I_0 \hat{r}_3 \cdot \bar{A}_3 = I_0 a^2 n_3 \\
P_{31} &= -RI_0 \hat{r}_{31} \cdot \bar{A}_{31} = RI_0 a^2 \left(n_3 - \frac{n_2 n_3}{2n_1} \right) \\
P_{312} &= -R^2 I_0 \hat{r}_{312} \cdot \bar{A}_{312} \\
&= R^2 I_0 a^2 \begin{cases} \left(2n_3 - \frac{n_2 n_3}{n_1} - \frac{n_1 n_3}{2n_2} \right), n_1 < 2n_2 \\ \frac{n_2 n_3}{n_1}, n_1 > 2n_2 \end{cases}.
\end{aligned} \tag{115}$$

The sixth and final subcase for $n_3 < n_2 < n_1$ is displayed in Fig. 3.7(f). The surface of PD₃ is illuminated first, followed by successive reflections off of PD₂ and PD₁. The light ray unit-normal vectors for this succession are

$$\begin{aligned}
\hat{r}_3 &= -n_1\hat{x} - n_2\hat{y} - n_3\hat{z} \\
\hat{r}_{32} &= -n_1\hat{x} - n_2\hat{y} + n_3\hat{z} \\
\hat{r}_{321} &= -n_1\hat{x} + n_2\hat{y} + n_3\hat{z}.
\end{aligned} \tag{116}$$

The resulting illumination area normal vectors and detected power levels for PD₃, PD₂, and PD₁ are

$$\begin{aligned}
\bar{A}_3 &= a^2\hat{z} \\
\bar{A}_{32} &= a^2\frac{n_3}{2n_1}\hat{y} \\
\bar{A}_{321} &= a^2\frac{n_2n_3}{2n_1}\hat{x}.
\end{aligned} \tag{117}$$

and

$$\begin{aligned}
P_3 &= -I_0\hat{r}_3 \cdot \bar{A}_3 = I_0a^2n_3 \\
P_{32} &= -RI_0\hat{r}_{32} \cdot \bar{A}_{32} = RI_0a^2\frac{n_2n_3}{2n_1} \\
P_{321} &= -R^2I_0\hat{r}_{321} \cdot \bar{A}_{321} = R^2I_0a^2\frac{n_2n_3}{2n_1}.
\end{aligned} \tag{118}$$

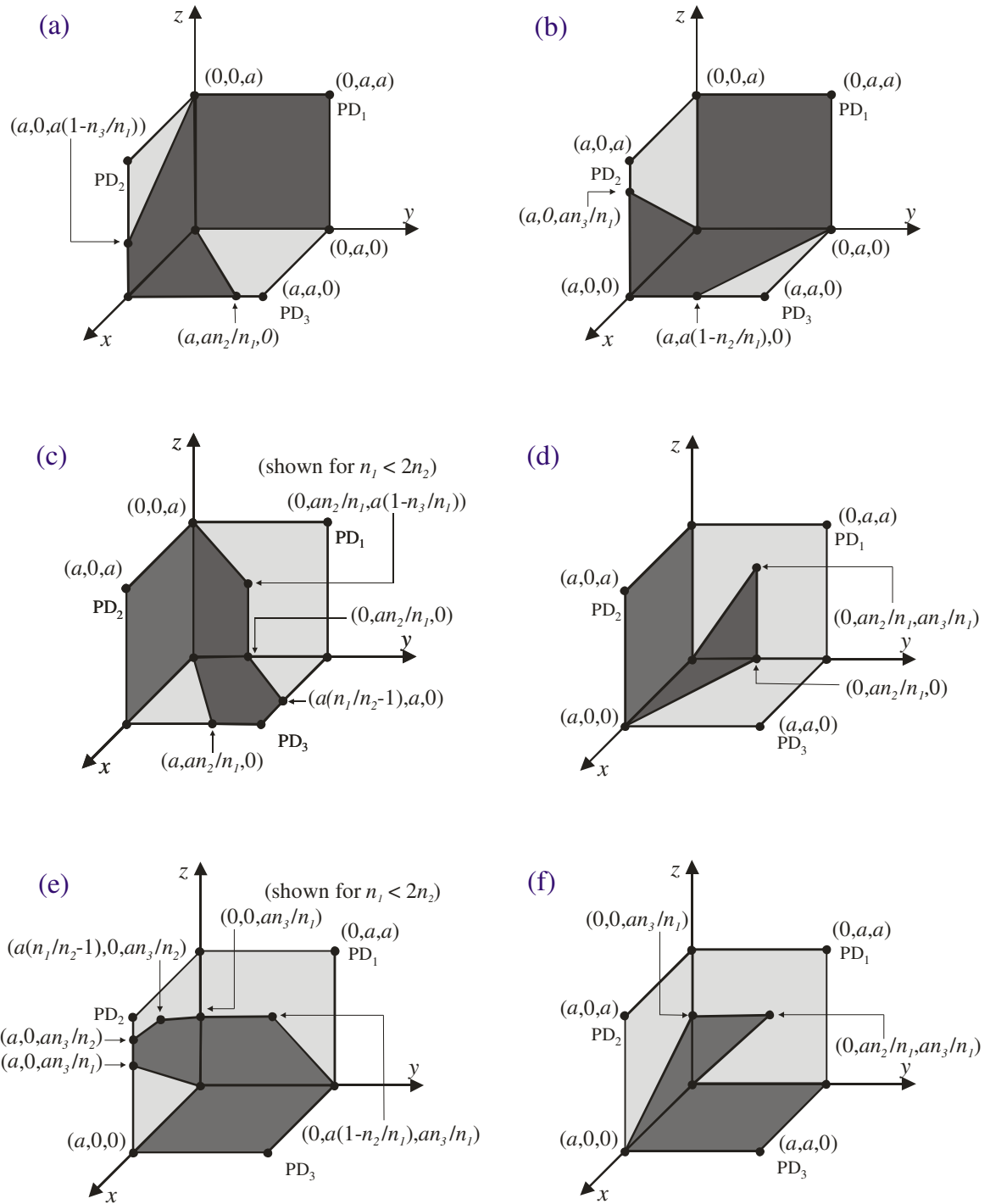


Figure 3.7 Schematics are shown for the internal reflection processes occurring in the retro-detector for directional cosine conditions $n_3 < n_2 < n_1$. Unilluminated areas are shown with light shading. Illuminated areas are shown with dark shading. The order of internal reflections proceeds as (a) PD₁ onto PD₂ onto PD₃, (b) PD₁ onto PD₃ onto PD₂, (c) PD₂ onto PD₁ onto PD₃, (d) PD₂ onto PD₃ onto PD₁, (e) PD₃ onto PD₁ onto PD₂, and (f) PD₃ onto PD₂ onto PD₁.

3.3.2.7. Summary of Photocurrent Levels for all Six Illumination Cases

The illumination cases described above are all well-defined for six directional cosine cases, though each differs in its successive ordering of illumination and reflection. The ultimate detected power levels observed for each of the three PDs will be a result of all the derived possible reflection permutations that culminate in their respective PD area being illuminated. To be exact, the total incident power level detected on PD₁ will include five components: i. the direct incident power onto PD₁, ii. the reflected power due to a primary reflection off PD₂, iii. the reflected power due to a primary reflection off PD₃, iv. the reflected power due to a primary reflection off PD₂ followed by a secondary reflection off PD₃, and v. the reflected power due to a primary reflection off PD₃ followed by a secondary reflection off PD₂. The resulting total power permutations are

$$\begin{aligned}
 P_{1-total} &= P_1 + P_{21} + P_{31} + P_{231} + P_{321} \\
 P_{2-total} &= P_2 + P_{12} + P_{32} + P_{312} + P_{132} \\
 P_{3-total} &= P_3 + P_{13} + P_{23} + P_{123} + P_{213},
 \end{aligned} \tag{119}$$

respectively, where the subscripts indicate the successive illumination and reflection sequence. The corresponding photocurrents, i_1 , i_2 , i_3 , can be found by summing the respective subcase power levels and applying a responsivity constant of proportionality which describes both the internal PD quantum efficiency and optical transmissivity through the interface. For the ease of comparison among differential channels, the PD photocurrents can be normalized with respect to this responsivity and $I_0 a^2$. For the first case with $n_1 < n_2 < n_3$, the photocurrents can be written as

$$\begin{aligned}
 i_1(n_1 < n_2 < n_3) &= n_1 + Rn_1 + R^2 \begin{cases} \left(2n_1 - \frac{n_1 n_2}{2n_3} - \frac{n_1 n_3}{2n_2} \right), n_3 < 2n_2 \\ \frac{3n_1 n_2}{2n_3}, n_3 > 2n_2 \end{cases} \\
 i_2(n_1 < n_2 < n_3) &= n_2 + Rn_2 + R^2 \begin{cases} \left(2n_1 - \frac{n_1 n_2}{2n_3} - \frac{n_1 n_3}{2n_2} \right), n_3 < 2n_2 \\ \frac{3n_1 n_2}{2n_3}, n_3 > 2n_2 \end{cases} \\
 i_3(n_1 < n_2 < n_3) &= n_3 + R \left(n_1 + n_2 - \frac{n_1 n_2}{n_3} \right) + R^2 \frac{n_1 n_2}{n_3}.
 \end{aligned} \tag{120}$$

While the above PD₁, PD₂, and PD₃ photocurrents have been defined explicitly for the directional cosine case of $n_1 < n_2 < n_3$, the photocurrents can be explicitly stated for the remaining five permutations with the same analysis procedure. Interestingly, the resulting expressions can be confirmed by rotational and mirror symmetries in these derivations. For the second incident light ray case, the x -, z -, and y -components of the incident light ray are in ascending order of magnitudes, and the inequality $n_1 < n_3 < n_2$ leads to three normalized photocurrents with

$$\begin{aligned}
i_1(n_1 < n_3 < n_2) &= n_1 + Rn_1 + R^2 \begin{cases} \left(2n_1 - \frac{n_1 n_3}{2n_2} - \frac{n_1 n_2}{2n_3} \right), n_2 < 2n_3 \\ \frac{3n_1 n_3}{2n_2}, n_2 > 2n_3 \end{cases} \\
i_2(n_1 < n_3 < n_2) &= n_2 + R(n_1 + n_3 - \frac{n_1 n_3}{n_2}) + R^2 \frac{n_1 n_3}{n_2} \\
i_3(n_1 < n_3 < n_2) &= n_3 + Rn_3 + R^2 \begin{cases} \left(2n_1 - \frac{n_1 n_3}{2n_2} - \frac{n_1 n_2}{2n_3} \right), n_2 < 2n_3 \\ \frac{3n_1 n_3}{2n_2}, n_2 > 2n_3 \end{cases} . \quad (121)
\end{aligned}$$

For the third case, with $n_2 < n_1 < n_3$, the y -, x -, and z -components of the incident light ray are in an ascending order of magnitudes, and the three normalized photocurrents become

$$\begin{aligned}
i_1(n_2 < n_1 < n_3) &= n_1 + Rn_1 + R^2 \begin{cases} \left(2n_2 - \frac{n_1 n_2}{2n_3} - \frac{n_2 n_3}{2n_1} \right), n_3 < 2n_1 \\ \frac{3n_1 n_2}{2n_3}, n_3 > 2n_1 \end{cases} \\
i_2(n_2 < n_1 < n_3) &= n_2 + Rn_2 + R^2 \begin{cases} \left(2n_2 - \frac{n_1 n_2}{2n_3} - \frac{n_2 n_3}{2n_1} \right), n_3 < 2n_1 \\ \frac{3n_1 n_2}{2n_3}, n_3 > 2n_1 \end{cases} \\
i_3(n_2 < n_1 < n_3) &= n_3 + R(n_1 + n_2 - \frac{n_1 n_2}{n_3}) + R^2 I_0 a^2 \frac{n_1 n_2}{n_3} . \quad (122)
\end{aligned}$$

For the fourth case, with $n_2 < n_3 < n_1$, the y -, z -, and x -components of the incident light ray are in an ascending order of magnitudes. The resulting three normalized photocurrents for PD₁, PD₂, and PD₃ can then be written as

$$\begin{aligned}
i_1(n_2 < n_3 < n_1) &= n_1 + R \left(n_2 + n_3 - \frac{n_2 n_3}{n_1} \right) + R^2 \frac{n_2 n_3}{n_1} \\
i_2(n_2 < n_3 < n_1) &= n_2 + R n_2 + R^2 \begin{cases} \left(2n_2 - \frac{n_2 n_3}{2n_1} - \frac{n_1 n_2}{2n_3} \right), n_1 < 2n_3 \\ \frac{3n_2 n_3}{2n_1}, n_1 > 2n_3 \end{cases} \\
i_3(n_2 < n_3 < n_1) &= n_3 + R n_3 + R^2 \begin{cases} \left(2n_2 - \frac{n_2 n_3}{2n_1} - \frac{n_1 n_2}{2n_3} \right), n_1 < 2n_3 \\ \frac{3n_2 n_3}{2n_1}, n_1 > 2n_3 \end{cases} .
\end{aligned} \tag{123}$$

For the fifth case, with $n_3 < n_1 < n_2$, the z -, x -, and y -components of the incident light ray are in an ascending order of magnitudes, and the normalized PD₁, PD₂, and PD₃ photocurrents become

$$\begin{aligned}
i_1(n_3 < n_1 < n_2) &= n_1 + R n_1 + R^2 \begin{cases} \left(2n_3 - \frac{n_1 n_3}{2n_2} - \frac{n_2 n_3}{2n_1} \right), n_2 < 2n_1 \\ \frac{3n_1 n_3}{2n_2}, n_2 > 2n_1 \end{cases} \\
i_2(n_3 < n_1 < n_2) &= n_2 + R \left(n_1 + n_3 - \frac{n_1 n_3}{n_2} \right) + R^2 \frac{n_1 n_3}{n_2} \\
i_3(n_3 < n_1 < n_2) &= n_3 + R n_3 + R^2 \begin{cases} \left(2n_3 - \frac{n_1 n_3}{2n_2} - \frac{n_2 n_3}{2n_1} \right), n_2 < 2n_1 \\ \frac{3n_1 n_3}{2n_2}, n_2 > 2n_1 \end{cases} .
\end{aligned} \tag{124}$$

For the sixth and final case, with $n_3 < n_2 < n_1$, the z -, y -, and x -components of the incident light ray are in an ascending order of magnitudes. The resulting three normalized photocurrents are

$$\begin{aligned}
i_1(n_3 < n_2 < n_1) &= n_1 + R \left(n_2 + n_3 - \frac{n_2 n_3}{n_1} \right) + R^2 \frac{n_2 n_3}{n_1} \\
i_2(n_3 < n_2 < n_1) &= n_2 + R n_2 + R^2 \begin{cases} \left(2n_3 - \frac{n_2 n_3}{2n_1} - \frac{n_1 n_3}{2n_2} \right), n_1 < 2n_2 \\ \frac{3n_2 n_3}{2n_1}, n_1 > 2n_2 \end{cases}
\end{aligned}$$

$$i_3(n_3 < n_2 < n_1) = n_3 + Rn_3 + R^2 \begin{cases} \left(2n_3 - \frac{n_2n_3}{2n_1} - \frac{n_1n_3}{2n_2}\right), n_1 < 2n_2 \\ \frac{3n_2n_3}{2n_1}, n_1 > 2n_2 \end{cases}. \quad (125)$$

The complete photocurrent expressions for individual PDs are summarized in Table 3.1 for the six incident light ray directional cosine component inequalities.

Cases	PD ₁ Normalized Photocurrents	PD ₂ Normalized Photocurrents	PD ₃ Normalized Photocurrents
$n_1 < n_2 < n_3$	$n_1 + Rn_1 + R^2 \begin{cases} \left(2n_1 - \frac{n_1n_2}{2n_3} - \frac{n_1n_3}{2n_2}\right), n_3 < 2n_2 \\ \frac{3n_1n_2}{2n_3}, n_3 > 2n_2 \end{cases}$	$n_2 + Rn_2 + R^2 \begin{cases} \left(2n_1 - \frac{n_1n_2}{2n_3} - \frac{n_1n_3}{2n_2}\right), n_3 < 2n_2 \\ \frac{3n_1n_2}{2n_3}, n_3 > 2n_2 \end{cases}$	$n_3 + R \left(n_1 + n_2 - \frac{n_1n_2}{n_3}\right) + R^2 \frac{n_1n_2}{n_3}$
$n_1 < n_3 < n_2$	$n_1 + Rn_1 + R^2 \begin{cases} \left(2n_1 - \frac{n_1n_3}{2n_2} - \frac{n_1n_2}{2n_3}\right), n_2 < 2n_3 \\ \frac{3n_1n_3}{2n_2}, n_2 > 2n_3 \end{cases}$	$n_2 + R(n_1 + n_3 - \frac{n_1n_3}{n_2}) + R^2 \frac{n_1n_3}{n_2}$	$n_3 + Rn_3 + R^2 \begin{cases} \left(2n_1 - \frac{n_1n_3}{2n_2} - \frac{n_1n_2}{2n_3}\right), n_2 < 2n_3 \\ \frac{3n_1n_3}{2n_2}, n_2 > 2n_3 \end{cases}$
$n_2 < n_1 < n_3$	$n_1 + Rn_1 + R^2 \begin{cases} \left(2n_2 - \frac{n_1n_2}{2n_3} - \frac{n_2n_3}{2n_1}\right), n_3 < 2n_1 \\ \frac{3n_1n_2}{2n_3}, n_3 > 2n_1 \end{cases}$	$n_2 + Rn_2 + R^2 \begin{cases} \left(2n_2 - \frac{n_1n_2}{2n_3} - \frac{n_2n_3}{2n_1}\right), n_3 < 2n_1 \\ \frac{3n_1n_2}{2n_3}, n_3 > 2n_1 \end{cases}$	$n_3 + R(n_1 + n_2 - \frac{n_1n_2}{n_3}) + R^2 \frac{n_1n_2}{n_3}$
$n_2 < n_3 < n_1$	$n_1 + R \left(n_2 + n_3 - \frac{n_2n_3}{n_1}\right) + R^2 \frac{n_2n_3}{n_1}$	$n_2 + Rn_2 + R^2 \begin{cases} \left(2n_2 - \frac{n_2n_3}{2n_1} - \frac{n_1n_2}{2n_3}\right), n_1 < 2n_3 \\ \frac{3n_2n_3}{2n_1}, n_1 > 2n_3 \end{cases}$	$n_3 + Rn_3 + R^2 \begin{cases} \left(2n_2 - \frac{n_2n_3}{2n_1} - \frac{n_1n_2}{2n_3}\right), n_1 < 2n_3 \\ \frac{3n_2n_3}{2n_1}, n_1 > 2n_3 \end{cases}$
$n_3 < n_1 < n_2$	$n_1 + Rn_1 + R^2 \begin{cases} \left(2n_3 - \frac{n_1n_3}{2n_2} - \frac{n_2n_3}{2n_1}\right), n_2 < 2n_1 \\ \frac{3n_1n_3}{2n_2}, n_2 > 2n_1 \end{cases}$	$n_2 + R \left(n_1 + n_3 - \frac{n_1n_3}{n_2}\right) + R^2 \frac{n_1n_3}{n_2}$	$n_3 + Rn_3 + R^2 \begin{cases} \left(2n_3 - \frac{n_1n_3}{2n_2} - \frac{n_2n_3}{2n_1}\right), n_2 < 2n_1 \\ \frac{3n_1n_3}{2n_2}, n_2 > 2n_1 \end{cases}$
$n_3 < n_2 < n_1$	$n_1 + R \left(n_2 + n_3 - \frac{n_2n_3}{n_1}\right) + R^2 \frac{n_2n_3}{n_1}$	$n_2 + Rn_2 + R^2 \begin{cases} \left(2n_3 - \frac{n_2n_3}{2n_1} - \frac{n_1n_3}{2n_2}\right), n_1 < 2n_2 \\ \frac{3n_2n_3}{2n_1}, n_1 > 2n_2 \end{cases}$	$n_3 + Rn_3 + R^2 \begin{cases} \left(2n_3 - \frac{n_2n_3}{2n_1} - \frac{n_1n_3}{2n_2}\right), n_1 < 2n_2 \\ \frac{3n_2n_3}{2n_1}, n_1 > 2n_2 \end{cases}$

Table 3.1 Theoretical normalized differential photocurrents for PD₁, PD₂ and PD₃, given various directional cosine component inequality permutations.

3.3.3. Control Characteristics

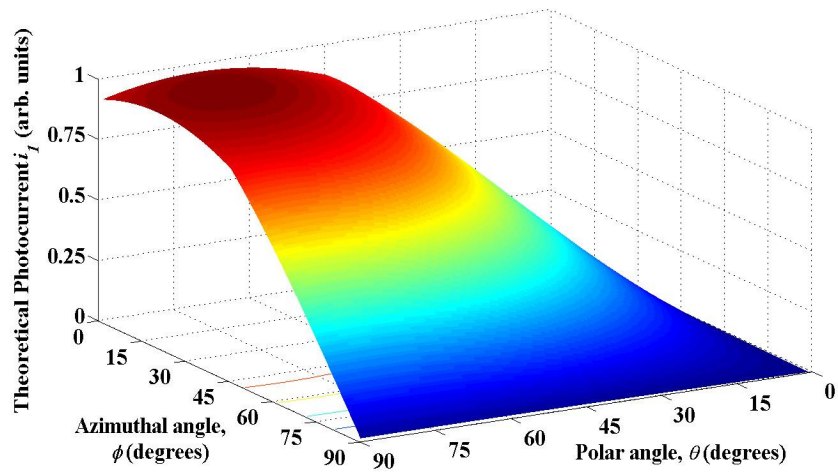
In the previous two subsections (sections 3.3.1 and 3.3.2), the reflection and detection characteristics of the corner-cube geometry were explored for the orthogonal PD structure. It is shown in this section that the complete retro-detector construction can be used as an active control device for optimizing the incident optical signal alignment, as a strong dependence exists among the individual PD photocurrent levels and the incident light ray components. This dependence is readily apparent in Figs. 3.8(a)-(c), where the three normalized theoretical photocurrents from (120)-(125) are displayed. The photocurrents here are plotted as a function of the azimuthal angle ϕ and polar angle θ . Notice from these figures that the photocurrent maxima for each of PD₁, PD₂, and PD₃ correspond to situations in which the respective PD surface is orthogonal to the incident light rays and the greatest amount of light is absorbed. Likewise, negligible photocurrents are observed when the respective PD surface is parallel to the incident light rays and the least amount of light is absorbed.

The directionality of the three PD photocurrents can be used for active control and optimization through a combination of differential sums. If, for example, PD₁ and PD₂ have the same photocurrent level, it can be expected that the incident light rays are balanced between the xz - and yz -planes. This alignment corresponds to the situation for which the optical source lies along the $\phi = 45^\circ$ plane. The same directionality arguments can be made by quantifying and balancing the differential signals between PD₂ and PD₃ and then PD₁ and PD₃, and the final perfect optical alignment corresponds to the situation for which the optical source lies along the $[+1 +1 +1]$ direction.

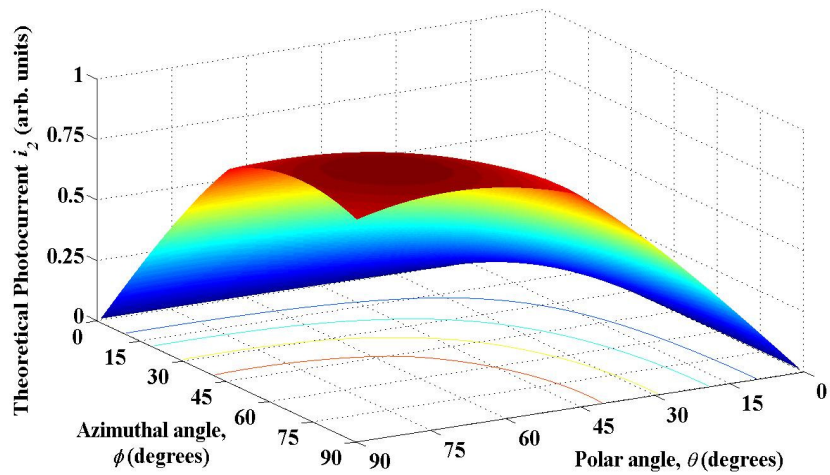
The complete procedure for balancing and optimizing the photocurrent signals can be observed most easily by summing the three differential sum magnitudes. The result is shown as a surface in Fig. 3.9(a), where this photocurrent differential sum is defined as

$$i_{diff}(\phi, \theta) = |i_3(\phi, \theta) - i_2(\phi, \theta)| + |i_3(\phi, \theta) - i_1(\phi, \theta)| + |i_2(\phi, \theta) - i_1(\phi, \theta)|. \quad (126)$$

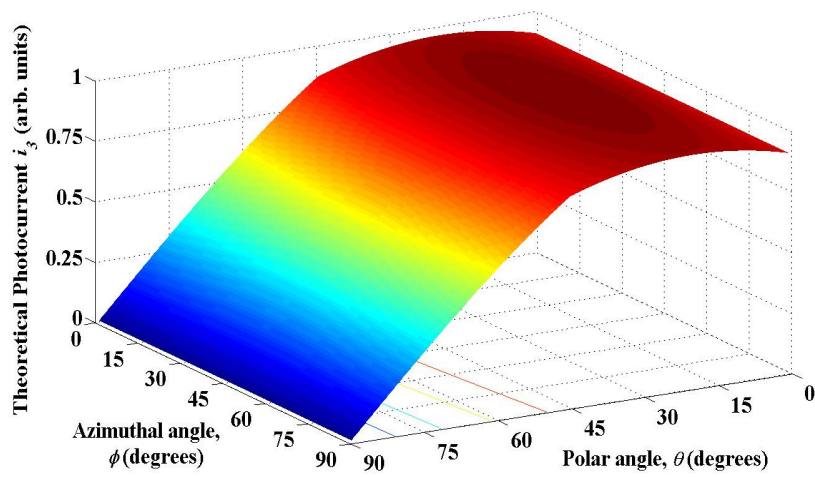
Minimizing this photocurrent differential sum corresponds to an optimization of the angular alignment, with the balanced condition achieved when the absolute minimum of the displayed surface is reached. Moreover, the concavity of the presented photocurrent differential sum allows this minimization to occur in two independent steps. The azimuthal angle ϕ can be minimized first, for example, while θ is kept constant, then the polar angle θ can be minimized as ϕ is kept



(a)



(b)



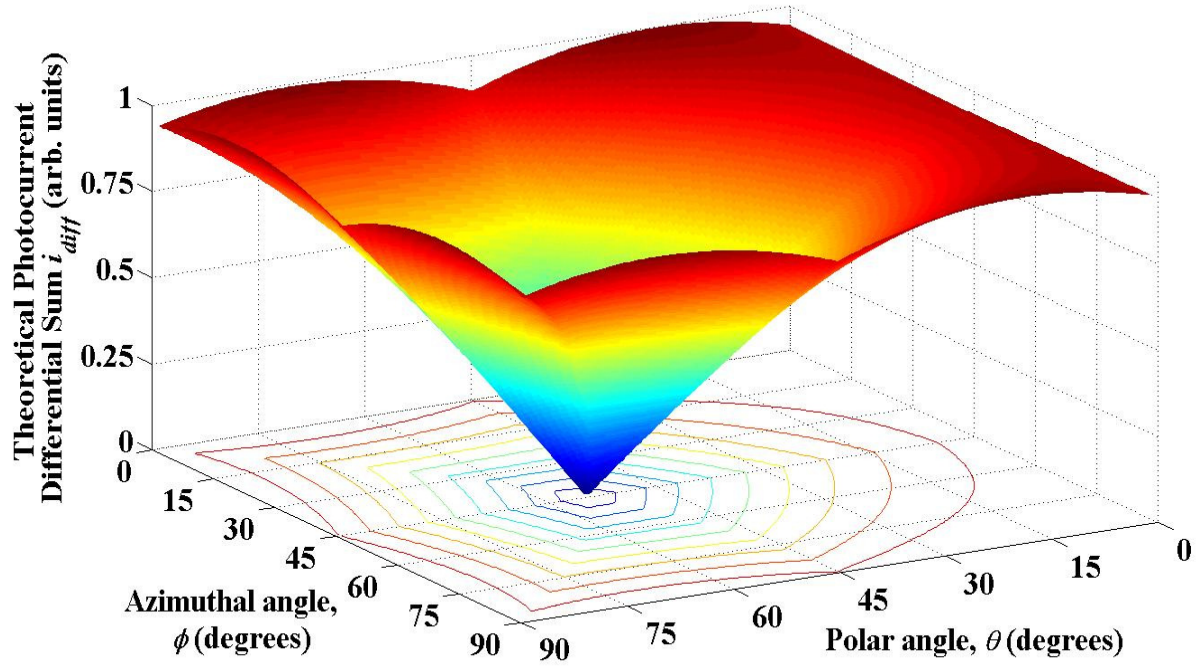
(c)

Figure 3.8 Theoretical photocurrents are shown as surfaces varying with ϕ and θ . Independent and normalized photocurrents are displayed for (a) P_1 , (b) P_2 , and (c) P_3 .

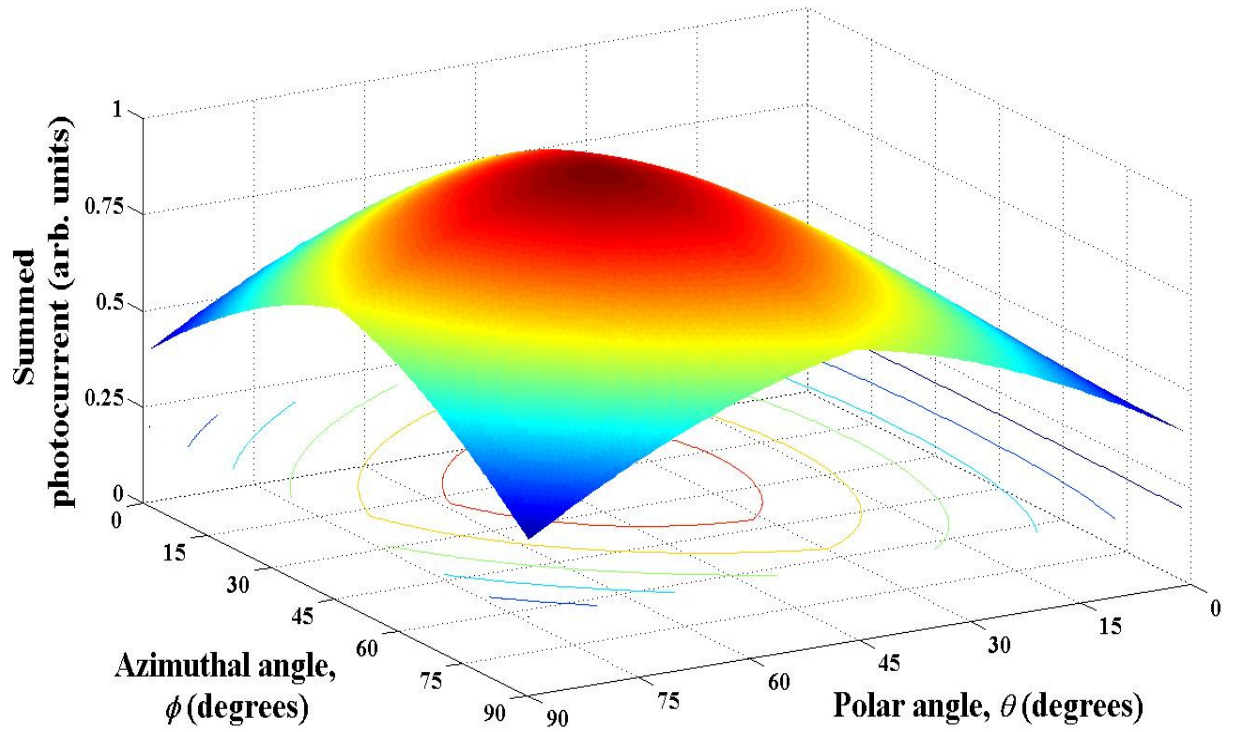
constant. Such a process will bring the retro-detector alignment to the $\phi = 45^\circ$ and $\theta = \cos^{-1}(1/\sqrt{3}) \approx 54.7^\circ$ absolute minimum of the Fig. 3.9(a) surface with the incident light rays entering the structure along the $\hat{r} = -\hat{x} - \hat{y} - \hat{z}$ direction. The absolute minimum condition for the photocurrent differential sum brings the system into alignment for optimal bi-directional communication with both detection and retroreflection being optimized.

From a detection standpoint, the summed photocurrent is recorded by combining the individual PD photocurrents. The absolute minimum of the differential photocurrent sum concavity in Fig. 3.9(a) is then transferred to the absolute maximum of the summed photocurrent convexity of Fig. 3.9(b), and this orientation gives optimal detection conditions. In contrast to this, differential photocurrent sum maxima at $(\phi, \theta) = (0^\circ, 0^\circ), (90^\circ, 0^\circ), (0^\circ, 90^\circ)$ and $(90^\circ, 90^\circ)$ correspond to minima and poor detection conditions for the summed photocurrent minima at these extreme orientations. The retro-detection optimization procedure leading to an orientation of $\phi = 45^\circ$ and $\theta \approx 54.7^\circ$ will therefore bring the system into alignment for optimal signal detection.

From a retroreflection standpoint, the alignment optimization procedure will bring the system into an orientation for optimal retroreflection. The theoretical retroreflected power of this photocell is shown as a surface varying with ϕ and θ in 3D and 2D views in Figs. 3.10(a) and (b), respectively. It is readily apparent that the maximum retroreflected power appears at the optimal orientation of $\phi = 45^\circ$ and $\theta \approx 54.7^\circ$. In contrast to this, the dark blue regions around the periphery at $(\phi, \theta) = (0^\circ, 0^\circ), (90^\circ, 0^\circ), (0^\circ, 90^\circ)$ and $(90^\circ, 90^\circ)$ correspond to near-zero retroreflection from the photocell. (These characteristics at the extreme orientations can be also considered as a motivation for bevelling the extreme points in the previously-described composite structure.) Ultimately, the described differential triangulation and optimization procedure can bring the system into optimal alignment for bi-directional FSO communication with enhanced detection and retroreflection.

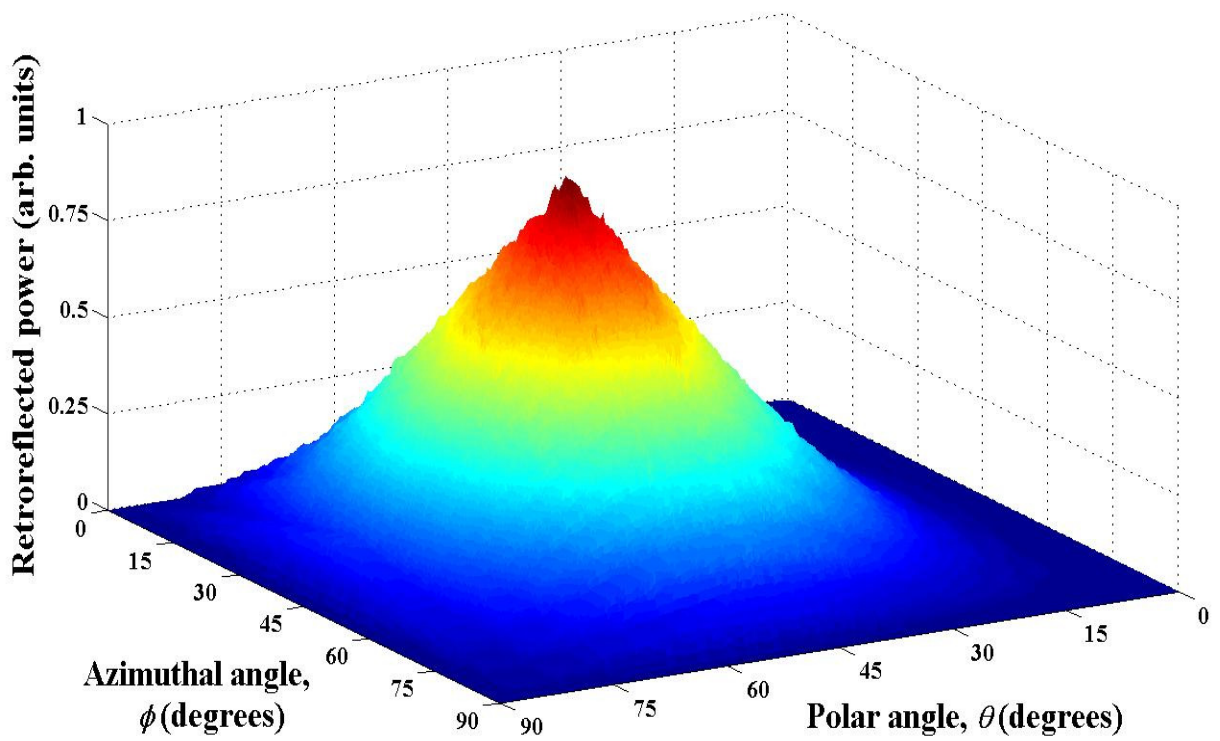


(a)

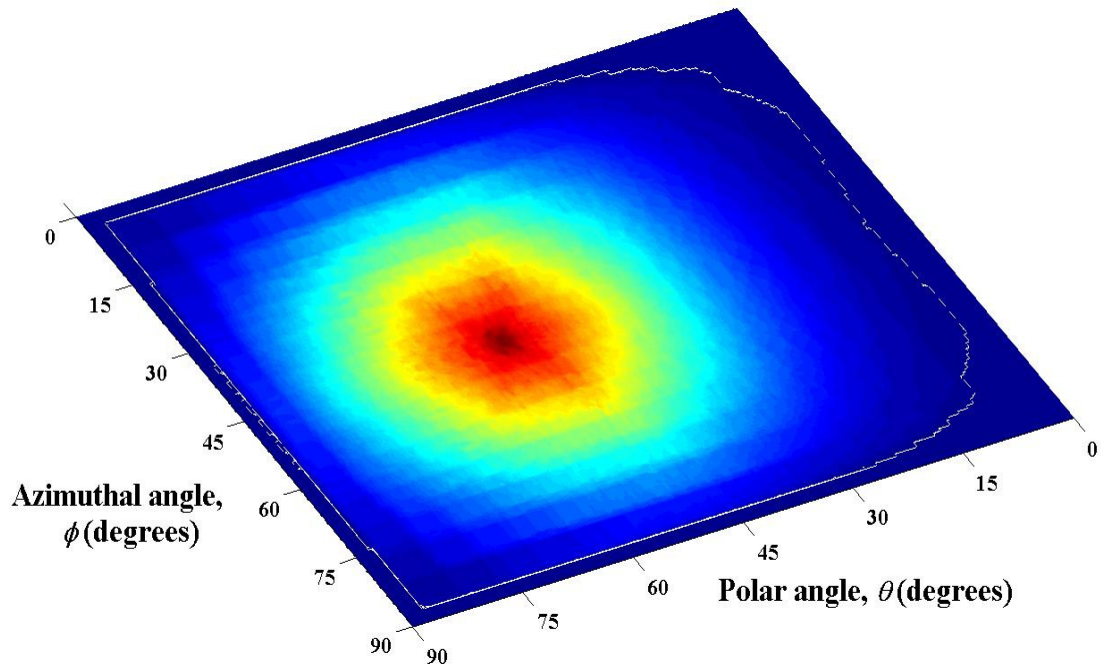


(b)

Figure 3.9 The (a) theoretical photocurrent differential sum and (b) theoretical summed photocurrent are shown as a surface varying with ϕ and θ . This figure is produced by the analytical expressions derived in this chapter.



(a)



(b)

Figure 3.10 The (a) 3D view and (b) 2D view of theoretical retroreflected power are shown as a surface varying with ϕ and θ . This figure is produced by the analytical expressions derived in this chapter.

The operation of the retro-detection photocell is fundamentally based on the asymmetric illumination levels for the constituent PDs. This point was demonstrated in the previous analytic methodology, and the relationship between the illumination asymmetry and differential photocurrents is quantified by the effects of internal reflections, as the light incident on any particular photodiode is a combination of directly-incident light and light reflecting off neighbouring PDs. The resulting optical response described by the analytical expressions in this chapter are validated here with a (brute-force) Matlab ray-tracing approach, for which the structure is illuminated from a uniform intensity grid at various ϕ and θ directions. Details on this model are given in the appendix.

The intensity of each ray is tracked in the Matlab ray-tracing model through the multiple absorption and reflection processes of each silicon PD. The resulting photocurrents are extracted as a function of the model's incident ϕ and θ directions, and the sum of the differential photocurrent magnitudes $|i_{1-2}(t)| + |i_{1-3}(t)| + |i_{2-3}(t)|$ is shown for this model in Fig. 3.11 with the angular range defined by $0 \leq \phi \leq 45^\circ$ and $0 \leq \theta \leq 90^\circ$. It is readily apparent from these results in Fig. 3.11 that the ray-tracing model is in excellent agreement with the algebraic expressions derived in this chapter (and plotted in Fig. 3.9(a)).

The fundamental goal of optimizing the beam alignment can be viewed on the Matlab ray-tracing model curve of Fig. 3.11 by traveling from any initial ϕ and θ location to the absolute minimum at $\phi = 45^\circ$ and $\theta = \cos^{-1}(1/\sqrt{3}) \approx 54.7^\circ$. This procedure is carried out through the independent ϕ and θ differential photocurrent minimization/rotation processes described above. A representative optimization procedure is shown by the line ABD or ACD in Fig. 3.11 as ϕ is optimized from 10° to 45° and θ is then optimized from 5° to 54.7° , or θ is optimized from 5° to 54.7° and ϕ is then optimized from 10° to 45° , respectively. Note that the internal reflections lessen the steepness of figure surface, but they do not prevent the desired complete optimization process. Physically, this is due to the fact that the optimal $(x,y,z) = (1,1,1)$ alignment is characterized by balanced incident light levels *and* balanced internal reflection light levels.

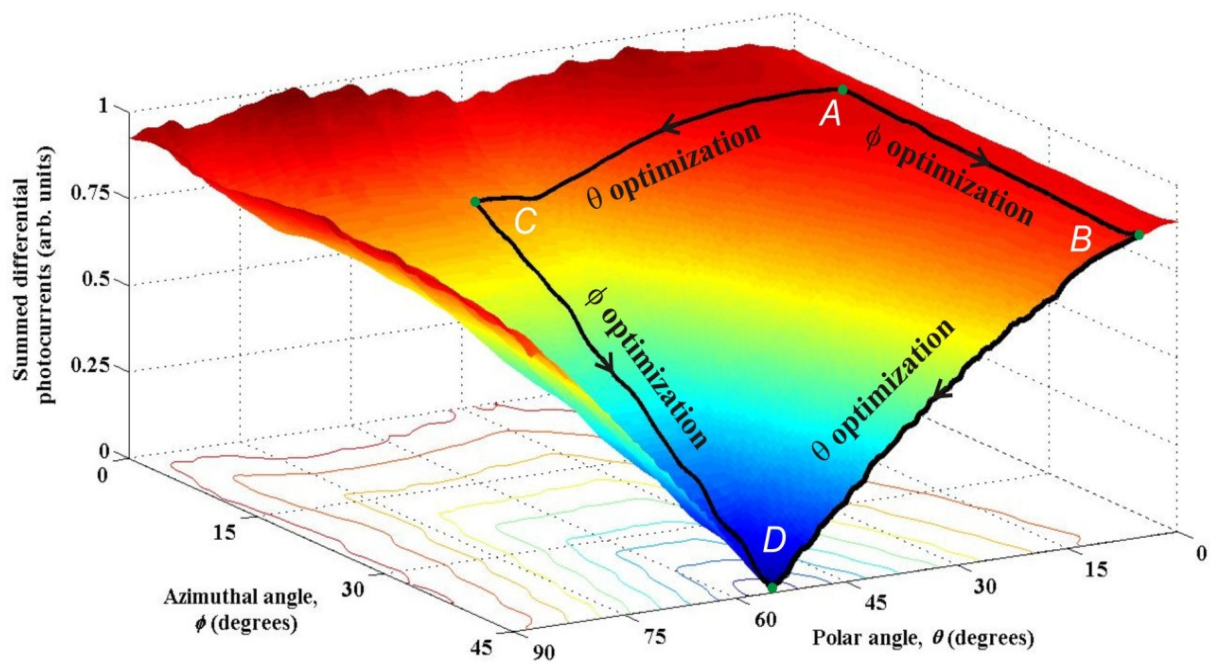


Figure 3.11 Theoretical Matlab ray-tracing model results for the retro-detector's photocurrent differential sum are shown. The summed differential photocurrent is shown as a function of the azimuthal angle ϕ and the polar angle θ . An example of an optimization process is shown by the black trace along either ABC or ABD curve.

3.4. Experimental Framework

In the previous section, the theory and methodology for reflection, detection and control were described for differential detection in the proposed retro-detection photocell. This photocell (shown in Fig. 3.1) is now tested experimentally by way of a broadband LED optical broadcasting configuration and a monochromatic laser configuration with uniform illumination. In the following two subsections, the control capability and communication capability of the proposed retro-detector architecture are systematically investigated.

3.4.1. Verification of the Control Capability

To investigate the angular-dependence of the power distribution characteristic for this retro-detection system, a long-range laser-based FSO setup is built. The setup covers a 10 m propagation range, and testing is carried out with a 1 mW, 650 nm laser diode as the illumination source. The photocell is rotated in a gyroscope with independent ϕ and θ orientations. The laser beam is expanded to a sufficiently large and collimated spot size to uniformly illuminate the retro-detection photocell, and a digital data acquisition system is employed to monitor the differential photocurrents and apply the required orientation optimization and control. The retro-detection photocell is then tested with 1 kHz modulation on the laser diode source and an on-state (open) condition for the Pi-cell LC modulator [38]. The three photocell photocurrents are tracked as a function of time with the laser source sampled at three different locations in the facility. Each of these locations corresponds to a propagation distance of 9 m, with orientations of $\phi = 20^\circ, 30^\circ,$ and 45° and a polar angle of $\theta \approx 54.7^\circ$. The results are shown in Figs. 3.12(a)-(c), respectively, with the resulting differential photocurrents $i_{1-2}(t)$, $i_{1-3}(t)$, and $i_{2-3}(t)$ shown in the lower half of each figure. It is apparent that the largest differential signal levels are exhibited in Fig. 3.12(a). This is the result of the significant misalignment for this orientation, as PD₁ has a disproportionately large illumination power. This is also qualitatively evident from the photocell alignment, whose orientation, as viewed from the laser, is shown in the figure inset. The alignment balancing is improved for the results of Fig. 3.12(b), as the orientation exhibits only a partial misalignment and reduced differential photocurrents. The system becomes completely balanced for the results of Fig. 3.12(c), as this alignment has negligible differential photocurrent levels. It is in this final balanced orientation that the retro-detection photocell is aligned for optimal transmission and reception along the $(x,y,z) = (1,1,1)$ direction.

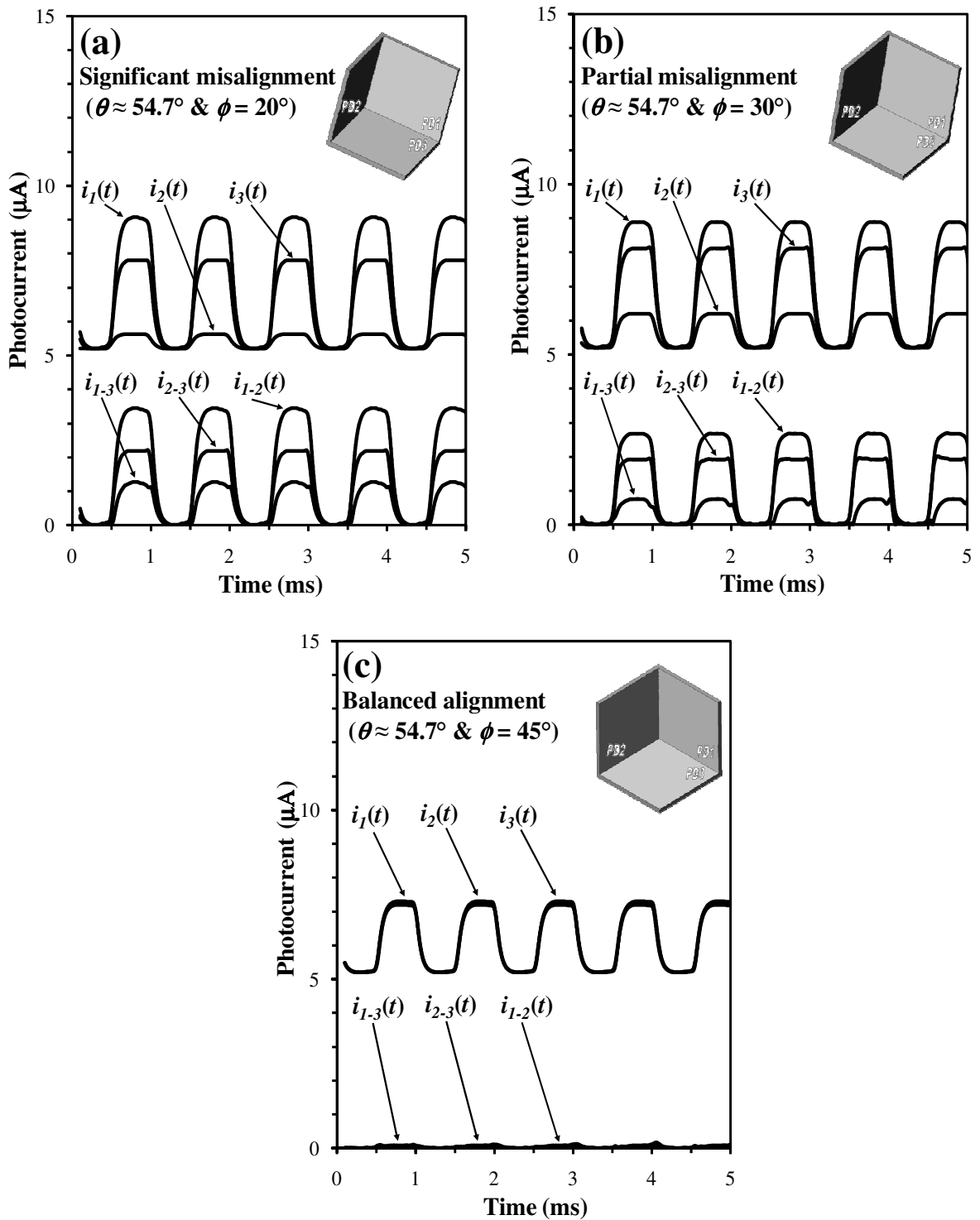
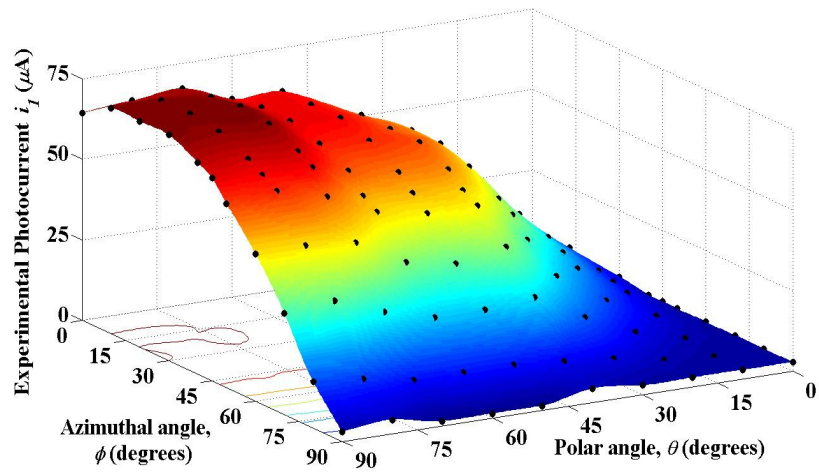


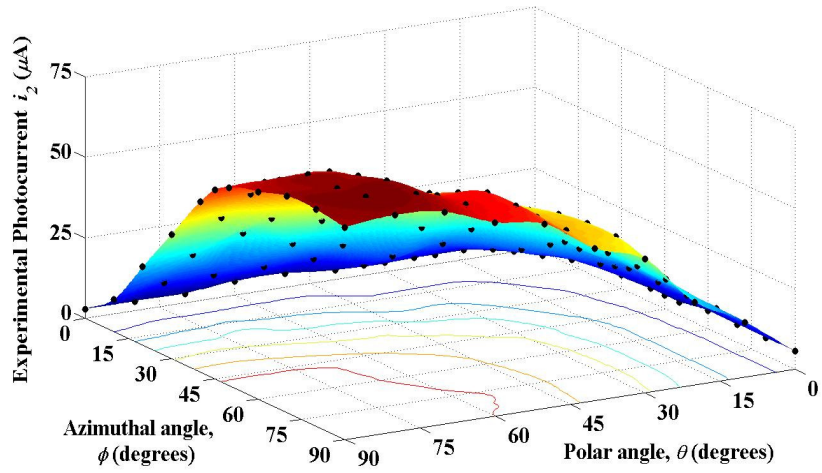
Figure 3.12 Experimental results of the retro-detection photocell for three laser orientations. Photocurrents $i_1(t)$, $i_2(t)$, and $i_3(t)$ and their resulting differential photocurrents, $i_{1-2}(t)$, $i_{1-3}(t)$, and $i_{2-3}(t)$, are shown as a function of time with a polar angle of $\theta \approx 54.7^\circ$ and (a) $\phi = 20^\circ$, (b) $\phi = 30^\circ$, and (c) $\phi = 45^\circ$. The insets show the retro-detection photocell at the respective orientations as viewed from the laser source.

To analyze the complete differential detection and optimization process over a wide range of angles, a smaller scale broadband LED optical broadcasting configuration is built and tested with the retro-detection system. The PD₁, PD₂, and PD₃ photocurrents are recorded by a digital data acquisition system as the azimuthal and polar angles are scanned in 10° increments over the ranges $0^\circ \leq \phi \leq 90^\circ$ and $0^\circ \leq \theta \leq 90^\circ$, respectively. The results are shown in Figs. 3.13(a)-(c). The resemblance of these experimental results for PD₁, PD₂, and PD₃ to their theoretical counterparts in Figs. 3.8(a)-(c) is immediately apparent. The PD₁ photocurrent in Fig. 3.13(a) rises from negligible levels at large azimuthal angles ($\phi \approx 90^\circ$) and small polar angles ($\theta \approx 0^\circ$) to a maximum of 70 μA when ϕ is small and θ is large. The PD₂ photocurrent in Fig. 3.13(b) rises from negligible levels at small azimuthal angles ($\phi \approx 0^\circ$) and small polar angles ($\theta \approx 0^\circ$) to a maximum of 68.6 μA when ϕ and θ are both large. The PD₃ photocurrent in Fig. 3.13(c) is largely independent of the azimuthal angle and rises from negligible levels at large polar angles ($\theta \approx 90^\circ$) to a maximum of 72.9 μA when θ is small. These rotational features are all apparent qualitatively by visualizing the PD illumination for angular extremes in the Fig. 3.1 coordinate system.

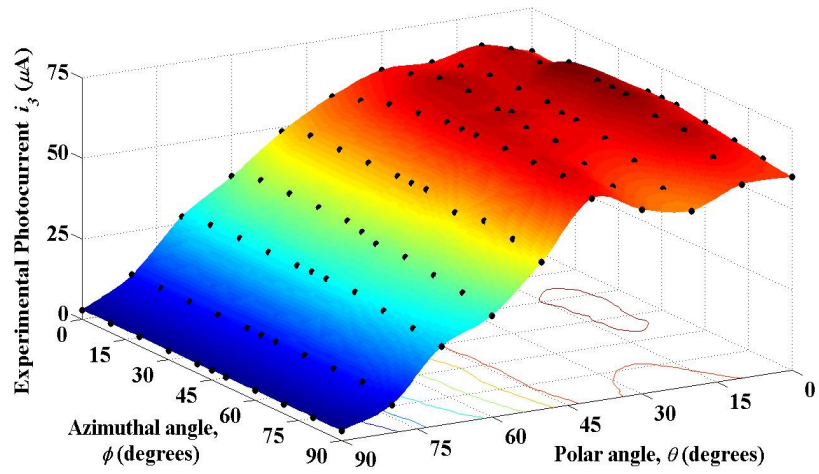
Having collected the independent photocurrents for PD₁, PD₂, and PD₃, values for the photocurrent differential sum can be recorded and the distribution can be used to optimize the optical alignment. The experimental photocurrent differential sum results are shown in Fig. 3.14 as the azimuthal and polar angles are scanned in 10° increments over the ranges $0^\circ \leq \phi \leq 90^\circ$ and $0^\circ \leq \theta \leq 90^\circ$, respectively. The resemblance of this surface to the theoretical curve defined by (126) and displayed in Fig. 3.9(a) is clear, and the resulting concavity of the distribution can be employed subsequently to optimize the retro-detector alignment. Carrying out this photocurrent differential sum minimization/optimization orients the silicon PD retro-detector at azimuthal and polar angles of $\phi \approx 45^\circ$ and $\theta \approx 55^\circ$, respectively, with the incident light entering the structure along the $\hat{r} = -\hat{x} - \hat{y} - \hat{z}$ direction.



(a)



(b)



©

Figure 3.13 Experimental photocurrent surfaces varying with ϕ and θ are shown. Results for (a) P_1 , (b) P_2 , and (c) P_3 , corresponding to PD_1 , PD_2 , and PD_3 respectively, are present.

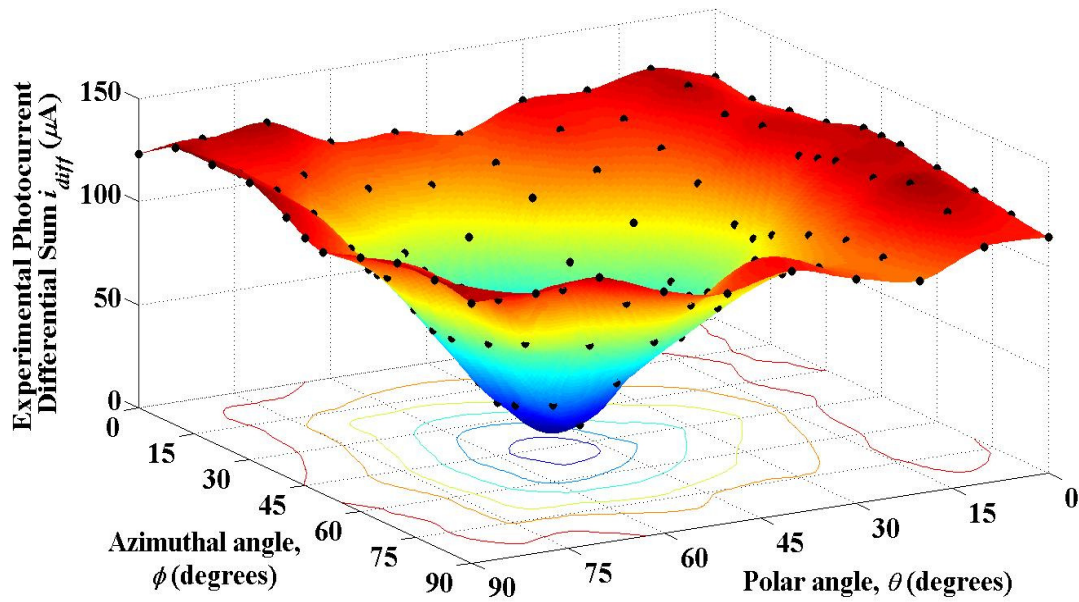
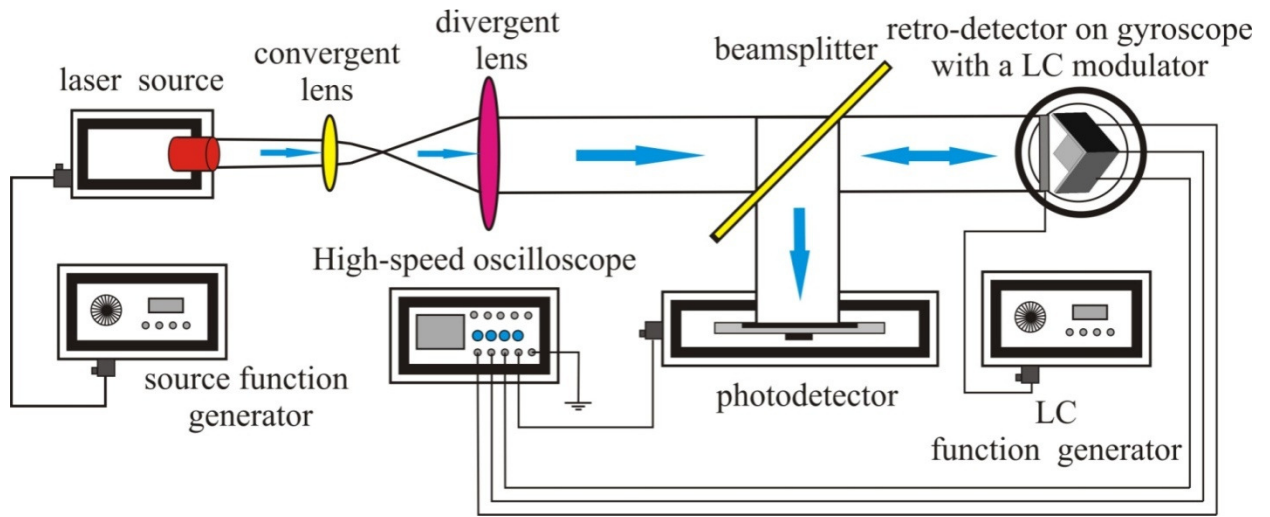


Figure 3.14 Experimental photocurrent differential sum surface varying with ϕ and θ .

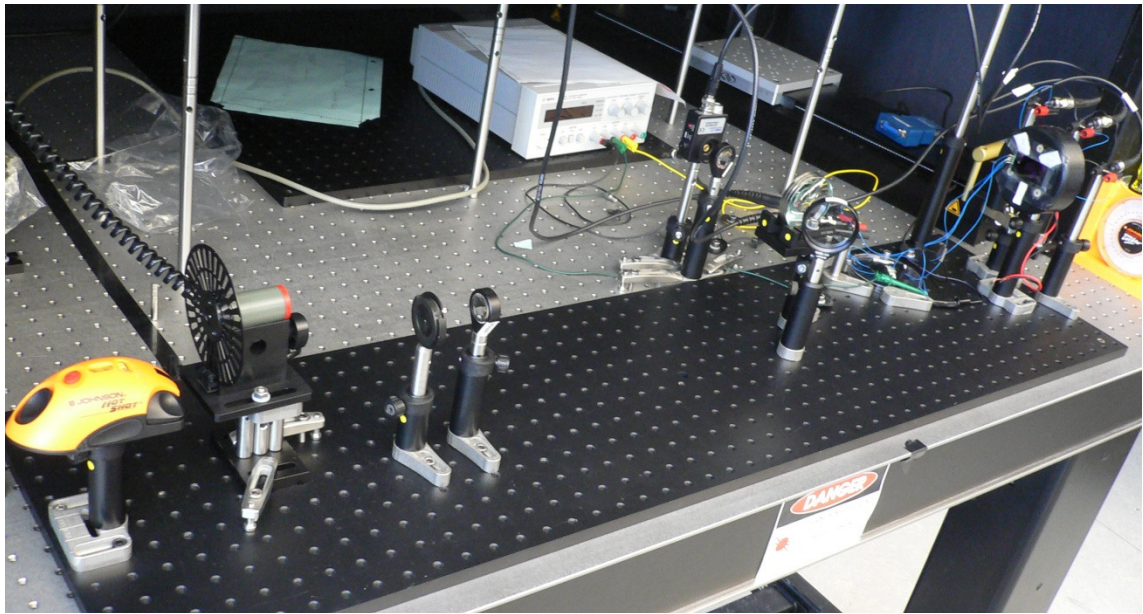
3.4.2. Verification of the Communication Capability

The proposed integrated retro-detection system has experimentally demonstrated our desired ability for active real-time optimization of optical beam alignments in the previous subsection. This active control is also a useful extension for FSO communication systems in general. The FSO communication capability is therefore verified here for this control structure, and the balanced condition achieved by minimizing the photocurrent differential sum leaves the structure in an orientation that is optimized for FSO bi-directional communication with a monochromatic laser configuration or broadband LED optical broadcasting configuration.

The laser-based FSO communication setup shown in Fig. 3.15 is built and employed for testing of the device. The laser diode is directed at the retro-detection photocell, and the ϕ and θ angles are optimized. The photocell $(x,y,z) = (1,1,1)$ orientation becomes aligned toward the laser source, and the system becomes optimized for FSO bi-directional communication. Both active downlink and passive uplink schemes are then demonstrated successively. The active downlink mode is investigated first with a 2 kHz modulated laser. The Pi-cell LC modulator remains in its on-state (open), and the summed photocurrent, $i_1(t) + i_2(t) + i_3(t)$, is shown in Fig. 3.16(a) as a function of time. The modulated characteristics of the laser transmitter are seen to be effectively detected by the retro-detector, as the incident light can be sampled by each of the three balanced PDs and subsequently summed.



(a)



(b)

Figure 3.15 The (a) CorelDraw schematic and (b) photograph of experimental laser-based system for the retro-detection photocell. They are shown to verify the communication ability of the integrated photocell. The 1mW, 650nm laser is expanded to create sufficiently collimated beams. The beams are then directed onto the photocell of interest with near-uniform beam intensity, and the optical signal is recorded remotely. The back-reflected optical beam is sampled by way of a beamsplitter and a silicon detector. Moreover, a Pi-cell LC modulator is mounted at the entrance interface of the photocell.

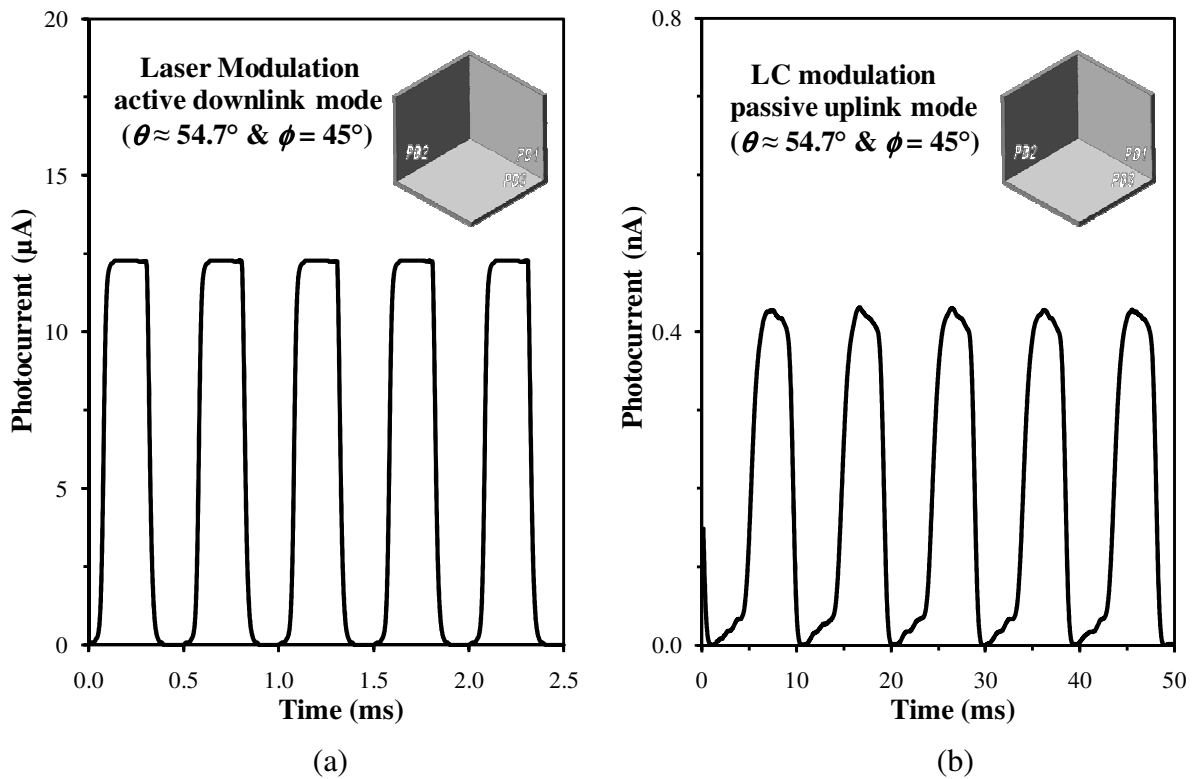


Figure 3.16 Photocurrents for the (a) active downlink mode and (b) passive uplink mode are shown as a function of time for the retro-detection photocell. It is illuminated by the modulated laser illumination and continuous laser illumination with a Pi-cell LC modulator (not shown), respectively. The photocell is in the optimal orientation with $\phi = 45^\circ$ and $\theta \approx 54.7^\circ$ (with 1 meter propagation). The figure inset shows the retro-detection structure at this optimal orientation as viewed by the source.

The alternative form of FSO communication is that of the passive uplink configuration. As it is fundamentally bi-directional in nature, a biased silicon photodetector is located at the optical source to monitor the retroreflected signal arriving back at this source. The integrated photocell is then illuminated by a continuous wave laser with the entrance Pi-cell LC modulator operating from a biased pi-state condition with a modulation frequency of 100 Hz. The resulting retroreflected signal level recorded by the photodetector is shown in Fig. 3.16(b) as a function of time. Note that the Pi-cell LC modulator effectively maps the remotely encoded information onto the retroreflected beam. The signal level and modulation depth are seen to be appreciable, as the system demonstrates a signal-to-noise ratio (SNR) beyond 40 dB. This enhanced signal is due, in large part, to the previous beam alignment optimization procedure.

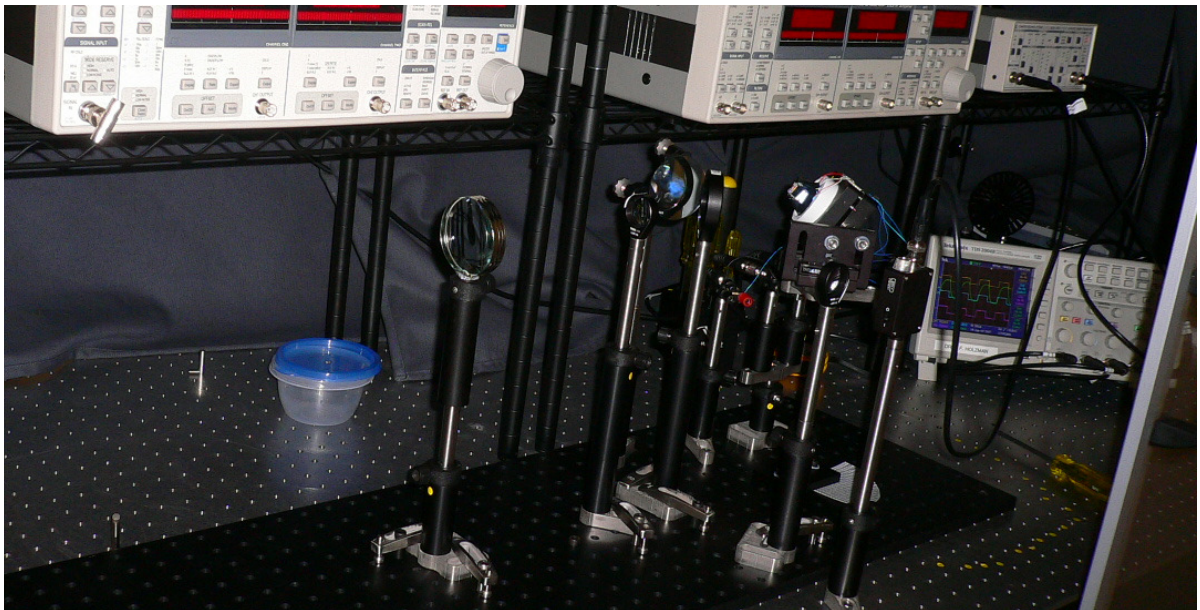


Figure 3.17 A photograph of the experimental LED-based broadcasting system is shown.

The retro-detection system of interest to this investigation is also tested with a broadband LED optical broadcasting scheme. A similar experimental setup (shown in Fig. 3.17) to that of Fig. 3.15(a) is built and used for testing. In the new system, a broadband LED source is employed with a 4 m propagation length. The broadband LED local source is modulated at 4 kHz and broadcasted in the direction of the retro-detector whose ϕ and θ angles are optimized at the orientations of $\phi \approx 45^\circ$ and $\theta \approx 55^\circ$. After 4 m propagation, the light is retroreflected by the remote retro-detector and returned directly back to the local source, where it is sampled by a photodetector. The photocurrent signal recorded at the local source is shown in Fig. 3.18(a) for the balanced orientation of $\phi \approx 45$ and $\theta \approx 55^\circ$. The 4 kHz retro-reflected signal is immediately apparent in the figure. For a broadcasted optical power of 0.25 mW, a 10.6 nA local signal is detected with a signal-to-noise ratio of approximately 40 dB. The same modulation can be seen at the remote retro-detector in Fig. 3.18(b), where the PD₁, PD₂, and PD₃ photocurrent signals are displayed as a function of time. The remote signal levels here are seen to be well-balanced (as expected), leading to a corresponding local signal that is maximized and relatively insensitive to extraneous reflections in the environment.

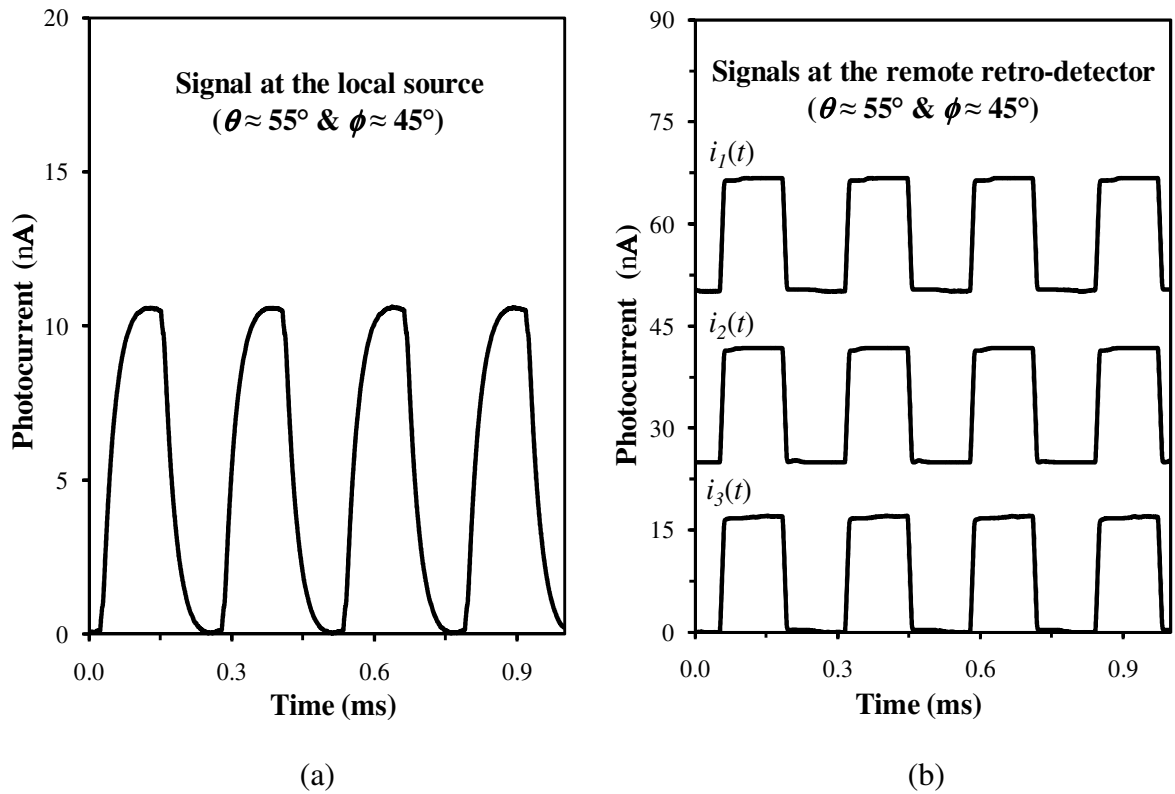


Figure 3.18 Photocurrent results for local and remote detection with 4 m propagation are shown for a modulated LED local source broadcasting toward the remote retro-detector. It has been aligned at the optimal $\phi \approx 45^\circ$ and $\theta \approx 55^\circ$ orientation. The signal retro-reflected back to the local source is shown in (a). The signal detected at the remote retro-detector is shown in (b). The PD₁, PD₂, and PD₃ photocurrent signals in (b) are plotted as $i_1(t)$ (shift up 50nA), $i_2(t)$ (shift up 25nA), and $i_3(t)$, respectively.

3.5. Summary

In summary, a corner-cube-based integrated photocell was introduced as a novel instrument for FSO communication applications. It provided the fundamental requirements for optical retroreflection, detection, and modulation. This retro-detector structure allowed for optical retro-reflection as a remote target and local signal detection by way of its constituent PDs, and it was shown that differential combinations of the local photocurrent signals could be used as a control mechanism to optimize the optical alignment. Excellent agreement was found between the theory (both analytical and Matlab ray-tracing) and experimental angular characterizations. The subsequent control and communication capabilities of the retro-detector were tested and found to be successful.

Chapter 4

Conclusions

In this chapter, some concluding remarks are given for my FSO projects device work, and some insight is given into future work for further developing these systems.

4.1. Summary of Contributions

My initial introduction to FSO systems listed existing drawbacks in FSO communication links. With this in mind, two novel optical devices were introduced and investigated within this thesis. The contributions of this work can be summarized as follows:

1. In the first phase of my thesis project, I developed an omni-directional composite solid retroreflector. This passive structure was found to be relevantly interesting for reflection-based applications (in particular, FSO communications where there exists a fundamental requirement for multi-directional optical transmission and reflection). Such devices can form the building-block of emerging multiple-input-multiple-output (MIMO) optical communication schemes, where current single-retroreflector implementations cannot provide omni-directional optical responses between many LOS communication nodes.
2. In the second phase of my project, a novel corner-cube-based integrated photocell was introduced, together with a new retro-detection technique. It was shown that differential photocurrent levels could be used to probe the alignment states of incident beams. These differential photocurrents could then be used in an actively-controlled optimization/triangulation procedure. Experimental results for this optimization were presented along with analytical and ray-tracing models. The aligned system was demonstrated with both active downlink and passive uplink communication modes. The FSO communication was found to be undoubtedly improved with perfect optical alignment.

4.2. Future Work

While the work presented in this thesis was successful at improving omni-directionality in FSO links, there still exist FSO issues which need to be addressed. Two such issues correspond to the dimensions/scales and the switching speed of the device. The prototypes presented in this thesis are cm and mm in scale, and operation was demonstrated over a low 0.1-1.0 KHz frequency range. In reality, our future work will look to extend these concepts to a much smaller spatial scale (microns) and a much faster (ultrafast) timescale.

Semiconductor crystals will be an excellent mechanism for reaching smaller spatial scales and providing much faster modulation [39, 40]. Semiconductors can be fabricated with precise, and microscopic, spatial resolutions. Moreover, a semiconductor optical switch together with a control optical pulse can be used to modulate the carrier density, refractive index and material reflectivity [41] of a co-propagating signal pulse. The turn-on time of this process can be extremely fast, being limited mainly by the duration of the incident optical pulse, while the turn-off time is set mainly by the semiconductor free-carrier lifetime. It is expected that picosecond switching schemes [42] can be successfully implemented with such a system.

With the above goals in mind, there will be two phases for the extension of my research into the future semiconductor work:

1. A singular corner-cube GaAs ultrafast optical switching device. In this initial phase, a singular mm-sized double-side-polished and gold-coated GaAs CCR will be fabricated as a photoconductive switch. There is a narrow photoconductive gap left on each individual surface of the three GaAs CCR reflectors (shown in Fig. 4.1). These gaps will be activated by an incident laser pulse to initiate ultrafast optical switching. The optical and electrical response of this novel device will be mathematically modeled and investigated theoretically and experimentally. I will analyze the effective retroreflective area and detected power in this GaAs CCR as a function of the incident angles and optimize the structure for high-speed electrical operation/detection. To our knowledge, this is the first introduction of such a CCR-based optoelectronic switching device.

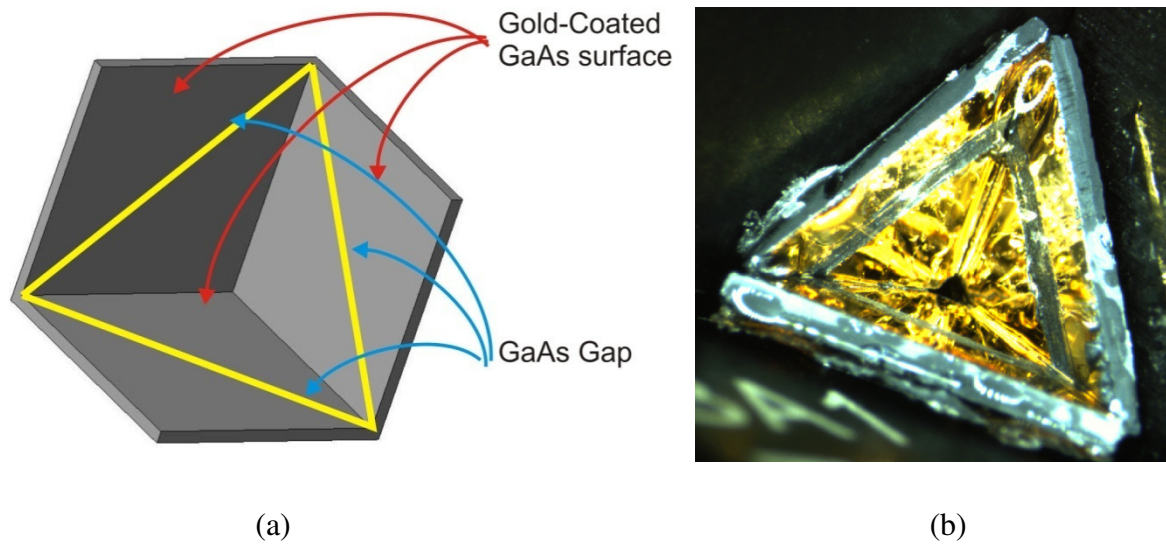


Figure 4.1 A (a) SolidWorks schematic and (b) photograph showing the proposed gold-coated GaAs corner-cube-based photoconductive switching device.

2. Integrated semiconductor retro-structures (micron scale). By selecting the correct semiconductor crystallographic orientations and etchants, corner-cube micro-structural arrays will be etched directly onto semiconductor surfaces (without the need for planar fabrication techniques) [43-46]. I will investigate the recipes/processes to effectively fabricate these semiconductor retro-surfaces and find the semiconductor lattices and etchants needed for producing $\{111\}$ corner-cube texturing (shown in Fig. 4.2). The resulting structures will have the ability for incredibly fast (subpicosecond) switching times and even the capabilities for optical-optical modulation.

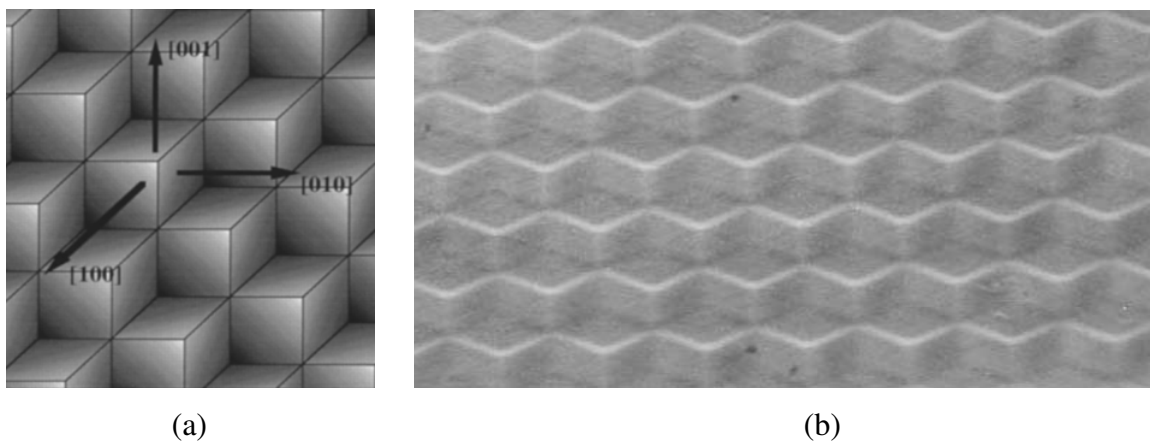


Figure 4.2 The (a) crystallographic orientations for the $\{111\}$ corner-cube texturing and the resulting (b) corner-cube micro-structural arrays.

Bibliography

- [1] V. Hsu, "MEMS Corner Cube Retroreflectors for Free-Space Optical Communications," M. Sc. Thesis, University of California, Berkeley, CA, US, 1999.
- [2] L. Zhou, J. M. Kahn, and K. S. J. Pister, "Corner-cube retroreflectors based on structure-assisted assembly for free-space optical communication," *J. Microelectromech. Syst.*, vol. 12, no. 3, pp. 233-242, Jun. 2003.
- [3] S. Junique, D. Agren, Q. Wang, S. Almqvist, B. Noharet, and J. Y. Andersson, "A modulating retroreflector for free-space optical communication," *IEEE Photon. Technol. Lett.*, vol. 18, no. 1, pp. 85-87, Jan. 2006.
- [4] P. B. Chu, N. R. Lo, E. C. Berg, and K. S. J. Pister, "Optical communication using micro corner cube reflectors," in *Proc. of IEEE MEMS Workshop*, pp. 350-355, Jan. 1997.
- [5] S. Hranilovic, *Wireless Optical Communication Systems*. New York: Springer, 2004.
- [6] R. Otte, L. P. de Jong, and A. H. M. van Roermund, *Low Power Wireless Infrared Communications*. Netherlands: Kluwer Academic, 1999.
- [7] W. Mao and J. M. Kahn, "Free-space heterochronous imaging reception of multiple optical signals," *IEEE Trans. Commun.*, vol. 52, no. 2, pp. 269-279, Feb. 2004.
- [8] X. Zhu, V. S. Hsu and J. M. Kahn, "Optical modeling of MEMS corner cube retroreflectors with Misalignment and Nonflatness," *IEEE J. Sel. Topics. Quantum Electron.*, vol. 8, no. 1, pp. 26-32, Jan. 2002.
- [9] D. C. O'Brien, G. E. Faulkner, and D. J. Edwards, "Optical properties of a retroreflecting sheet," *Appl. Opt.*, vol. 38, no. 19, pp. 4137-4144, July 1999.

- [10] W. S. Rabinovich, R. Mahon, H. R. Burris, G. C. Gilbreath, P. G. Goetz, C. I. Moore, M. F. Stell, M. J. Vilcheck, J. L. Witkowsky, L. Swingen, M. R. Suite, E. Oh, and J. Koplów, "Free-space optical communications link at 1550 nm using multiple-quantum-well modulating retroreflectors in a marine environment," *Opt. Eng.*, vol. 44, no. 5, pp. 056001-003, 2005.
- [11] D. C. O' Brien, W. W. Yuan, J. J. Liu, G. E. Faulkner, S. J. Elston, S. Collins, and L. A. Parry-Jones, "Optical wireless communications for micro-machines," in *Proc. of SPIE*, vol. 6304, pp. 63041A1-8, Aug. 2006.
- [12] W. S. Rabinovich, R. Mahon, P. G. Goetz, E. Waluschka, D. S. Katzer, S. C. Binari, and G. C. Gilbreath, "SA cat's eye multiple quantum-well modulating retro-reflector," *IEEE Photon. Technol. Lett.*, vol. 15, pp. 461-463, Apr. 2003.
- [13] B. Warneke, M. Last, B. Liebowitz, and K. S. J. Pister, "Smart dust: Communicating with a cubic-millimeter computer," *Computer*, vol. 34, no. 1, pp. 44-51, Jan. 2001.
- [14] L. Zhou, K. S. J. Pister, and J. M. Kahn, "Assembled corner-cube retroreflector quadruplet," in *Proc. of IEEE MEMS*, pp. 556-559, Jan. 2002.
- [15] X. Zhu and J. M. Kahn, "Free-space optical communication through atmospheric turbulence channels," *IEEE Trans. Commun.*, vol. 50, no. 8, pp. 1293-1300, Aug. 2002.
- [16] P. B. Chu, N. R. Lo, E. C. Barg, and K. S. J. Pister, "Optical communication using micro corner cube reflectors," in *Proceedings of IEEE Micro Electro Mechanical Systems Workshop*, pp. 350-355, 1997.
- [17] F. Farahi and D. A. Jackson, "A fibre optic interferometric system for surface profiling," *Review of Scientific Instruments*, vol. 61, no. 2, pp. 673-680, Feb. 1990.
- [18] S. H. Yueh, R. Kwok, F. K. Li, S. V. Nghiem, W. J. Wilson, and J. A. Kong, "Polarimetric passive remote sensing of wind-generated sea surfaces and ocean wind vectors," in *Proc. Oceans'93 'Engineering in Harmony with Ocean'*, vol. 1, pp. 131-136, 1993.
- [19] P. Sharma, I. S. Hudgara, and M. L. Singh, "Passive remote sensing of a buried object using a 29.9 GHz radiometer," in *Proc. Asia-Pacific Microwave*, vol. 1, pp. 2-3, 2005.

- [20] Y. H. Lee and J. K. Lee, "Passive remote sensing of three-layered anisotropic random media," in *Proc. IEEE IGARSS.*, vol. 1, pp. 249-251, 1993.
- [21] C. S. Lin, "Modulations of laser signals by water waves observed by a boxcar integrator," *IEEE Trans. Geosci. Remote Sens.*, vol. 38, pp. 198-224, Jan. 2000.
- [22] J. K. Lee and J. A. Kong, "Active microwave remote sensing of an anisotropic random medium layer," *IEEE Trans. Geosci. Remote Sens.*, vol. GE-23, pp. 910-923, Nov. 1985.
- [23] G. R. Allan, H. Riris, J. B. Abshire, X. L. Sun, E. Wilson, J. F. Burris, and M. A. Krainak, "Laser sounder for active remote sensing measurements of CO₂ concentrations," in *Proc. IEEE Aerospace*, pp. 1-7, 2008.
- [24] M. A. Zuniga, T. M. Habashy, and J. A. Kong, "Active remote sensing of layered random media," *IEEE Trans. Geosci. Remote Sens.*, vol. 17, no. 4, pp. 296-302, Oct. 1979.
- [25] R. D. Thom, T. L. Koch, J. D. Langan, and W. J. Parrish, "A fully monolithic InSb infrared CCD array," *IEEE Trans. Electron Devices*, vol. 27, no. 1, pp. 160-170, Jan. 1980.
- [26] C. R. Sharma, C. Furse, and R. R. Harrison, "Low-power STDR CMOS sensor for locating faults in aging aircraft wiring," *IEEE Sensors J.*, vol. 7, no. 1, pp. 43-50, Jan. 2007.
- [27] X. Y. Kong, "GPS modeling in frequency domain," in *Proc. IEEE 2nd Int. Conf.*, pp. 61-61, 2007.
- [28] Y. Zhou, J. Schembri, L. Lamont, and J. Bird, "Analysis of stand-alone GPS for relative location discovery in wireless sensor networks," in *Proc. IEEE CCECE*, pp. 437-441, 2009.
- [29] M. Steinhauer, H. O. Ruo, H. Irion, and W. Menzel, "Millimeter-wave-radar sensor based on a transceiver array for automotive applications," *IEEE Trans. Microw. Theory Tech.*, vol. 56, no. 2, pp. 261-269, Feb. 2008.
- [30] H. Dominik, "Short range radar – status of UWB sensors and their applications," in *Proc. IEEE European Microwave Conf.*, pp. 1530–1533, 2007.
- [31] T. Dorney, J. Johnson, D. Mittleman, and R. Baraniuk, "Imaging with THz pulses," in *Proc. IEEE Int. Conf. Image Processing*, vol. 1, pp. 764–767, 2002.

- [32] R. W. McGowan, R. A. Cheville, and D. Grischkowsky, "Direct observation of the Gouy phase shift in THz impulse ranging," *Appl. Phys. Lett.*, vol. 76, no. 6, pp. 670-672, Feb. 2000.
- [33] D. A. Humphreys and A. J. Moseley, "GaInAs photodiodes as transfer standards for picoseconds measurements," *IEE Proc. J. Optoelectronics*, vol. 135, no. 2, pp. 146-152, Apr. 1988.
- [34] D. H. Auston, "Picosecond optoelectronic switching and gating in silicon," *Appl. Phys. Lett.*, vol. 26, pp. 101-103, Feb. 1975.
- [35] R. T. Howard, A. F. Heaton, R. M. Pinson, and C. K. Carrington, "Orbital express advanced video guidance sensor," in *Proc. IEEE Aerospace Conf.*, pp. 1-10, 2008
- [36] A. Makynen and J. Kostamovaara, "Optimization of the displacement sensing precision of a reflected beam sensor in outdoor environment," in *Proc. 21th IEEE IMT Conf.*, vol. 2, pp. 1001-1004, 2004.
- [37] C. M. Collier, X. Jin, J. F. Holzman, and J. Cheng, "Omni-directional characteristics of composite retroreflectors," *J. Opt. A., Pure Appl. Opt.* vol. 11, pp. 085404(1-10), May 2009.
- [38] Y. Sun, H. Ma, Z. Zhang, and G. Fu, "Rapid response mechanism of pi cell," *Appl. Phys. Lett.*, vol. 92, no. 11, pp. 111117.1-3, Mar. 2008.
- [39] J. F. Holzman, P. Strasser, R. Wuest, F. Robin, D. Erni and H. Jackel, "Ultrafast carrier dynamics in InP photonic crystals," *Nanotechnology*, vol. 6, pp. 949-952, 2005.
- [40] Y. Rosenwals, B. R. Thacker, R. K. Ahrenkiel, and A. J. Nozik, "Photogenerated carrier dynamics under the influence of electric fields in III-V semiconductors," *Physical Review B.*, vol. 50, no. 3, pp. 1746-1754, July 1994.
- [41] J. F. Holzman, F. E. Vermeulen, and A. Y. Elezzabi, "Ultrafast photoconductive self-switch of subpicosecond electrical pulses," *IEEE J. Quantum Electron.*, vol. 36, no. 2, pp. 130-136, Feb. 2000.
- [42] A.Y. Elezzabi, J. Meyer, M. K. Y. Hughes, and S. R. Johnson, "Generation of 1-ps infrared pulsed at 10.6um by use of low temperature grown GaAs as an optical semiconductor switch," *Opt. lett.*, vol. 19, no. 12, Jun. 1994.

- [43] J. D. Hylton, A. R. Burgers, and W. C. Sinke, "Alkaline etching for reflectance reduction in multicrystalline silicon solar cells," *Journal of The Electrochemical Society*, vol. 151, no. 6, pp. G408-427, 2004.
- [44] A. Hartmann, L. Loubies, F. Reinhardt, and E. Kapon, "Self-limiting growth of quantum dot heterostructures on nonplanar {111}B substrates," *Appl. Phys.Lett.*, vol. 71, no. 10, pp. 1314-1316, Sep. 1997.
- [45] K. C. Rajkumar, K. Kaviani, J. Chen, P. Chen and A. Madhukar, "Nanofeatures on GaAs (111)B via photolithography," *Appl. Phys. Lett.*, vol. 60, no. 7, pp. 850-852, Feb. 1992.
- [46] G. W. Neudeck, J. Spitz, J. C. H. Chang, J. P. Denton, and N. Gallagher, "Precision crystal corner cube arrays for optical gratings formed by(100) silicon planes with selective epitaxial growth," *Appl. Opt.*, vol. 35, no. 19, pp. 3466- 3470, July 1996.

Appendices

Appendix A

Driving a Pi-cell Optical Modulator

The modulation scheme employed in the FSO communication links in this thesis is a new LC optical modulator, called the Pi-cell LC modulator (or Optically Compensated Bend (OCB) cell). This LC Pi-cell was first developed at Tektronix Corp. by Dr. Phil Bos in 1984, and it is marketed by LC Technologies. Its name comes from the fact that a Pi-cell has a 180° twist instead of a 90° twist like a normal TN cell. It is also characterized by a faster response time, wider viewing angle, and larger contrast ratio.

The electronics necessary to drive a Pi-cell is very different from the electronics needed to drive a normal TN cell. A normal TN cell is driven with a relative simple square wave with a typical frequency of about 50 Hz. This square wave can be directly applied on both the common plane and segment plane of the TN cell. The theory behind this operation is the fact that the TN cell displays both “on” and “off” states by way of comparing the phase states of applied square waves going to either the common or segment plane. If these two square waves are in phase, the root mean square (RMS) voltage across the entire LC cell is zero, so that the shutter turns clear (for an “off” state). In contrast, if these two square waves are 180° out of phase, the shutter turns opaque (for an “on” state). The significance here is that the 50% duty cycle of that square wave guarantees that LC cell does not witness a net DC voltage on either plane which would eventually destroy it.

The Pi-cell LC shutter has three states: (1) the rest state where zero volts are supplied and it has a slight purplish hue (45% transparent), (2) the “pi” state where the “holding voltage (3.3V)” is supplied and it is clear, and (3) the saturation state where 18-25V voltage is externally provided and it is opaque. With this in mind, to operate a Pi-cell we have to prevent the cell from

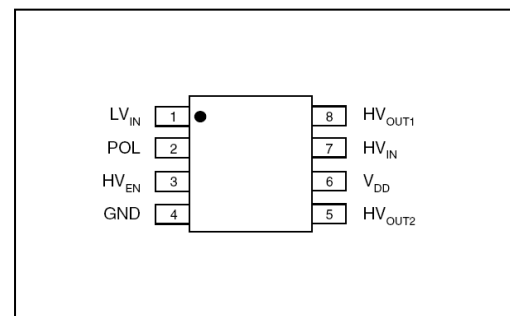
staying at and returning to the rest state and offer a square wave in phase or out of phase to the two planes of the Pi-cell. A frequency of 500-1000 Hz is normally used with some experimentation needed to optimize for each given cell.

The Pi-cell LC modulator is operated with a driver chip (shown in Fig. 5.1), HV508, that was specially designed to drive a Pi-cell by Supertex. This chip can provide 3.3V (as a holding voltage for “pi-state”) and 18V or 24V (saturation voltage) simultaneously, and it is also able to control the switching speed of the Pi-cell LC by an external frequency input. The HV508 is soldered onto a bare circuit board, and each foot of the chip is subsequently connected to individual device planes or external instrumentation. The details of the connections are given below:

1. foot “1” : Low output supplied voltage, typically 3.3V for “pi-state”.
2. foot “2” : Logical input frequency to set the output frequency, typically 100 Hz.
3. foot “3” : Logical enable pin determining the operation states.
4. foot “4” : Ground pin.
5. foot “5” : Output to segment plane or common plane.
6. foot “6” : Logical supply voltage, typically 7.5V.
7. foot “7” : High output supplied voltage, typically 18V for “saturation-state”.
8. foot “8” : Output to common plane or segment plane.



(a)



(b)

Figure 5.1 The (a) driver chip HV 508 for the Pi-cell LC modulator is soldered onto a bare circuit board, and the (b) pin configuration of the HV 508 is shown.

Appendix B

Summary of Mathematical Expressions for Individual PDs Photocurrents

In Chapter 3, we investigated the theoretical normalized photocurrents for PD₁, PD₂ and PD₃, given various directional cosine component inequality permutations. Here, the complete expressions for the individual PDs are derived based on equations (120)–(125) with various directional cosine components, n_1, n_2, n_3 . The mathematical photocurrent expression for PD₁ is

$$\begin{aligned} P_{1_total} = & n_1*(1+R)*((n_1 \leq n_2) \& (n_2 < n_3)) \\ & + n_1*(1+R)*((n_2 < n_1) \& (n_1 \leq n_3)) \\ & + n_1*(1+R)*((n_1 < n_3) \& (n_3 \leq n_2)) \\ & + n_1*(1+R)*((n_3 \leq n_1) \& (n_1 < n_2)) \\ & + (n_1 + R*(n_2 + n_3) - R*n_2*n_3/n_1)*((n_2 \leq n_3) \& (n_3 < n_1)) \\ & + (n_1 + R*(n_2 + n_3) - R*n_2*n_3/n_1)*((n_3 < n_2) \& (n_2 \leq n_1)) \\ & + R^2*(2*n_1 - n_1*n_2/n_3 - n_1*n_3/2/n_2)*((n_3 \leq (2*n_2)) \& (n_1 \leq n_2) \& (n_2 < n_3)) \\ & + R^2*n_1*n_2/n_3*((n_3 > (2*n_2)) \& (n_1 \leq n_2) \& (n_2 < n_3)) \\ & + R^2*n_1*n_2/2/n_3*((n_1 \leq n_2) \& (n_2 < n_3)) \\ & + R^2*n_1*n_2/2/n_3*((n_1 > n_2) \& (n_1 \leq n_3)) \\ & + R^2*(2*n_2 - n_1*n_2/n_3 - n_2*n_3/2/n_1)*((n_3 < (2*n_1)) \& (n_1 > n_2) \& (n_1 \leq n_3)) \\ & + R^2*n_1*n_2/n_3*((n_3 \geq (2*n_1)) \& (n_1 > n_2) \& (n_1 < n_3)) \\ & + R^2*n_3*n_2/2/n_1*((n_3 \geq n_2) \& (n_1 > n_3)) \\ & + R^2*n_2*n_3/2/n_1*((n_1 \geq n_2) \& (n_2 > n_3)) \\ & + R^2*(2*n_1 - n_1*n_3/n_2 - n_1*n_2/2/n_3)*((n_2 < (2*n_3)) \& (n_1 < n_3) \& (n_3 \leq n_2)) \\ & + R^2*n_1*n_3/n_2*((n_2 \geq (2*n_3)) \& (n_1 < n_3) \& (n_3 < n_2)) \\ & + R^2*n_3*n_1/2/n_2*((n_3 \leq n_2) \& (n_1 < n_3)) \\ & + R^2*n_1*n_3/2/n_2*((n_1 \geq n_3) \& (n_2 > n_1)) \end{aligned}$$

$$\begin{aligned}
&+R^2*(2*n3-n1*n3/n2-n2*n3/2/n1)*((n2<=(2*n1))\&(n1<n2)\&(n1>=n3)) \\
&+R^2*n1*n3/n2*((n2>(2*n1))\&(n1<n2)\&(n1>=n3)) \\
&+R^2*n3*n2/2/n1*((n3>=n2)\&(n1>n3)) \\
&+R^2*n2*n3/2/n1*((n1>=n2)\&(n2>n3)).
\end{aligned}$$

The mathematical photocurrent expression for PD₂ is

$$\begin{aligned}
P_{2_total} = &n2*(1+R)*((n1<n2)\&(n2<=n3)) \\
&+n2*(1+R)*((n2<=n1)\&(n1<n3)) \\
&+n2*(1+R)*((n2<n3)\&(n3<=n1)) \\
&+n2*(1+R)*((n3<=n2)\&(n2<n1)) \\
&+(n2+R*(n1+n3)-R*n1*n3/n2)*((n1<=n3)\&(n3<n2)) \\
&+(n2+R*(n1+n3)-R*n1*n3/n2)*((n3<n1)\&(n1<=n2)) \\
&+R^2*(2*n1-n1*n2/n3-n1*n3/2/n2)*((n3<=(2*n2))\&(n1<=n2)\&(n2<n3)) \\
&+R^2*n1*n2/n3*((n3>(2*n2))\&(n1<=n2)\&(n2<n3)) \\
&+R^2*n1*n2/2/n3*((n1<=n2)\&(n2<n3)) \\
&+R^2*n1*n2/2/n3*((n1>n2)\&(n1<=n3)) \\
&+R^2*(2*n2-n1*n2/n3-n2*n3/2/n1)*((n3<(2*n1))\&(n1>n2)\&(n1<=n3)) \\
&+R^2*n1*n2/n3*((n3>=(2*n1))\&(n1>n2)\&(n1<n3)) \\
&+R^2*n1*n3/2/n2*((n3>n1)\&(n2>=n3)) \\
&+R^2*n1*n3/2/n2*((n1>=n3)\&(n2>n1)) \\
&+R^2*(2*n2-n2*n3/n1-n1*n2/2/n3)*((n1<=(2*n3))\&(n1>n3)\&(n2<=n3)) \\
&+R^2*n2*n3/n1*((n1>(2*n3))\&(n2<=n3)\&(n3<n1)) \\
&+R^2*n3*n1/2/n2*((n3<=n2)\&(n1<n3)) \\
&+R^2*n1*n3/2/n2*((n1>=n3)\&(n2>n1)) \\
&+R^2*(2*n3-n2*n3/n1-n1*n3/2/n2)*((n1<=(2*n2))\&(n3<n2)\&(n1>=n2)) \\
&+R^2*n2*n3/n1*((n1>=(2*n2))\&(n3<n2)\&(n2<n1)) \\
&+R^2*n3*n2/2/n1*((n3>=n2)\&(n1>n3)) \\
&+R^2*n2*n3/2/n1*((n1>=n2)\&(n2>n3)).
\end{aligned}$$

The mathematical photocurrent expression for PD₃ is

$$P_{3_total} = n3*(1+R)*((n1<n3)\&(n3<=n2))$$

$$\begin{aligned}
&+n^3*(1+R)*((n^3\leq n^1)\&(n^1<n^2)) \\
&+n^3*(1+R)*((n^2\leq n^3)\&(n^3<n^1)) \\
&+n^3*(1+R)*((n^3<n^2)\&(n^2\leq n^1)) \\
&+(n^3+R*(n^2+n^1)-R*n^2*n^1/n^3)*((n^1\leq n^2)\&(n^2<n^3)) \\
&+(n^3+R*(n^2+n^1)-R*n^2*n^1/n^3)*((n^2<n^1)\&(n^1\leq n^3)) \\
&+R^2*(2*n^1-n^1*n^3/n^2-n^1*n^2/2/n^3)*((n^2<(2*n^3))\&(n^1<n^3)\&(n^3\leq n^2)) \\
&+R^2*n^1*n^3/n^2*((n^2\geq(2*n^3))\&(n^1<n^3)\&(n^3<n^2)) \\
&+R^2*n^1*n^2/2/n^3*((n^1\leq n^2)\&(n^2<n^3)) \\
&+R^2*n^1*n^2/2/n^3*((n^1>n^2)\&(n^1\leq n^3)) \\
&+R^2*(2*n^2-n^3*n^2/n^1-n^1*n^2/2/n^3)*((n^1\leq(2*n^3))\&(n^1>n^3)\&(n^2\leq n^3)) \\
&+R^2*n^2*n^3/n^1*((n^1>(2*n^3))\&(n^1>n^3)\&(n^2\leq n^3)) \\
&+R^2*n^1*n^2/2/n^3*((n^1\leq n^2)\&(n^2<n^3)) \\
&+R^2*n^1*n^2/2/n^3*((n^1>n^2)\&(n^3\geq n^1)) \\
&+R^2*(2*n^3-n^1*n^3/n^2-n^3*n^2/2/n^1)*((n^2\leq(2*n^1))\&(n^1<n^2)\&(n^3\leq n^1)) \\
&+R^2*n^1*n^3/n^2*((n^2>(2*n^1))\&(n^2>n^1)\&(n^3\leq n^1)) \\
&+R^2*n^3*n^1/2/n^2*((n^3\leq n^2)\&(n^1<n^3)) \\
&+R^2*n^1*n^3/2/n^2*((n^1\geq n^3)\&(n^2>n^1)) \\
&+R^2*(2*n^3-n^2*n^3/n^1-n^1*n^3/2/n^2)*((n^1<(2*n^2))\&(n^3<n^2)\&(n^1\geq n^2)) \\
&+R^2*n^2*n^3/n^1*((n^1\geq(2*n^2))\&(n^3<n^2)\&(n^2<n^1)) \\
&+R^2*n^3*n^2/2/n^1*((n^3\geq n^2)\&(n^1>n^3)) \\
&+R^2*n^2*n^3/2/n^1*((n^1\geq n^2)\&(n^2>n^3)).
\end{aligned}$$

Appendix C

Matlab Ray-tracing Code

The differential triangulation used to optimize the optical alignment can be modeled with a ray-tracing approach, whereby the singular CCR structure is illuminated from a sufficiently large light source with a uniform intensity grid at various ϕ and θ directions both ranging from 0° to 90° . The complete Matlab program is attached here.

```
%%%%%%%%%%%%%%%%%%%%%%%%%%%%%%%%%%%%%%%%%%%%%%%%%%%%%%%%%%%%%%%%%%%%%%%%%%  
% Here make CCR visible structure  
a=linspace(0,1,2); % Define the Dimension of the CCR  
b=linspace(0,1,2);  
c=linspace(0,1,2);  
  
[x1,y1]=meshgrid(a,b); % x-y Plane  
z1=zeros(length(x1),length(y1));  
[x2,z2]=meshgrid(a,c); % x-z Plane  
y2=zeros(length(x2),length(z2));  
[y3,z3]=meshgrid(b,c); % y-z Plane  
x3=zeros(length(y3),length(z3));  
  
figure  
h1=surf(x1,y1,z1,'FaceColor','r');hold on % Plot x-y Plane  
h2=surf(x2,y2,z2,'FaceColor','y');hold on % Plot x-z Plane  
h3=surf(x3,y3,z3,'FaceColor','b');hold on % Plot y-z Plane  
xlabel('X-axis')  
ylabel('Y-axis')
```

```

xlabel('Z-axis')
axis([-5,5,-5,5,-5,5])
grid on

%%%%%%%%%%%%%%%%%%%%%%%%%%%%%%%%%%%%%%%%%%%%%%%%%%%%%%%%%%%%%%%%%%%%%%%%%%
Here make incident source (surface) visible structure
phi=0:0.5:90; % Define the Horizontal Angles
Phi=phi*pi/180;
theta=0:0.5:90; % Define the Polar Angles
Theta=theta*pi/180;

%%%%%%%%%%%%%%%%%%%%%%%%%%%%%%%%%%%%%%%%%%%%%%%%%%%%%%%%%%%%%%%%%%%%%%%%%%
Ray tracing part (Main part of the program)
Power_Difference=zeros(length(Phi),length(Theta));

y4=linspace(-3,3,90);
z4=linspace(-3,3,90);
y5=meshgrid(y4,z4);
z5=meshgrid(z4,y4);
z5=z5';
x5=zeros(length(y4),length(z4))+3; % Create Initial Incident Plane

x6=zeros(length(x5),length(y5));
y6=zeros(length(x5),length(y5));
z6=zeros(length(x5),length(y5)); % Create Rotation Plane
for m1=1:length(Phi)
    for n1=1:length(Theta)
        m1/size(Phi,2)*100 % Running Percentage

x6=cos(Phi(m1))*cos(Theta(n1)).*x5-sin(Phi(m1))*cos(Theta(n1)).*y5-sin(Theta(n1)).*z5;
y6=sin(Phi(m1)).*x5+cos(Phi(m1)).*y5;

```

```

z6=cos(Phi(m1))*sin(Theta(n1)).*x5-sin(Phi(m1))*sin(Theta(n1)).*y5+cos(Theta(n1)).*z5;
                                                                    % Rotation Matrix

x=cos(Phi(m1))*cos(Theta(n1));
                                                                    % Spherical to Cartesian
y=sin(Phi(m1));
z=cos(Phi(m1))*sin(Theta(n1));

R_total=0.36;
                                                                    % Angular Independent Reflectivity

DET1=zeros(length(x6),length(y6));
                                                                    % Final Detected Power in Mirror1
DET2=zeros(length(x6),length(y6));
                                                                    % Final Detected Power in Mirror2
DET3=zeros(length(x6),length(y6));
                                                                    % Final Detected Power in Mirror3

    for m11=1:length(x5)
                                                                    % Create Ray tracing --time, position and velocity
        for n11=1:length(y5)
            bit=12;
            pos0=[x6(m11,n11),y6(m11,n11),z6(m11,n11)];
                                                                    % Initial Ray Position
            vel0=[-x/bit -y/bit -z/bit];
                                                                    % Initial Velocity
            P=1;
                                                                    % Initial Normalized Power

            dt=0.5; time=0:dt:500;
                                                                    % Propagating ray: time, position and velocity
            pos=zeros(size(time,2),size(pos0,2)); pos(1,:)=pos0;
            vel=zeros(size(time,2),size(pos0,2)); vel(1,:)=vel0;

            Mirror1=0;Mirror2=0;Mirror3=0;
                                                                    % Mirror Flag Index

            for i=1:size(time,2)
                vel(i+1,:)=vel(i,:);
                pos(i+1,:)=pos(i,:)+vel(i,:)*dt;

                if((abs(pos(i+1,1))<=(x/bit))&&(Mirror1==0)&&(pos(i+1,2)<=1)&&(pos(i+1,3)<=1)&&(pos(i+
                1,2)>=0)&&(pos(i+1,3)>=0)),

```

```

vel(i+1,1) = - vel(i+1,1);
DET1(m11,n11)=DET1(m11,n11)+P*(1-R_total);
P=P*R_total;
Mirror1=Mirror1+1;
end

if((abs(pos(i+1,2))<=(y/bit))&&(Mirror2==0)&&(pos(i+1,1)<=1)&&(pos(i+1,3)<=1)&&(pos(i+
1,1)>=0)&&(pos(i+1,3)>=0)),
vel(i+1,2) = - vel(i+1,2);
DET2(m11,n11)=DET2(m11,n11)+P*(1-R_total);
P=P*R_total;
Mirror2=Mirror2+1;
end

if((abs(pos(i+1,3))<=(z/bit))&&(Mirror3==0)&&(pos(i+1,1)<=1)&&(pos(i+1,2)<=1)&&(pos(i+
1,1)>=0)&&(pos(i+1,2)>=0)),
vel(i+1,3) = - vel(i+1,3);
DET3(m11,n11)=DET3(m11,n11)+P*(1-R_total);
P=P*R_total;
Mirror3=Mirror3+1;
end
end

plot3(pos(:,1),pos(:,2),pos(:,3),'k'); hold on % Plot Ray Trace

end
end

detect1=0;detect2=0;detect3=0; % Total Detected Power in each Mirrors.
for parameter1=1:length(x6)
    for parameter2=1:length(y6)
        detect1=detect1+DET1(parameter1,parameter2);
    end
end

```

```

        detect2=detect2+DET2(parameter1,parameter2);
        detect3=detect3+DET3(parameter1,parameter2);
    end
end

Power_Difference(m1,n1) = abs(detect1-detect2)+ abs(detect2-detect3)+ abs(detect1-detect3);
    end
end

surfc(phi, theta, Power_Difference);           % Plot the Final differential Plot

%%%%%%%%%%%%%%%%%%%%%%%%%%%%%%%%%%%%%%%%%%%%%%%%%%%%%%%%%%%%%%%%%%%%%%%%%%
% Define the Properties of Plot

xlabel('Polar angle, {\it\theta}(degrees)', 'fontsize', 20 , 'fontweight', 'b', 'fontname', 'Times New
Roman');

ylabel('Azimuthal angle, {\it\phi} (degrees)', 'fontsize', 20, 'fontweight', 'b', 'fontname', 'Times
New Roman');

zlabel('Summed Differential Photocurrents (arb. units)', 'fontsize', 20, 'fontweight', 'b', 'fontname',
'Times New Roman');

axis([0 90 0 45 0 1]);

view(150,30);

set(0, 'defaultAxesFontSize', 20, 'defaultAxesFontName', 'Times New Roman',
'defaultAxesFontWeight', 'b');

set(0, 'defaultAxesXTick', [0;15;30;45;60;75;90], 'defaultAxesYTick', [0;15;30;45],
'defaultAxesZTick', [0;0.25;0.5;0.75;1])

```